Search for Resonant Top Quark Pair Production in the Muon+Jets Channel with the CMS Detector

Zur Erlangung des akademischen Grades eines
Doktors der Naturwissenschaften
von der Fakultät für Physik des
KIT – Karlsruher Institut für Technologie

genehmigte

Dissertation

von

Dipl.-Phys. Jochen Ott
aus Bietigheim-Bissingen

Tag der mündlichen Prüfung: 14.12.2012

Referent: Prof. Dr. Thomas Müller
Korreferent: Prof. Dr. Günter Quast

Introduction

The standard model of particle physics accurately describes a multitude of observations. However, it neither includes gravitation or explains the large hierarchy between the gravitational scale and electroweak scale (hierarchy problem), nor does it provide explanations of astrophysical observations attributed to dark matter, dark energy, or the baryon asymmetry. These shortcomings inspired many theories beyond the standard model (BSM) predicting new phenomena at the TeV-scale that could be visible at the LHC [1]. The top quark is the heaviest particle in the standard model and as such, it plays a special role in many BSM theories, some predicting a resonance decaying preferentially to top quark pairs $t\bar{t}$. Such models include topcolor-assisted technicolor models that explain the large top quark mass and predict a leptophobic topcolor Z' [2,3] and Randall-Sundrum models with warped extra dimensions solving the hierarchy problem [4], which can give rise to a Kaluza-Klein partner of the gluon detectable at the LHC [5]. Other relevant theories include additional massive gauge bosons from unified gauge groups [6], and some models that explain the unusually large forward-backward asymmetry of the top quark production at the Tevatron [7–12] predict a resonance decaying to $t\bar{t}$, e.g. [13–17].

Independent of the specific model, a resonance that decays to $t\bar{t}$ is predicted, which is always referred to as Z' in this thesis. If the natural width of the Z', $\Gamma_{Z'}$, is not too large compared to the experimental resolution and if the interference effects with standard model $t\bar{t}$ production can be neglected, the Z' manifests itself as a peak in the $M_{t\bar{t}}$ distribution. Searches based on the $M_{t\bar{t}}$ distribution are rather model-independent and allow to set limits on the cross section $\sigma(pp \to Z' \to t\bar{t})$ as a function of $M_{Z'}$.

Searches for Z' are also performed at the Tevatron [18–20], at ATLAS in the lepton+jets channel [21,22], in the dilepton channel [23], and in the all-hadronic channel [24]. Other Z' searches at CMS are performed in the all-hadronic and dilepton channels [25,26].

This thesis presents a search for $Z' \to t\bar{t}$ resonances using the $t\bar{t}$ invariant mass spectrum in the muon+jets channel. The main challenges of this analysis are the selection and reconstruction of $t\bar{t}$ events from a high-mass resonance in which the top quarks have large transverse momentum, and the decay products of the top quarks are therefore not always reconstructed as well-separated isolated objects in the detector. This requires to develop new selection and reconstruction techniques, which

are different from those used in typical standard model $t\bar{t}$ analyses. The analyzed data have been recorded with the CMS detector during the 2011 proton–proton run of the LHC with a center-of-mass energy of $\sqrt{s} = 7\,\text{TeV}$ and corresponds to an integrated luminosity of $L = 5.0\,\text{fb}^{-1}$. No significant deviation from the standard model backgrounds are found, and upper limits on the cross section $\sigma(pp \to Z' \to t\bar{t})$ are set as a function of the Z' mass, for different widths $\Gamma_{Z'}$. Model-dependent mass limits are set for a leptophobic topcolor Z' model and for Kaluza-Klein excitations of the gluon.

The analysis is a continuation of simulation-only studies at a center-of-mass energy of $\sqrt{s} = 10\,\text{TeV}$ in reference [27]. The analysis methods developed on simulation have been applied using a dataset corresponding to $L = 1.1\,\text{fb}^{-1}$, which is documented in reference [28]. It is the first measurement in this channel using the newly developed analysis techniques. In this thesis, the analysis has been further improved by including more data and by enhancing the analysis technique. This improved analysis has been combined with an electron+jets analysis at CMS, which uses similar selection and reconstruction algorithms [29, 30].

Chapter 1 briefly reviews the standard model of particle physics and the phenomenology of the top quark, and chapter 2 describes the CMS detector at the LHC. The remaining chapters describe the analysis steps in the order they are performed: Chapter 3 discusses the event simulation and low-level object reconstruction, followed by a description of the event selection and $t\bar{t}$ reconstruction in chapter 4. The statistical methods to extract upper limits on the Z' cross section are introduced in chapter 5, and the resulting limits for the Z' cross section and model-specific Z' mass limits are given in chapter 6. A short summary and some concluding remarks are given in chapter 7.

Contents

1 Theory

The standard model of particle physics describes the constituents of matter (fermions) and their interactions within the framework of a quantum-field theory. Its extensive theory framework and rich phenomenology only allow a superficial introduction in this thesis, which is given in the first section. The second section focuses on the top quark production and decay in the standard model and a generic Z′ model used in this analysis. The chapter concludes with a brief section outlining the Monte-Carlo event generation techniques.

1.1 Standard Model

This section provides a brief introduction to the standard model of elementary particle physics; a more detailed introduction to the standard model and quantum field theory can be found in textbooks [31–34], or reviews [35–39].

The standard model successfully describes most of the phenomena in particle physics; the only currently known exceptions are gravitation and neutrino masses, and both can be neglected for observables at colliders. The interactions in the standard model are introduced via local gauge invariance based on the group $SU(3)_C \times SU(2)_L \times U(1)_Y$, where the $SU(3)$ group corresponds to the strong interaction, Quantum Chromodynamics, while the group $SU(2)_L \times U(1)_Y$ corresponds to the electromagnetic and weak interactions.

The fundamental fermions in the standard model are summarized in table 1.1.[1] All fermions participate in the weak interaction, electrically charged particles in the electromagnetic interactions, and only the quarks in the strong interaction. The following sections provide an introduction into the different interactions of the standard model, mainly following reference [36].

[1] The convention $\hbar = c = 1$ is used in this thesis.

Quarks				Leptons			
Charge $2/3$		Charge $-1/3$		Charge -1		Charge 0	
	Mass (GeV)		Mass (GeV)		Mass (GeV)		Mass
u	0.0018–0.0030	d	0.0045–0.0055	e	0.000511	ν_e	$< 2\,\text{eV}$
c	1.25–1.30	s	0.090–0.100	μ	0.106	ν_μ	$< 0.19\,\text{MeV}$
t	173.5±1.0	b	4.2–4.7	τ	1.777	ν_τ	$< 18.2\,\text{MeV}$

Table 1.1: The masses of the quarks and leptons in the standard model, with their electric charge in units of the electron charge $|e|$ [35]. Note that neutrinos in the standard model are massless, and the given neutrino mass limits refer to the effective neutrino masses.

1.1.1 Quantum Chromodynamics

Quantum Chromodynamics is based on the gauge group $SU(3)$ with quark fields arranged in color triplets, and the Lagrangian density is

$$\mathcal{L}_{QCD} = -\frac{1}{4}\sum_{A=1}^{8} F^A_{\mu\nu}F^{A\mu\nu} + \sum_{j=1}^{n_f} \bar{q}_j(i\not{D} - m_j)q_j \tag{1.1}$$

where q_j are the quark fields with flavor j and mass m_j; n_f is the number of flavors, $n_f = 6$ in the standard model. The derivative $\not{D} = D_\mu\gamma^\mu$, where γ^μ are the Dirac matrices and D_μ is the covariant derivative,

$$D_\mu = \partial_\mu - ie_s\sum_A t^A g^A_\mu, \tag{1.2}$$

where e_s is the gauge coupling, and in analogy to electrodynamics, the strong structure constant is given by

$$\alpha_s = \frac{e_s^2}{4\pi}. \tag{1.3}$$

t^A with $A = 1,\ldots,8$ are the $SU(3)$ generators in the 3×3 matrix representation acting on the quark fields q. g^A_μ are the vector gluon fields and

$$F^A_{\mu\nu} = \partial_\mu g^A_\nu - \partial_\nu g^A_\mu - e_s C_{ABC} g^B_\mu g^C_\nu, \tag{1.4}$$

where the structure constants C_{ABC} of the group $SU(3)$ are defined by

$$[t^A, t^B] = iC_{ABC}t^C \tag{1.5}$$

with the normalization trace $[t^A, t^B] = 1/2\delta^{AB}$.

In the perturbative expansion, the terms in the Lagrangian correspond to vertices in the Feynman graphs. The vertices in the QCD are the gluon–quark–antiquark vertex — where the quark and antiquark are of the same flavor — and the three-gluon and four-gluon vertices of order e_s and e_s^2, respectively. The latter gauge boson self-couplings appear only in non-Abelian gauge theories in which the structure constants C_{ABC} are non-zero, and the last term on the right hand side of equation (1.4) does not vanish.

Two important properties of QCD are quark confinement and asymptotic freedom. Confinement is the observation that quarks do not exist as free particles, but only hadrons, which are color-neutral combinations of quarks and gluons. When gluons and quarks in the final state of a process, such as $e^+e^- \to q\bar{q}$, separate, the coupling effectively increases with the distance r, eventually creating new $q\bar{q}$ pairs from the vacuum. In the detector, the quarks and gluons appear as collimated stream of hadrons, known as jets. In perturbative QCD, the effective coupling strength α_s for the vertices of the Feynman graphs is modified by higher-order radiative corrections. These corrections depend on the momentum transfer of the vertex and the coupling α_s gains a dependence on the momentum transfer Q^2, a fact referred to as *running coupling*. Asymptotic freedom means that the effective coupling α_s decreases for large Q^2. Conversely, for decreasing Q^2, the effective coupling becomes very large, and the perturbative approach breaks down.

1.1.2 Electroweak Interactions

The electroweak interaction is introduced via the $SU(2)_L \times U(1)_Y$ gauge group in analogy to QCD. To explain the masses of the gauge bosons of the weak interaction, the standard model includes the Higgs mechanism, which is also responsible for the fermion masses, as will be explained below. The electroweak Lagrangian density is split into the symmetrical part and the Higgs sector,

$$\mathcal{L}_{EWK} = \mathcal{L}_{symm} + \mathcal{L}_{Higgs}. \tag{1.6}$$

The symmetrical part defines the matter field and the electroweak gauge bosons (where it is understood that the sum is taken over all fermion fields ψ)

$$\mathcal{L}_{symm} = -\frac{1}{4}\sum_{A=1}^{3} F^A_{\mu\nu}F^{A\mu\nu} - \frac{1}{4}B_{\mu\nu}B^{\mu\nu} + i\bar{\psi}_L \not{D}_L \psi_L + i\bar{\psi}_R \not{D}_R \psi_R, \tag{1.7}$$

where — in analogy to equation (1.1) — the first two parts are the kinematic term of the gauge bosons of $SU(2)_L \times U(1)_Y$ with

$$B_{\mu\nu} = \partial_\mu B_\nu - \partial_\nu B_\mu \qquad \text{and} \qquad F^A_{\mu\nu} = \partial_\mu W^A_\nu - \partial_\nu W^A_\mu - g\epsilon_{ABC}W^B_\mu W^C_\nu. \tag{1.8}$$

	ν_L	e_L	e_R	u_L	d_L	u_R	d_R
t^3	$+1/2$	$-1/2$	0	$+1/2$	$-1/2$	0	0
Y	-1	-1	-2	$+1/3$	$+1/3$	$+4/3$	$-2/3$
Q	0	-1	-1	$+2/3$	$-1/3$	$+2/3$	$-1/3$

Table 1.2: The quantum numbers weak isospin t^3, hypercharge Y, and electric charge $Q = t^3 + Y/2$ for left-handed and right-handed quarks and leptons.

Here, B_μ is the gauge field of the $U(1)_Y$ and W_μ^A for $A = 1, 2, 3$ are the gauge fields of the group $SU(2)_L$. The structure constants of the $SU(2)_L$ coincide with the totally asymmetric Levi-Civita tensor ϵ_{ABC}.

The fermion fields ψ_L and ψ_R denote the left-handed and right-handed components of the field ψ and are defined by $\psi_{L,R} = 1/2(1 \mp \gamma^5)\psi$, with $\gamma^5 = i\gamma^0\gamma^1\gamma^2\gamma^3$.

The interactions of the fermions with the gauge fields appear within the covariant derivatives $\not{D}_L$ and $\not{D}_R$ in equation (1.7). The electroweak interaction is different for right-handed and left-handed fermions; the electroweak theory is *chiral*: The fields ψ_L are doublets under the $SU(2)_L$, whereas the right-handed fields ψ_R are singlets. This chirality prohibits introducing fermion mass terms into the Lagrangian directly, which would contain terms proportional to $\bar{\psi}_L\psi_R$ violating the gauge symmetry. The covariant derivatives are given by

$$D_{\mu,L/R} = \partial_\mu + ig\sum_{A=1}^{3} t_{L/R}^A W_\mu^A + ig'\frac{1}{2}Y_{L/R}B_\mu, \tag{1.9}$$

where $t_{L/R}^A$ and $1/2Y_{L/R}$ are representations of the generators of the groups $SU(2)_L$ and $U(1)_Y$, respectively. Table 1.2 summarizes the quantum numbers of the fermions in the standard model.

The linear combinations $(W^1 \pm iW^2)/\sqrt{2}$ correspond to the charged bosons $W^\mp$ and W_μ^3 mixes with B_μ to the photon field A_μ and the field of the Z boson Z_μ. This mixing is described by a single angle θ_W with

$$A_\mu = \cos\theta_W B_\mu + \sin\theta_W W_\mu^3 \tag{1.10}$$

$$Z_\mu = -\sin\theta_W B_\mu + \cos\theta_W W_\mu^3, \tag{1.11}$$

where $\tan\theta_W = g'/g$. These relations allow to derive the coupling strength of the boson–fermion–fermion vertices and the W/Z three-/four-vertex in terms of the couplings g and g', which is however not done here. It is worth pointing out,

however, that these relations lead to predictions for many electroweak observables with only few parameters, and this provides an excellent testbed for the structure of the electroweak sector of the standard model. By including radiative corrections for these observables, precision measurements allow indirect constraints on the top mass, Higgs boson mass, and new physics. For details, see e.g. [35] and references therein.

The gauge bosons and fermions as introduced so far are massless. A mechanism to give masses to the gauge bosons and fermions that preserves gauge invariance is *spontaneous symmetry breaking*, where the coupling to a field with non-zero vacuum expectation value generates the masses. The minimal implementation of the symmetry breaking is the Higgs mechanism. The Higgs mechanism introduces a Lorentz-scalar, weak doublet field ϕ with the Langrangian density

$$\mathcal{L}_{\text{Higgs}} = (D_\mu \phi)^\dagger (D^\mu \phi) - V(\phi^\dagger \phi) - \bar{\psi}_L \Gamma \psi_R \phi - \bar{\psi}_R \Gamma^\dagger \psi_L \phi^\dagger. \tag{1.12}$$

Spontaneous symmetry breaking is induced by choosing the potential $V(\psi)$ such that the energy minimum is at $\phi \neq 0$,

Rewriting the Lagrangian density around the energy minimum, the last two terms in equation (1.12) with the matrices Γ lead to mass terms for the fermions. The fields ψ_L and ψ_R in these Yukawa terms denote any fields with the same quantum numbers and thus in general contain non-diagonal terms, leading to the mass eigenstates of the quarks not coinciding with the weak states. The relation of the mass eigenstates and weak eigenstates can be expressed as a matrix multiplication with the CKM matrix.

Through the covariant derivative D_μ in the kinematic term for ψ in equation (1.12), the Higgs doublet couples to the electroweak bosons and three of the four degrees of freedom of the ψ correspond to the longitudinal components of the (now massive) $W^\pm$ and Z_0 bosons. One degree of freedom remains, the Higgs boson, which could be the boson with a mass of 125 GeV recently found at the LHC [40, 41].

1.2 Top Quark

1.2.1 Standard Model Properties

The top quark has been predicted as the electroweak partner of the bottom quark and was discovered after many years of direct search and indirect electroweak constraints in 1995 at the Tevatron [42, 43]. In the standard model, top quark pairs at a hadron collider are produced almost exclusively via the strong coupling. Some of the leading-order Feynman graphs for top quark pair production are shown in figure 1.1.

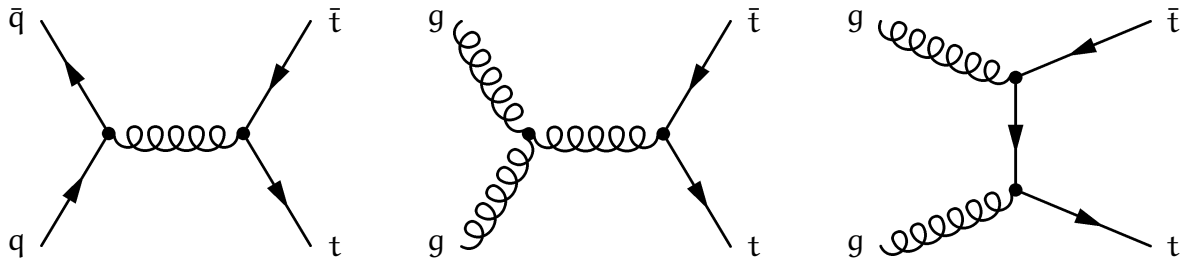

Figure 1.1: Examples for leading-order Feynman graphs contributing to $t\bar{t}$ production at a hadron collider.

The top quark decays before it can hadronize via the weak interaction into a W boson and a b quark. Decays to other down-type quarks are suppressed by the small off-diagonal CKM matrix elements. The decay modes of the W bosons determine the event signature. The *all-hadronic* category refers to $t\bar{t}$ events in which both W bosons decay to quarks, the *di-lepton* category if both W bosons decay to a charged lepton and a neutrino, and the *lepton+jets* or *semi-leptonic* category comprises events in which one W boson decays to a charged lepton and a neutrino and the other into quarks. The all-hadronic channel is hard to study due to the large background from QCD multijet production. The di-lepton channel allows a pure selection, but the two neutrinos in the final state complicate the kinematic reconstruction of the top quarks. The semi-leptonic channel, especially in case where the lepton is a muon or an electron, is considered the golden channel, as it allows both a selection of a pure sample and the reconstruction of the $t\bar{t}$ kinematic. This analysis uses the *muon+jets* channel; its branching fraction is given by the branching ratios of the W [35] and is 14.3%.

All properties of the top quark except of its mass are predicted by the standard model. The top quark is the most massive particle in the standard model. Its mass has been measured with very high precision: The latest combination of results of the Tevatron experiments yields $m_t = 173.18 \pm 0.94\,\text{GeV}$ [44], and CMS reports a consistent value of $m_t = 173.36 \pm 0.99\,\text{GeV}$ [45].

Many other properties of top quark production and decay are studied, and almost all measurements are in very good agreement with the standard model prediction.

The top quark pair production cross section has been calculated at next-to-leading order using MCFM and is $\sigma_{t\bar{t}} = 157.5 \pm 24\,\text{pb}$ for proton-proton collisions at $\sqrt{s} = 7\,\text{TeV}$, where the error includes uncertainties from the parton distribution functions and scale uncertainties. This value is in agreement with approximate next-to-next-to-leading order calculations [46] and measurements at the ATLAS and CMS experiments, which yield a combined value of $\sigma_{t\bar{t}} = 173 \pm 10\,\text{pb}$ [47].

Other examples of top quark property measurements at the LHC include the cross

section for the electroweak production of single top quarks [48–51] and searches for effects beyond the standard model, including searches for non-standard decays through flavor-changing neutral currents [52,53], and charge measurements excluding an exotic top quark charge of $\frac{4}{3}e$ [54, 55]. The results are in agreement with the predictions from the standard model.

One result with some tension to the standard model prediction is the charge asymmetry measurement in $t\bar{t}$ production. At the Tevatron, this can be observed as a forward-backward asymmetry in the detector frame and a positive asymmetry value corresponds to top quarks preferentially produced in the direction of the incoming proton, and the top anti-quarks in the direction of the anti-proton. Such asymmetries can only arise in an asymmetric initial state $q\bar{q}$. The standard model predicts a small asymmetry as a result of higher-order effects [56], while analyses at CDF [10–12] and DØ [7–9] observe deviations from the standard model predictions by more than 3σ. The charge asymmetry is harder to measure at the LHC, as $t\bar{t}$ events are produced primarily via a gg initial state and the symmetric proton-proton initial state requires the definition of a different observable, which exploits that for $t\bar{t}$ production via the relevant $q\bar{q}$ initial state, the quark tends to have larger z momentum than the anti-quark. The charge asymmetry measurements at the LHC [57–60] found no indication for deviations from the standard model, but the sensitivity to some of the BSM theories explaining the Tevatron result is very limited, and the charge asymmetry measurements at the Tevatron still provide ground for speculation for explanations beyond the standard model.

1.2.2 Beyond the Standard Model

To find an explanation for the forward-backward asymmetry observed at the Tevatron, a widely considered model are axigluons, e.g. in [13–16]. In axigluon models, the QCD gauge group is replaced by an extended group $SU(3)_L \times SU(3)_R$ with left-handed and right-handed couplings. This symmetry is spontaneously broken by some mechanism in analogy to the Higgs mechanism in the electroweak sector of the standard model. This symmetry breaking leads to the standard model QCD group $SU(3)_C$ with the well-known octet of massless gluons, and an octet of massive gluons, the axigluons. The strong coupling ensures a large production cross section and width of axigluons.

In the topcolor model [2], the QCD gauge group of the standard model $SU(3)_C$ is embedded into a larger gauge group $SU(3)_1 \times SU(3)_2$, where $SU(3)_1$ only couples to the first two quark generations, and $SU(3)_2$ only couples to the third generation. To be consistent with the current measurement, the $SU(3)_1 \times SU(3)_2$ symmetry is broken into $SU(3)_C$, creating 8 massive gluons known as *topgluons* that preferentially couple

to the third generation. The formation of a $t\bar{t}$ condensate is used as mechanism for electroweak symmetry breaking, replacing the Higgs mechanism. This model, however, has a fine-tuning problem in explaining the large mass difference between the top and the bottom quark. A mechanism to explain this mass difference naturally can be introduced by extending the hypercharge group of the standard model $U(1)_Y$ to $U(1)_1 \times U(1)_2$ in analogy to the $SU(3)$ extension discussed above, and $U(1)_1$ couples preferentially to the first and second generations, while $U(1)_2$ preferentially couples to the third generation. The breaking of this symmetry generates the topcolor Z', which couples preferentially to the third generation. Depending on the couplings of the new gauge groups, the Z' can have a negligible coupling to leptons, resulting in a *leptophobic topcolor* Z', while having a large enough coupling to the first quark generation to generate a visible cross section via $u\bar{u}$ and $d\bar{d}$. For the observable relevant in this analysis, $d\sigma(Z' \to t\bar{t})/dm^{t\bar{t}}$, the relevant free parameters of this model are the Z' mass and the natural width $\Gamma_{Z'}$; specifying those two parameter also determines the production cross section. In this analysis, this model is used with $\Gamma_{Z'} = 0.012 \times M_{Z'}$ and $\Gamma_{Z'} = 0.1 \times M_{Z'}$. The narrow model with 1.2% width has already been used at the Tevatron, e.g. in [19]. Recent analyses of Tevatron data exclude such a narrow topcolor Z' below masses of 900 GeV at 95% confidence level [18–20].

The huge difference of the energy scale of the electroweak theory around 10^2 GeV and the scale of the gravitation, the Planck scale, at 10^{18} GeV is known as the hierarchy problem, and it has inspired a number of models attempting to explain this scale difference naturally. One of such models is the Randall-Sundrum (RS) model [4], which is a generalization of the Kaluza-Klein model of extra dimensions. In the RS model, the space-time metric contains an exponential *warp* factor that explains the hierarchy without requiring fine-tuning or introducing additional arbitrary hierarchies. The RS model can also be used to explain the mass hierarchy of the standard model fermions, which is explained by placing the standard model fermions at different locations in the fifth dimension [5]. A prediction of this model are Kaluza-Klein excitation of the gluon, i.e. a gluon state with a non-zero mode in the fifth dimension, which decays in more than 90% to $t\bar{t}$. The natural width of the KK gluon is about 17%. For more details, see references [5, 61].

With the multitude of models, it is hardly possible to study all of them in detail. Instead, in this analysis, a generic model leading to a resonant contribution to $t\bar{t}$ production is used by assuming a Z' with couplings as the standard model Z, which is produced in the s channel via $q\bar{q}$ and always decays to $t\bar{t}$. The width is either set to 1% of $M_{Z'}$ or 10% of $M_{Z'}$. This allows to set limits which are valid for any resonance with a similar reconstructed invariant $t\bar{t}$ mass spectrum (which is affected by resolution effects), and it allows to set limits on the mass of a leptophobic topcolor Z' for the a width of 1.2% and 10%. In addition, the Kaluza-Klein gluon model

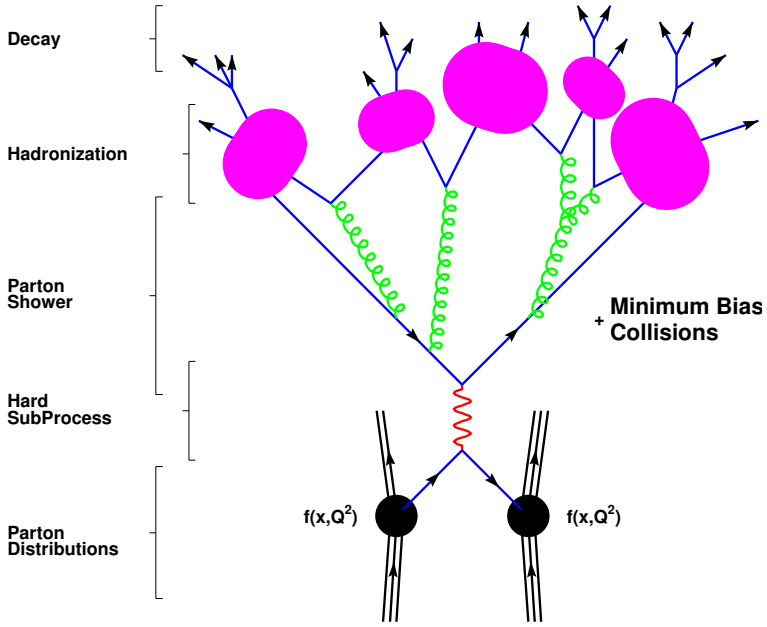

Figure 1.2: Events at hadron colliders [63].

from [5] is used to set cross section and mass limits. More details about the different Z' types are discussed in section 3.1.2.

1.3 Event Modeling

The comparison of data to theory prediction requires a comprehensive model of events at hadron colliders. The different steps and ingredients of a realistic event at a hadron collider are depicted in figure 1.2. The description in this section follows reference [62].

The protons are not fundamental particles of the standard model, and the cross section on the parton level has to be weighted by the parton distribution functions; the total cross section for the process $pp \to X$ is given by

$$\sigma_{pp\to X}(\mu_R, \mu_F) = \sum_{a,b} \int dx_a dx_b f_a(x, \mu_F) f_b(x, \mu_F) \hat{\sigma}_{ab\to X}(x_a, x_b, \mu_R), \tag{1.13}$$

where a and b denote the parton types (quarks, gluons), f_a are the parton distribution functions, and $\hat{\sigma}$ is the partonic cross section, which can be calculated perturbatively. This is known as the factorization ansatz. The parton distribution function $f_i(x)$ is the probability to find a parton of type i with momentum fraction x in the proton. It has a dependence on the *factorization scale* μ_F, which is introduced to

absorb large logarithms spoiling the perturbative convergence that appear in higher-order corrections in cases where a gluon is emitted approximately collinear to the incoming quarks. The partonic cross section has an explicit dependence on the *renormalization scale*, which is the scale the running coupling α_s is evaluated. Both the renormalization scale and the factorization scale are set to the typical momentum transfer in the process, such as the mass of the produced particle, its transverse momentum. They are unphysical parameters in the sense that in a hypothetical calculation of the cross section to all orders, the dependence on μ_R and μ_F would disappear. For a finite series, the cross section result depends on the chosen scales, and an uncertainty on the result is quoted by varying μ_R and μ_F up and down by some amount, e.g. by a factor of two.

Monte-Carlo event generators are used to sample from the integrand of equation (1.13), resulting in a representative sample of events, each consisting of a set of final state particles including their four-vectors, spin, color, which are used to study the process and develop the analysis. For many processes, tree-level matrix elements and cross sections can be calculated automatically with packages such as MadGraph [64], which can also generate a Monte-Carlo sample. This is known as the *matrix element* part of the simulation.

After the matrix element, the *parton shower* adds the dominant higher-order contributions to the hadronic process, which are collinear and soft gluon emissions and $g \to q\bar{q}$ splittings. After simulating the parton shower, the gluons and quarks form hadrons — a process that is not described perturbatively —, which subsequently decay. One implementation simulating the parton shower, hadronization, and decay is the program Pythia [65]. It also includes the simulation of other aspects of the *underlying event*, such as additional interactions between the proton remnants, leading to additional particles uncorrelated to the hard process. Many of these processes cannot be calculated perturbatively, and phenomenological models are used that are "tuned" to data using sensitive observables, e.g. the median jet energy per jet area in an event as a measure for the energy contribution of the underlying event [66].

The matrix element approach is suitable for modeling hard, large-angle radiation, whereas soft and collinear radiation is handled better by the parton shower program, as these lead to divergencies in the matrix element. Therefore, one can simulate a process with additional jets, e.g. Z+jets, by using tree-level matrix element simulation from MadGraph simulating Z+0 parton, Z+1 parton, Z+2 partons, ... Z+n partons. In this case, a potential double-counting of phase space can occur, as the parton shower might add the same radiation to the Z+0 parton sample, which is included in the matrix element of the Z+1 parton sample. To avoid this double counting a *matching* algorithm is used. For a review of different matching algorithms, see [67]. In this analysis, the MLM matching is used. After the parton shower, it clusters the

partons to jets and accepts the events only if each jet matches to a final state parton of the matrix element. This ensures that the parton shower part cannot generate additional jets, beyond what is included as partons in the matrix element already. One exception is the sub-sample with the highest parton multiplicity (Z+n partons), in which the parton shower is allowed to generate additional jets. This matching algorithm depends on the parameters used for the jet clustering, in particular the jet p_T threshold. This threshold is chosen such that the transition of the jet p_T spectra from matrix element to parton shower is smooth and depends on the process. The values used here are $p_T = 10\,\text{GeV}$ for W and Z production and $p_T = 20\,\text{GeV}$ for $t\bar{t}$ production. As this threshold is arbitrary to some extent, an uncertainty on the result is estimated by varying it up and down by a factor of two.

Finally, for a realistic simulation of additional inelastic proton–proton interactions within the same bunch crossing (pileup), a *minimum bias* process is simulated, which mainly relies on non-perturbative, phenomenological models of inelastic proton–proton scattering. This is also simulated with PYTHIA.

2 The CMS Detector and the LHC

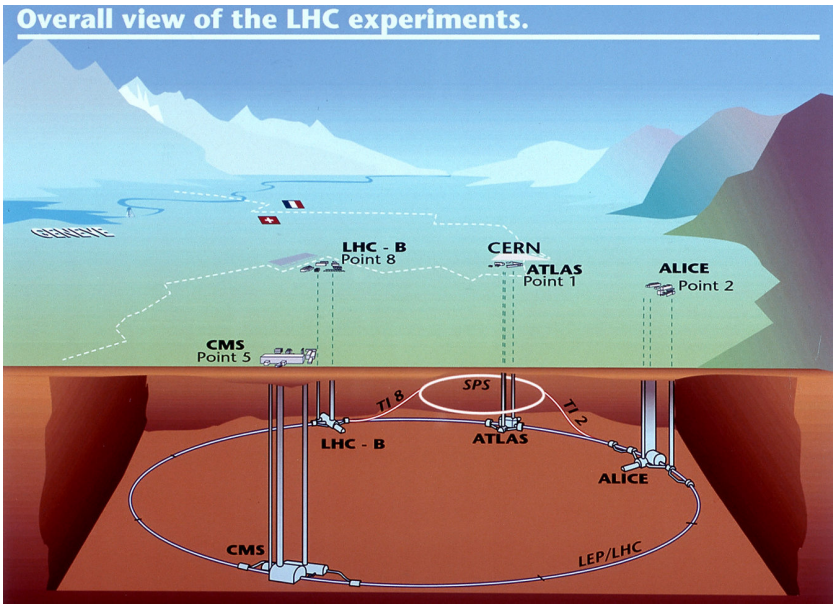

Figure 2.1: Overall view of the underground Large Hadron Collider ring with the four main detectors ATLAS, ALICE, CMS, and LHCb [68].

The analysis discussed in this thesis uses data from proton–proton collisions at the Large Hadron Collider (LHC), recorded by the Compact Muon Solenoid (CMS). This chapter introduces the LHC apparatus and the CMS detector and focuses on the features relevant for this analysis; more details can be found in the provided references.

2.1 The Large Hadron Collider

This section outlines some features of the Large Hadron Collider [69] and describes the LHC design parameters for an operation at 7 TeV proton beam energy, unless noted otherwise.

The LHC is the most powerful hadron collider, designed to collide proton beams with energies up to 7 TeV and lead ion beams with an energy up to 2.76 TeV per

nucleon. The main tunnel of the Large Hadron Collider is located at the Franco-Swiss border near Geneva, between 45 and 170 m below the surface, and it has a circumference of 26.7 km. The main tunnel was originally built for the Large Electron-Positron Collider (LEP), which operated from 1989 to 2000. An overall view of the LHC ring and the four main detectors is shown in figure 2.1. The proton and lead ion energy is limited by the strength of the magnetic dipole field required to bend the particle trajectories along the ring. For an energy of 7 TeV per proton beam, the field strength of the magnetic dipoles is 8.33 T. Due to space constraints in the tunnel, this magnetic field is not provided by two separate magnets, but by twin magnets producing two magnetic dipole fields of opposite field direction within the same mechanical support and cooling infrastructure. In total, 1232 dipole magnets and 392 quadrupoles are installed in the ring.

The LHC ring has eight straight sections, and at the center of each straight section are the points at which the proton beams can be brought to collision, labeled *point 1* to *point 8*. At four of these points, detectors are installed. Point 2 hosts A Large Ion Collider Experiment (ALICE) [70], which is specialized in studies of lead ion collisions, studying properties of the high density matter present when colliding lead ions. The LHCb detector [71] at point 8 is designed for studies of b quark production and decay in proton-proton collisions. The detectors ATLAS (A Toroidal LHC Apparatus) and CMS (Compact Muon Solenoid), located at point 1 and point 5 respectively, are general-purpose detectors focusing on studies of high-luminosity proton-proton collisions.

In many cases, the sensitivity of searches for a rare process — as the one studied in this thesis — are mainly limited by the production rate of the new process. The cross section of a heavy particle typically rises with the center-of-mass energy $\sqrt{s}$, which is chosen as high as the LHC machine technology allows. For a given $\sqrt{s}$, the key performance parameter for an accelerator determining the production rate is the instantaneous luminosity L: The number of events per second N is given by $N = L\sigma$ for a process with cross section σ. Cross sections for some standard model processes and the corresponding production rates are given in figure 2.2. The instantaneous luminosity L does not depend on the physics process but is a machine parameter determined by the beam geometry; high luminosities require high-intensity beams with small transverse beam areas. The design luminosity of the LHC is $10^{34}\,\mathrm{cm}^{-2}\mathrm{s}^{-1}$. The protons in the beams are arranged in up to 2808 bunches per beam with $1.1 \cdot 10^{11}$ protons per bunch and a bunch spacing of 25 ns.

The proton acceleration is performed in several steps by different accelerators, as sketched in figure 2.3. The protons for the LHC are accelerated by the Linac 2, the Proton Synchrotron Booster (PBS), the Proton Synchrotron (PS), and the Super Proton Synchrotron (SPS), which provides proton bunches for the LHC with an energy of

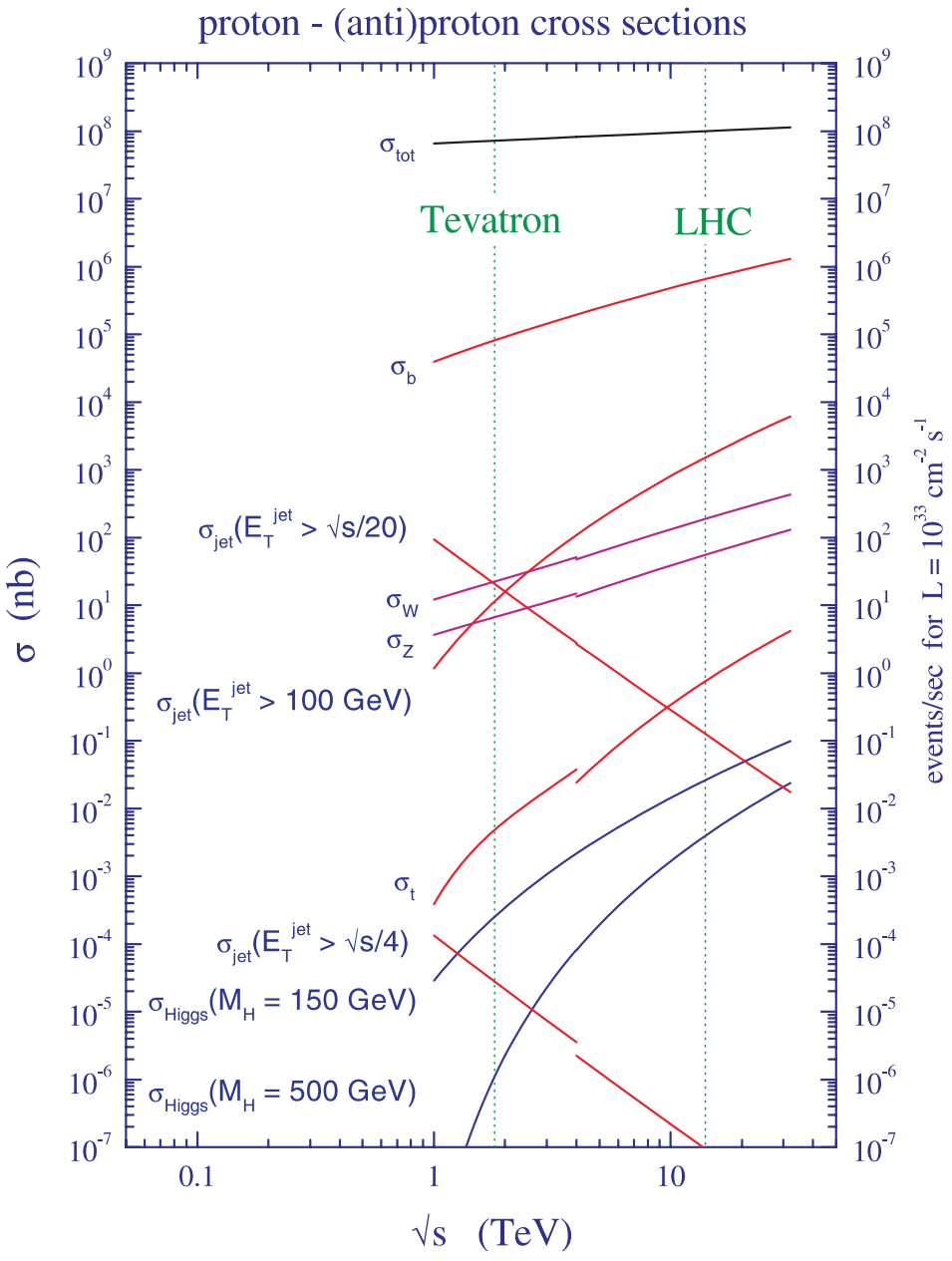

Figure 2.2: Next-to-leading order cross sections (left axis) and event rates (right axis) for various standard model processes for proton-antiproton ($\sqrt{s} < 4\,\text{TeV}$) or proton-proton collisions ($\sqrt{s} > 4\,\text{TeV}$) [62]. The event rates are given for an instantaneous luminosity of $10^{33}\,\text{cm}^{-2}\text{s}^{-1}$, which is ten times smaller than the design luminosity and 3.5 times smaller than the maximum instantaneous luminosity reached during 2011.

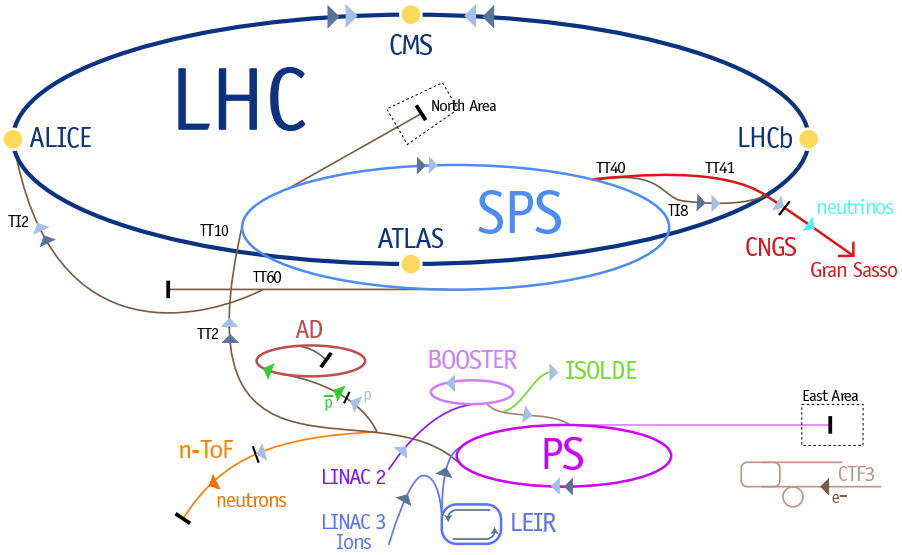

Figure 2.3: Schematic of the accelerators related to the LHC [72]. The LHC is filled with protons accelerated by Linac 2, Booster, PS, and SPS.

450 GeV. After beam injection, the protons are accelerated using radio frequency cavities in the LHC, which increase the proton energy by 0.5 MeV per turn.

During the commissioning of the LHC magnets on September 19$^{\text{th}}$ 2008, a malfunction in the interconnection of a dipole and quadrupole magnet caused an electrical arc, leading to the heating of the liquid helium [73]. The helium could not be released fast enough by the relief valves and the high pressure caused severe damage, and 37 magnets had to be replaced by spares [74]. In the investigation of this incident, a number of copper interconnections with an abnormally large resistance have been found, and it was decided to operate the LHC at 3.5 TeV beam energy [75]. The current analysis uses data taken in 2011. During that time, the LHC has been operated with a beam energy of 3.5 TeV using up to 1380 bunches per beam and bunch intensities of up to $1.4 \cdot 10^{11}$ protons per bunch, and a peak instantaneous luminosity of $3.5 \cdot 10^{33}\,\text{cm}^{-2}\text{s}^{-1}$ [76].

2.2 The CMS Detector

The Compact Muon Solenoid detector [77, 78] is shown in figure 2.4. It is 22 m long, 15 m high, and weighs about 12 500 t. A main feature of CMS is its large superconducting solenoid with a diameter of 6 m enclosing the calorimeter systems,

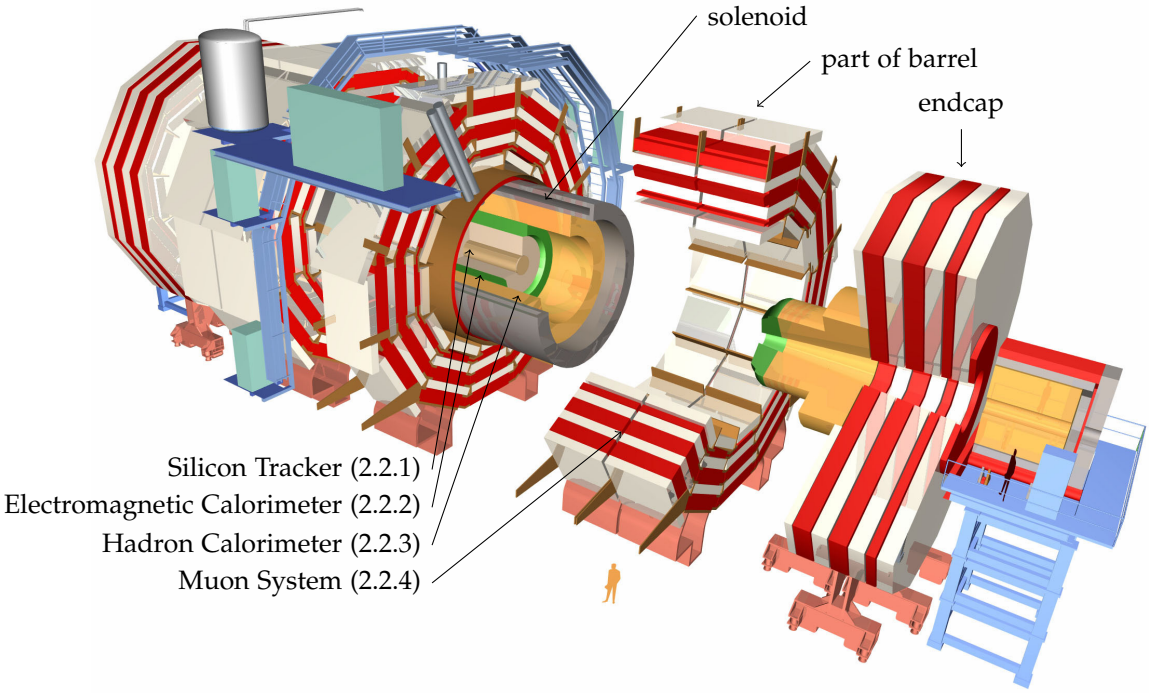

Figure 2.4: The CMS detector at the LHC [79]. It is divided into the central barrel and two endcaps and has a length of 22 m and a diameter of 15 m. The subdetectors are described in the given sections.

leading to a "compact" design. The solenoid produces a homogeneous magnetic field of 3.8 T parallel to the beam axis, which allows the momentum measurement of charged particles in the inner tracker by bending their trajectories.

The main requirements for the design of the CMS detector are a good muon identification and momentum resolution, a good momentum and position resolution for charged particles for b tagging, good electromagnetic energy resolution, and a good dijet mass and missing transverse energy resolution, all with a large geometric coverage. The main experimental challenges include the high levels of radiation in the inner and forward parts of the detector and the large collision rates of up to 40 MHz for operating at LHC design parameters, leading to high trigger rates and data volumes. These requirements and challenges are addressed by the design of the subdetectors of CMS discussed in the next sections.

The coordinate system of CMS has its origin at the center of the detector at the nominal interaction point with the x axis pointing towards the center of the LHC ring, the y axis pointing upwards, and the z being parallel to the counterclockwise beam direction. The polar angle θ is measured from the z axis and the azimuthal

angle ϕ is measured in the x-y plane. The cylindrical coordinate system uses z, ϕ, and the radius r measured in the x-y plane. The pseudorapidity η is defined as

$$\eta = -\ln \tan \frac{\theta}{2}. \tag{2.1}$$

For massless particles, it coincides with the rapidity y, defined as

$$y = \frac{1}{2} \ln \frac{E + p_z}{E - p_z}, \tag{2.2}$$

which has the property that differences in rapidity are invariant under Lorentz transformations along the z axis. This is useful for hadron collisions as it allows to define observables independent of the z momentum of the initial state, which is random in each event according to the parton distribution functions.

2.2.1 Silicon Tracker

The innermost subdetector is the silicon tracker [78, 80], used to reconstruct the helix trajectories of charged particles in the magnetic field, allowing the measurement of particle momenta and the reconstruction of vertices, which is discussed in section 3.2.1. It covers the pseudorapidity range $|\eta| < 2.4$.

Experimental challenges arise from the high particle flux from the interaction region, requiring a radiation-hard design. To keep the number of channels at a managable level, the outer regions are equipped with strip sensors, while the inner part is instrumented with pixel sensors. The overall tracker layout is shown in figure 2.5.

The pixel detector in the inner part comprises three barrel layers at radii of 4.4, 7.3, and 10.2 cm with a length of 53 cm each. The two endcaps per side are located at $|z| = 34.5$ cm and $|z| = 46.5$ cm and extend in r from 6 to 15 cm. The pixel size is $100 \times 150\,\mu m^2$. Through the Lorentz force, the charge generated from a particle traversing the sensor is shared among neighboring pixel sensors, increasing the resolution up to 10 µm for the r and ϕ coordinates and 20 µm for the z coordinate. The pixel sensor has a total of 66 million pixels, covering an area of about $1\,m^2$.

The strip detector is divided into an inner part and outer part, both divided further into the barrel part and discs that cover the forward region. These four parts are called TIB (Tracker Inner Barrel), TID (Tracker Inner Disks), TOB (Tracker Outer Barrel), and TEC (Tracker Endcaps). The TIB consists of 4 layers, extends up to $|z| = 65$ cm, and uses silicon sensors with a pitch between 80 and 120 µm. In general, the strips are parallel to the z axis, thus providing measurements for r and z. The inner two layers contain *stereo* modules, which are made up of two strip modules

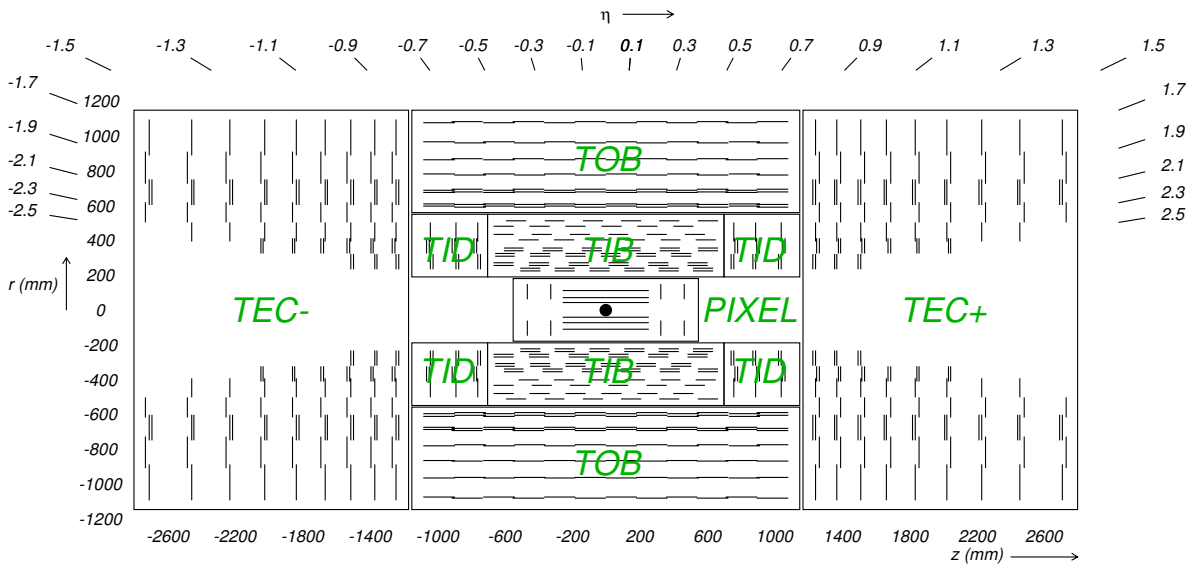

Figure 2.5: Schematic of the CMS inner silicon tracker [77]. Each line corresponds to a detector module, double lines indicate stereo strip modules.

with an angle of 100 mrad between the strips, thus providing also a measurement for ϕ. The single-point resolution is 23–34 µm. The TOB consists of 6 layers and extends to $|z| = 110$ cm. It uses strip pitches between 120 and 180 µm. As for the TIB, the first two layers are stereo modules, and the single point resolution is 35–52 µm. The TID comprises three disks, filling the gap between the TIB and TEC. Each part of the TEC consists of 9 disks in the region $120\,\text{cm} < |z| < 280\,\text{cm}$. The total number of strips is around 9.6 million, with a total area of about 200 m^2.

2.2.2 Electromagnetic Calorimeter

The electromagnetic calorimeter (ECAL) [78, 81] consists of nearly 80 000 scintillating crystals of lead tungstate ($PbWO_4$). The material was chosen because of its short radiation length of $X_0 = 0.89$ cm and because it is a fast scintillator: 80% of the light is emitted within 25 ns. The crystals have a length of 230 mm in the barrel and 220 mm in the endcap, corresponding to $25.8X_0$ and $24.7X_0$, respectively. Each crystal is instrumented with either silicon avalanche photodiodes in the barrel or vacuum photodiodes in the endcaps.

The inner radius of the barrel is 129 cm and covers the pseudorapidity up to $|\eta| = 1.479$. It comprises 36 "supermodules" spanning half of the barrel in z direction and 20° in ϕ direction. The crystals almost point to the nominal interaction point at the center of the detector, but are slightly tilted by 3° to avoid particle trajectories

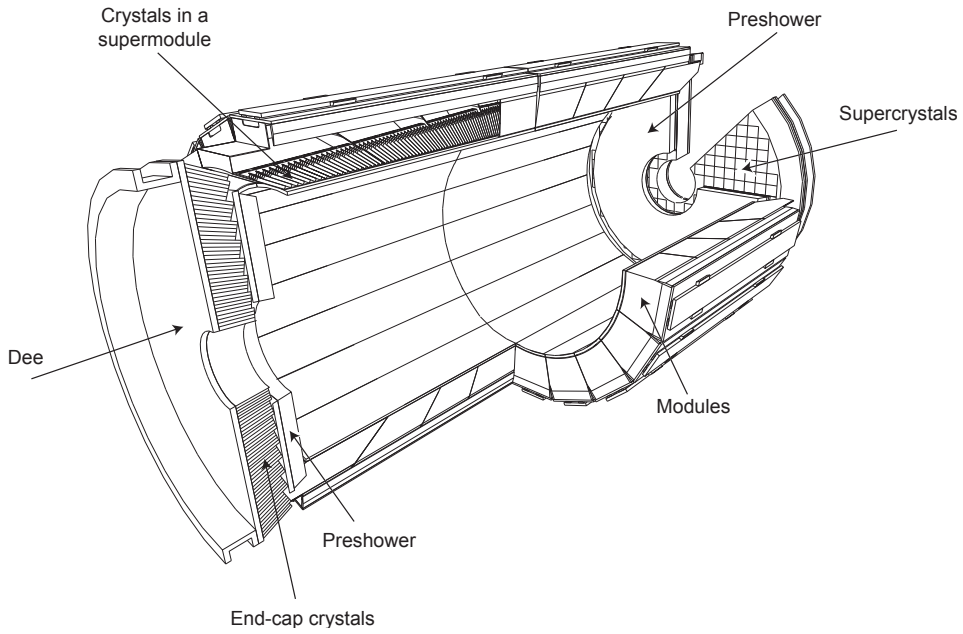

Figure 2.6: The electromagnetic calorimeter of CMS [77].

coinciding with the boundary between two crystals, which would degrade the response. The crystals have a front cross section of about $22 \times 22\,\mathrm{mm}^2$ and cover $\Delta\phi = \Delta\eta = 0.0174$.

The endcaps are located at $|z| = 314\,\mathrm{cm}$, covering the region up to $|\eta| = 3.0$. Each endcap consists of two semicircular aluminum structures, called "Dees". The crystals are arranged in a x-y structure and have identical cross sections of $28.6 \times 28.6\,\mathrm{mm}^2$. The preshower detector in front of the endcaps covers $1.65 < |\eta| < 2.61$ and provides good angular resolution that allows to separate single photons from neutral pions π^0 that decay to two almost collinear photons. It contains two layers of lead converters with 3 radiation lengths.

Around 99% of the channels of the barrel and endcap and about 95% of the channels in the preshower detector have been operational in 2011, and the observed resolution in data agrees with the expected resolution from test-beam measurements and simulation [82]. The relative energy resolution σ_{rel} for electrons hitting the center of a crystal can be parametrized as

$$\sigma_{\mathrm{rel}}(E) = \frac{2.8\%}{\sqrt{E}} \oplus \frac{12\%}{E} \oplus 0.3\%, \tag{2.3}$$

where E is the electron energy measured in GeV, and the symbol $\oplus$ denotes the square root of the quadratic sum, as required for the Gaussian error propagation, i.e.

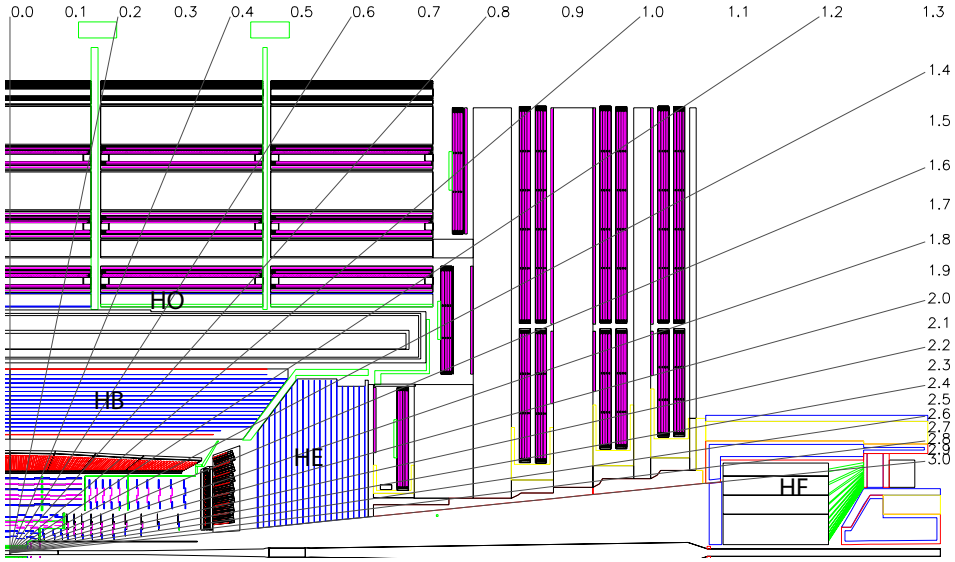

Figure 2.7: The hadron calorimeter at CMS, comprising the barrel (HB), endcap (HE), outer (HO), and forward (HF) parts [77].

$a \oplus b := \sqrt{a^2 + b^2}$.

2.2.3 Hadron Calorimeter

The Hadron Calorimeter (HCAL) [78, 83] surrounds the electromagnetic calorimeter. The HCAL design is driven by the magnet and the requirement to provide hermetic coverage; a sketch is shown in figure 2.7. The absorber material is brass, which is non-magnetic, easy to process, and has a reasonably short radiation length. The active material consists of plastic scintillators read out with wavelength-shifting fibers.

The Hadron Barrel (HB) covers the pseudorapidity range up to $|\eta| = 1.4$, extending radially from $r = 1.806$ to 2.95 m. It has a segmentation of $\Delta\eta = \Delta\phi = 0.087$, resulting in 2304 towers. In total 15 brass plates, each about 5 cm thick, are interleaved with the plastic scintillator plates of 3.7 mm thickness. The Hadron Outer (HO) is located outside of the solenoid, covering the region $|\eta| < 1.26$. It uses the magnet coil as additional absorber material and thereby extends the effective thickness of the Hadron Calorimeter to over 10 hadron radiation lengths. The Hadron Endcaps (HE) comprise 14 η segments each, covering the region $1.3 < |\eta| < 3.0$. The segmentation in η is 0.087 for the inner part at small $|\eta|$ and increases to 0.35 for the outermost part. The Hadron Forward (HF) calorimeter measures hadrons in the forward region and covers a substantial pseudorapidity range of $|\eta|$ between 3.0 and 5.0, which is important for the measurement of missing transverse energy. It is located at

$|z| = 11.2\,\mathrm{m}$ and the absorber depth is 1.65 m. The segmentation is between $\Delta\eta \approx 0.1$ for the lowest-η tower, $\Delta\eta \approx 0.175$ for the towers between, and $\Delta\eta \approx 0.3$ for the highest-η tower. The ϕ segmentation is $\Delta\phi = 0.175$, except for the highest-η tower, where it is $\Delta\phi = 0.35$.

The relative energy resolution for the HCAL is expected to be

$$\sigma_{\mathrm{rel}}(E) = \frac{100\%}{E} \oplus 5\% \tag{2.4}$$

where E is the energy of the particle in GeV. This resolution was confirmed in first data [84] and is also confirmed by the resolution of the jet energy and the missing transverse energy discussed in section 3.2.

2.2.4 Muon System

The muon system at CMS [78, 85] is located outside of the solenoid, interleaved with the iron return yoke. As shown in figure 2.8, three types of gas detectors are used: Drift Tubes (DT), Resistive Plate Chambers (RPC), and Cathode Strip Chambers (CSC).

Drift tubes are used in the barrel region, roughly covering $|\eta| < 1.3$, where the particle flux is relatively low. The drift tubes are arranged in chambers MB1 to MB4 at radii of about 4.0, 4.9, 5.9 and 7.0 m, separated by the iron flux return yoke. The three inner chambers consist of 12 layers of drift tubes, the first and last four measure r and ϕ, while the inner four provide measurements for r and z. The outermost station comprises 14 tube r-ϕ measuring layers. The single-point resolution for each tube is about 250 µm, leading to a resolution of 100 µm per chamber and a time resolution of a few nanoseconds. One or two resistive plate chambers are coupled to each DT chamber, which provide additional timing information and allow muon track building at the trigger level.

The endcap region uses cathode strip chambers, covering $0.9 < |\eta| < 2.4$, arranged in four stations ME1 to ME4. Cathode strip chambers can cope with the higher magnetic field and particle rates in that region. Each station comprises two or three layers of chambers, arranged to maximize coverage on all possible muon paths. There are different types of chambers, covering azimuth angles of either 10 or 20°. Each chamber comprises six layers of cathode panels with radial strips and six anode panels with parallel wires approximately perpendicular to the cathode strips, thus providing six measurements of r and ϕ per chamber. The position resolution is between 75 and 150 µm.

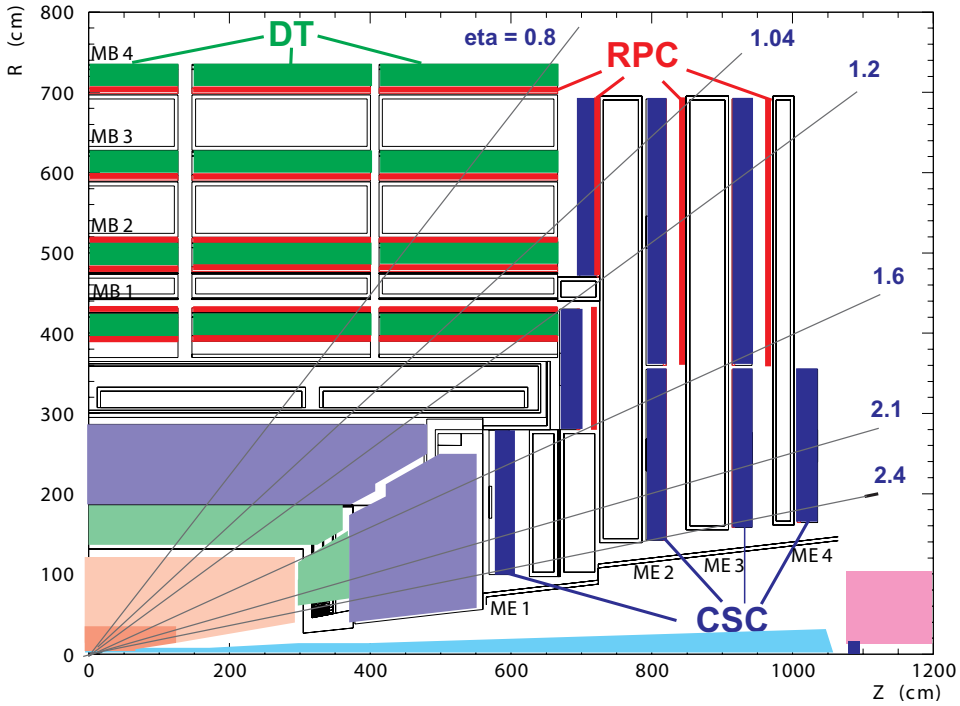

Figure 2.8: The muon detectors of CMS: Drift Tubes (CT), Resistive Plate Chambers (RPC), and Cathode Strip Chambers (CSC) [78].

2.2.5 Trigger and Data Processing

The main challenge for the data taking is the large bunch crossing rate of 40 MHz. To keep the event rate at a manageable level in terms of both storage and computing power requirements, a trigger is used, which selects a subset of events for further storage and processing. The trigger at CMS [77,78,86,87] consists of two levels. The *level-1* trigger reduces the data rate to under 100 kHz. This trigger is implemented using custom hardware and has to reach a trigger decision within 3.2 µs of the bunch crossing. The trigger decision is based on primitive trigger objects, provided by the calorimeter and muon trigger subsystems. Only if the level-1 trigger fires, the event data is read out from the detector. The event data is zero-suppressed, i.e. only channels with non-vanishing signal are kept, and the remaining data of about 1 MB per event is sent to the surface, where the second level of the trigger decision, the *high-level trigger* (HLT), is performed. The HLT is implemented in a computing farm running a special version of the CMS reconstruction software. It has around 20 ms CPU time to reach a trigger decision and reduces the trigger rate to under 400 Hz.

Events accepted by the HLT are divided into around 20 primary datasets based

on the trigger decision and sent to the Tier-0 computing center at CERN, where a *prompt reconstruction* is performed within hours of data taking. To meet the large demands for computing power and storage, CMS uses a distributed computing model [88]. The recorded data is distributed from the Tier-0 to Tier-1 and further to the smaller Tier-2 computing centers. The main function of the seven Tier-1 centers is the storage, reconstruction, and further distribution of data. Tier-1 centers are also used to run the simulation of collision events. The total storage space used by CMS at Tier-1 centers in 2011 was slightly above 40 PB, and used a computing power of around 100 000 HEP-SPEC06 units [89], where modern CPUs have around 10 HEP-SPEC06 per core [90]. There are about 50 Tier-2 computing centers, which are used for centrally managed simulation and by individual physicists accessing the reconstructed datasets for their analyses, who in general do not have access to Tier-0 and Tier-1 resources.

The data taking is separated into runs comprising a consistent configuration of the data taking, including trigger settings, and a run can last several hours. Each run is further divided into *luminosity sections* (LS) lasting 23.3 s, in which the instantaneous luminosity and other machine parameters are considered to be constant. The instantaneous luminosity is measured during data taking using the energy or occupancy of the hadron forward calorimeter [77,78,91], which are proportional to the instantaneous luminosity. The absolute luminosity normalization is provided by Van-der-Meer scans [92], which measure the effective beam area by displacing the beams along the x/y axes. For physics analyses, a luminosity based on pixel cluster counting [93] is used, which is affected by fewer nonlinearity effects and less calibration drift than the HF-based luminosity measurement. It is also normalized using the Van-der-Meer scans and provides luminosity with a total uncertainty of 2.2%. Recorded data undergoes a validation procedure in which a list of runs and luminosity sections is created during which all detector components were operational; this reduces the amount of data available for analyses. As the data acquisition of CMS (DAQ) and the trigger are not always operational and have some non-zero dead time by design, it is common to cite three different values for the integrated luminosity: The *delivered* luminosity is the one provided by the LHC, the *recorded* luminosity refers to the stored dataset, corrected for dead time and DAQ downtime, and the *certified* luminosity contains only validated luminosity sections. The delivered integrated luminosity as a function of time in 2011 is shown in figure 2.9. This analysis uses the single-muon primary dataset. It corresponds to a certified integrated luminosity of $5.0 \pm 0.1\,\text{fb}^{-1}$.

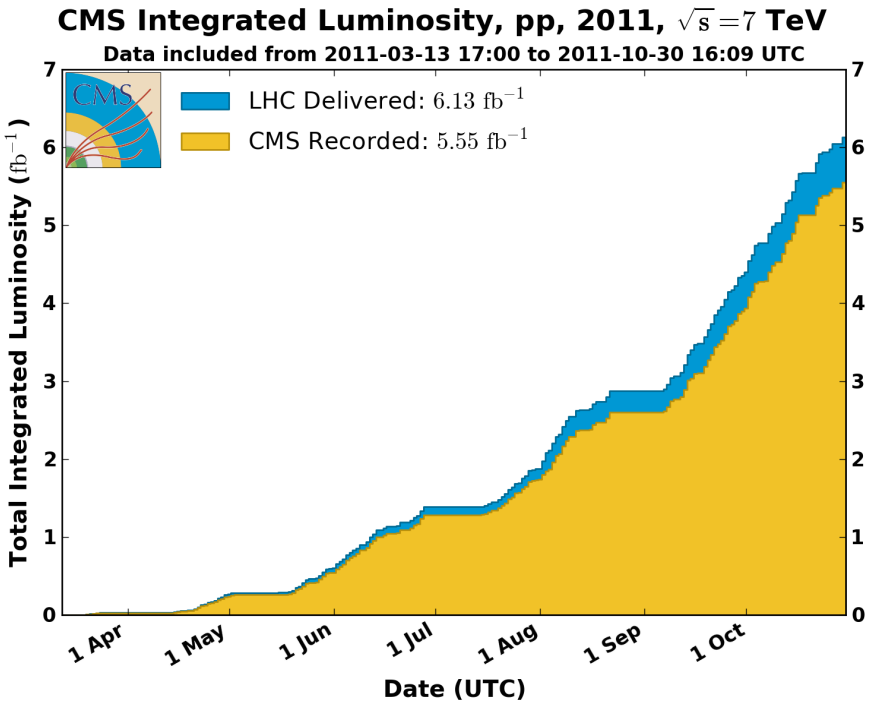

Figure 2.9: The delivered and recorded integrated luminosities at CMS as a function of time in 2011 [94]. This analysis uses the certified subset of the recorded data, which corresponds to $5.0 \pm 0.1\,\text{fb}^{-1}$.

3 Event Simulation and Reconstruction

The analysis method relies on a realistic prediction of the properties of signal and background events. This is done with a detailed simulation of events based on theory calculation and is described in section 3.1. The reconstruction algorithms applied to the low-level detector response of simulated and recorded events in order to obtain high-level physics objects are discussed in section 3.2. Known differences between recorded and simulated events can be accounted for by applying corrections to the simulated events, which are discussed in section 3.3. The chapter concludes with section 3.4 pointing out the systematic uncertainties related to both the theory predictions as well as to the reconstruction algorithms introduced earlier in this chapter.

3.1 Event Simulation

The event simulation described in this section provides a realistic sample of events on detector level for different background and signal processes used in this analysis. It starts with the generation of events at the parton level, including the underlying events, the parton shower, hadronization, and decay as discussed in section 1.3. The result of this step is a set of events, each consisting of a list of those long-lived particles that typically reach the detector, including charged kaons and pions. These are used as input to a detailed CMS detector simulation based on GEANT4 [95], which includes propagating the particle trajectories in the magnetic field, the decay of the long-lived particles, and the detailed simulation of the interaction of detector material with the particles resulting in the detector response. On a technical level, the result of this simulation is the low-level detector response in the same format as for actual data, and the same reconstruction algorithms can be applied for both simulated and recorded events.

A realistic event simulation requires to include additional inelastic proton-proton interactions within the same or adjacent bunch crossings, known as *pileup*. Pileup events in the same bunch crossing (in-time pileup) give rise to additional low-p_T charged and neutral particles originating from additional vertices. Out-of-time pileup events in adjacent bunch crossings, i.e. 50 ns before or after the current bunch crossing, contribute to energy in the calorimeter readout, as the readout extends to these bunch crossings; the contribution from pileup events more than 50 ns before or after the

primary bunch crossing can be neglected. Pileup events are included by simulating minimum bias events using Pythia as generator and mixing pileup events with the simulated event of the primary interaction discussed in the previous paragraph.

A weight is assigned to the simulated events such that the weighted number of events corresponds to the number of events expected from the integrated luminosity and the cross section. The event weight is thus

$$w = \frac{L\sigma}{N_{sim}}, \tag{3.1}$$

where L is the integrated luminosity of the dataset one wants to scale to, σ is the cross section of the simulated process and N_{sim} is the number of simulated events for this process. The event weight is modified by multiplying additional event weights to correct for known differences between data and simulation, as will be discussed in section 3.3.

3.1.1 Background Processes

The standard model background processes for events in the muon+jets channel fall into two classes for which different strategies are employed: The first class comprises background processes with a muon in the final state of the hard interaction, *prompt muons*. This background is modeled with simulated events, making use of theory predictions. The second class of background processes comprises events containing a reconstructed non-prompt muon, i.e. muons from heavy flavor decays, decay-in-flight muons, or wrongly reconstructed muons. This background process is referred to as *QCD multijet*. The QCD multijet background is hard to model as the underlying $2 \to 2$ process has a large cross section, but the probability to find muons in such events is very low and not well-known. Therefore, the strategy for the QCD multijet background is to reduce it as much as possible by applying appropriate event selection criteria and to estimate the remaining fraction of QCD multijet events with methods, using data sidebands, not relying on the event simulation.

The background processes with prompt muons include the irreducible QCD $t\bar{t}$ production introduced in section 1.2.1. Events are generated with MadGraph 5 [64] with up to three final state partons beyond the $t\bar{t}$ final state. Parton showering is performed with Pythia 6.4 [65], and the MLM algorithm introduced in section 1.3 is used to do the matching between the matrix element and the parton shower. The same combination of MadGraph and Pythia is used for the simulation of the W+jets and Z/γ^*+jets background processes, which are another important source for prompt muons. In these cases, up to four partons in the final state are included in the matrix element. Examples for tree-level Feynman graphs for these processes are shown in

figure 3.1. In both cases, only leptonic decays of the vector boson are included in the simulation. For the Z/γ^*+jets background, a requirement for the invariant dilepton mass of $m_{\ell\ell} > 50\,\text{GeV}$ is applied to remove the infrared-divergent component at low $m_{\ell\ell}$, which does not contain high-p_T leptons contributing to the muon+jets topology anyway. The electroweak production of single top quarks is another source for prompt muons. There are three production modes for single top quark events, single top quarks in association with a W boson, t channel, and s channel, where "t" and "s" are Mandelstam variables referring to the four-momentum-square of the W boson in the respective leading-order Feynman graphs. Some leading-order Feynman graphs for t channel and associated tW production are shown in figure 3.2. The s channel single top quark production has a low cross section and is not considered in this analysis. Single top quark events in the t channel and associated tW production are generated with the next-to-leading order POWHEG [96–100] event generator and showered with PYTHIA. Events with more than one W/Z boson in the final state have a negligible contribution compared to the other processes and are therefore not considered in this analysis. All top quark processes use a top quark pole mass $m_{\text{top}} = 172.5\,\text{GeV}$; the used parton distribution function is the appropriate leading-order or next-to-leading order variant of the CTEQ6 pdf sets [101]. The PYTHIA parameters governing the modeling of multiple interactions and underlying event are set according to the tune Z2 [102]. The renormalization and factorization scale for $t\bar{t}$ (W/Z) simulation with MadGraph are different for each event and set to $Q^2 = m^2 + \sum_i p_{T,i}^2$, where m is the top quark mass (W/Z mass), and i loops over all final state partons simulated in addition to the $t\bar{t}$ (W/Z) final state.

While the QCD multijet background is estimated from data sidebands for the final event selection, a simulated sample of QCD multijet production is still used in order to develop the event selection and make cross-checks for the QCD multijet estimation technique. The simulated sample uses PYTHIA to generate QCD $2 \to 2$ processes with $\hat{p}_T > 15\,\text{GeV}$, allowing all gluons and quarks (except top quarks) in the final state. After hadronization and decay, but before the detector simulation, a filter is applied that only keeps events in which a muon with $p_T > 15\,\text{GeV}$ and $|\eta| < 2.5$ is found.

The cross sections and the numbers of simulated events for all background processes are summarized in table 3.1. In case of QCD $t\bar{t}$, W+jets and Z/γ^*+jets, the cross sections are next-to-leading order values calculated with MCFM 5.8 [103]. The cross sections for single top quark production in the t channel and tW production are approximate NNLO results from references [104, 105]. In all cases, the uncertainties include uncertainties from parton distribution functions, α_s uncertainties, and scale uncertainties. The cross section for the QCD multijet process is a leading-order result from PYTHIA for which no uncertainty has been evaluated. The uncertainties

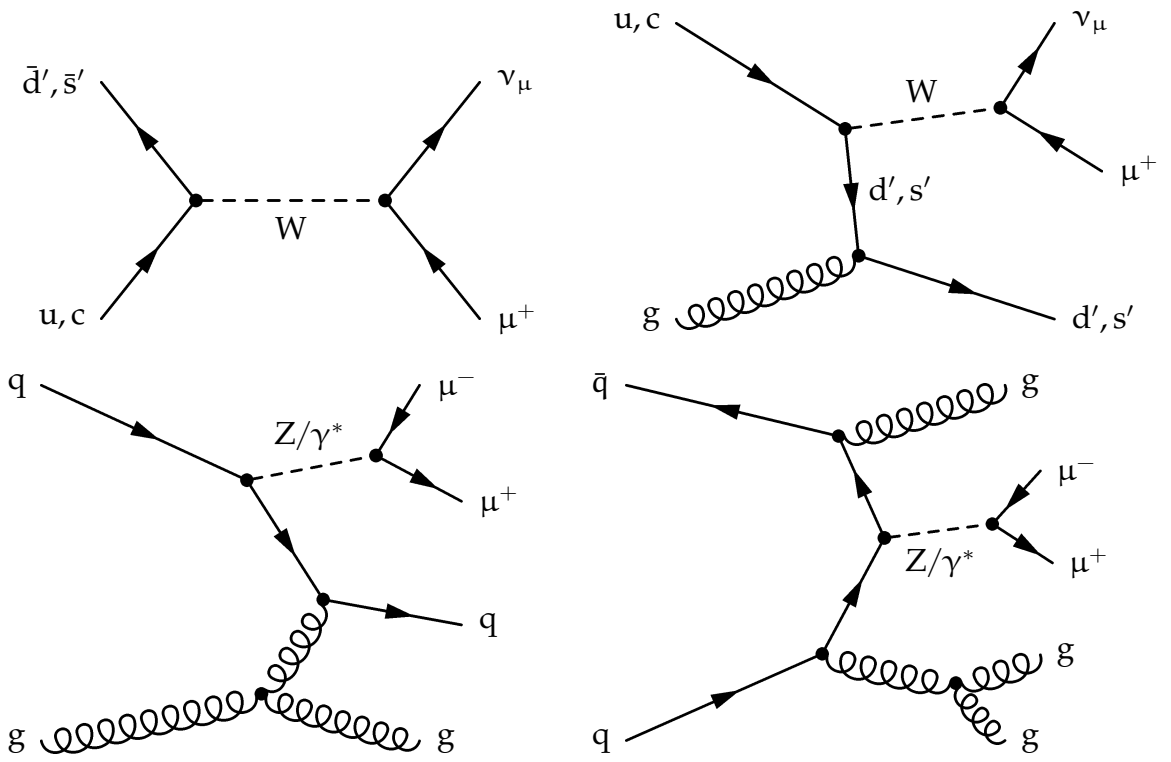

Figure 3.1: Example Feynman graphs for W+jets and Z/γ^*+jets production with different final state parton multiplicities included in the simulation.

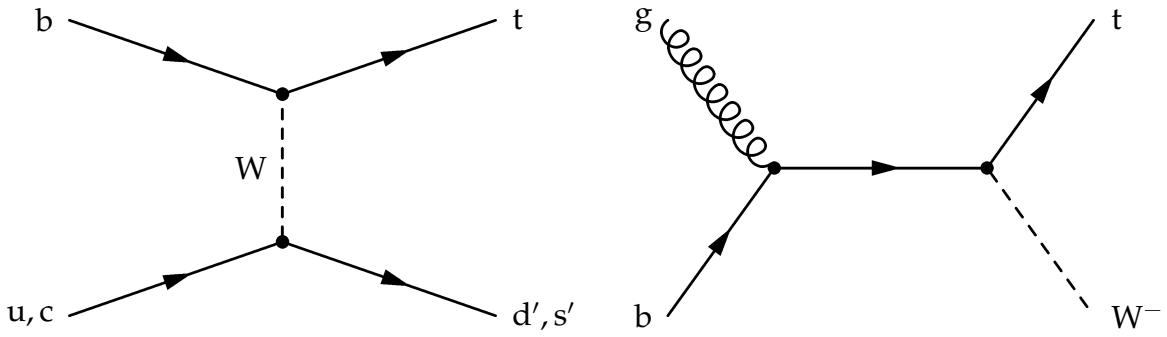

Figure 3.2: Example Feynman graphs for single top quark production in the t channel (left) and in association with a W boson (right).

Process	Cross Section (pb)	Sim. Events (10^6)
QCD $t\bar{t}$	157.5 ± 24	59.5
$W \to \ell\nu$+jets	$31\,314 \pm 1558$	81.3
$Z/\gamma^* \to \ell\ell$+jets	3048 ± 132	36.1
Single-Top t channel	64.6 ± 2.6	5.8
Single-Top associated tW production	15.7 ± 1.2	1.6
QCD multijet (μ-enriched)	84 679	20.4

Table 3.1: The cross sections and numbers of events of the simulated background processes.

used in the statistical evaluation have additional contributions and are discussed in section 3.4.

3.1.2 Signal Processes

The Z' signal events are generated according to the process $q\bar{q} \to Z' \to t\bar{t}$ in the s channel. They use the same top quark mass, underlying event tune, and parton distribution function as the background processes discussed in the previous section. Three different signal types have been simulated, *narrow* Z' with a natural width $\Gamma = 0.01 \times M_{Z'}$, *wide* Z' with $\Gamma = 0.1 \times M_{Z'}$, and the *KK-Gluon* process introduced in section 1.2.2. The narrow and wide Z' samples have been generated with the same combination of MadGraph and Pythia used as for the QCD $t\bar{t}$ process, including the generation of up to three additional partons in the final state of the matrix element. The Kaluza-Klein sample was generated with a leading-order implementation in Pythia 8 [106], and a fast simulation relying on parameterizations of the CMS detector response rather than on the detailed but time-consuming simulation with Geant4 has been used in this case. For all three signal types, samples have been generated for $M_{Z'} = 1, 1.5, 2$, and 3 TeV; for the narrow Z', an additional sample with $M_{Z'} = 1.25$ TeV was generated.

The distribution of the generated invariant $t\bar{t}$ mass $m_{t\bar{t}}^{gen}$ for the different signal types is shown in figures 3.3 and 3.4. For large $M_{Z'}$, there is a tail towards lower generated invariant $t\bar{t}$ masses $m_{t\bar{t}}^{gen}$. This tail results from the large partonic luminosity at these low values for $\hat{s} = m_{t\bar{t}}^{gen}$, corresponding to virtual Z'.

The narrow Z' sample has a natural width of 1%, which is much smaller than the experimental resolution for the reconstructed invariant $t\bar{t}$ mass $M_{t\bar{t}}$ of 6% to 10% (see section 4.2). Therefore, the width of the $M_{t\bar{t}}$ peak — which is given by the

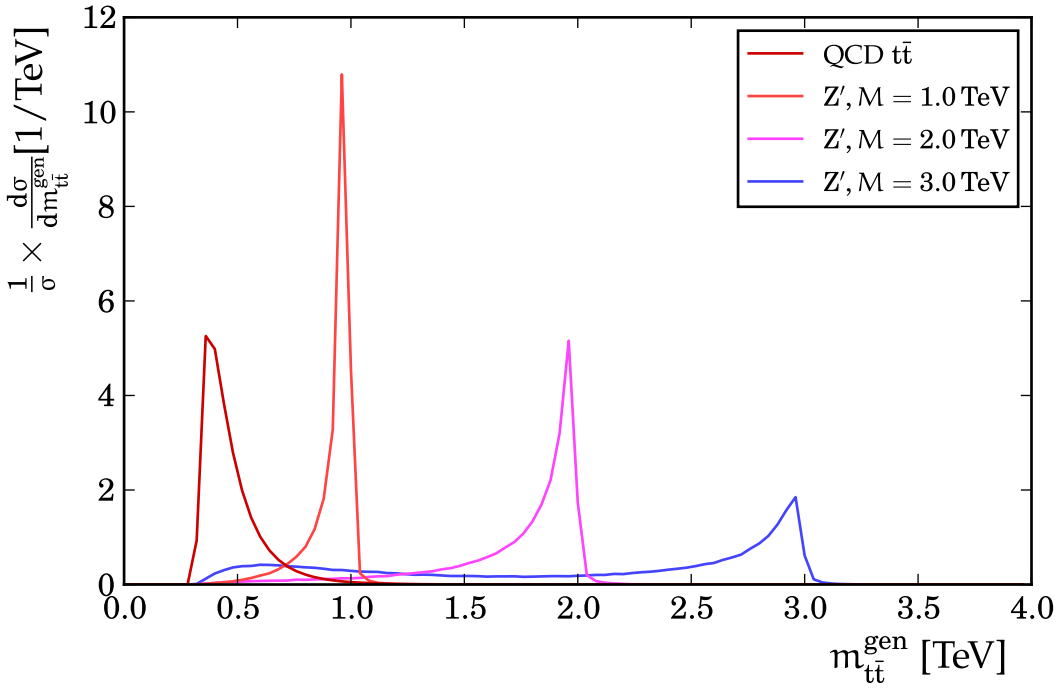

Figure 3.3: Distribution of the generated invariant $t\bar{t}$ mass $m_{t\bar{t}}^{gen}$ for the *narrow* Z' signal and standard model QCD $t\bar{t}$ production for different $M_{Z'}$.

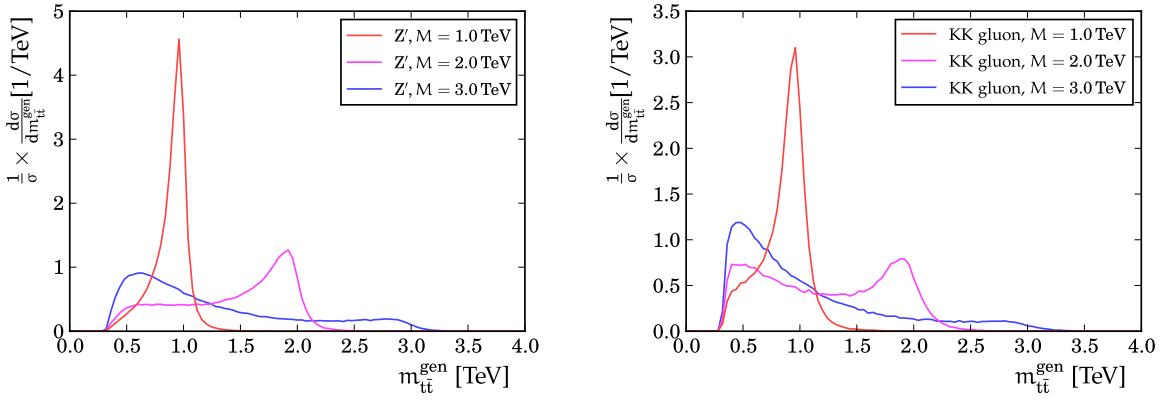

Figure 3.4: Distribution of the generated invariant $t\bar{t}$ mass $m_{t\bar{t}}^{gen}$ for the *wide* Z' signal (left) and the *KK-Gluon* sample (right).

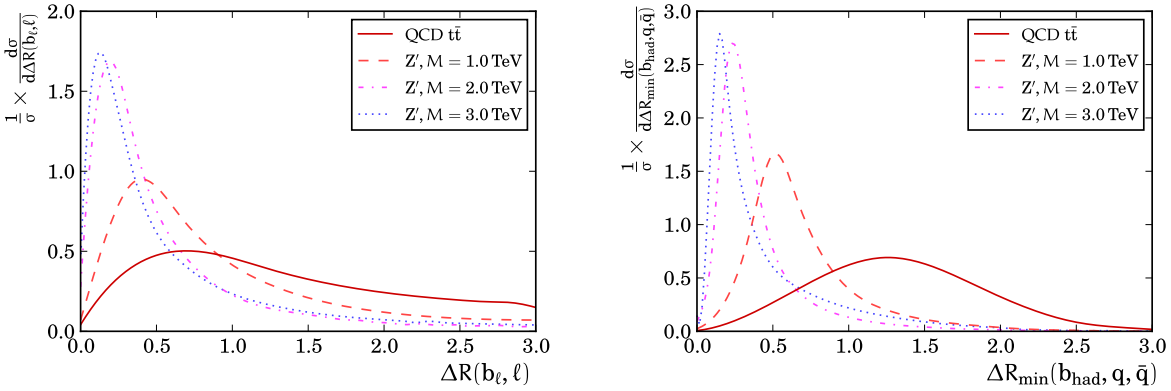

Figure 3.5: Distribution of the distance ΔR of the b quark and the lepton of the leptonically decaying top quark (left) and the minimum distance between any pair of the three quarks of the hadronically decaying top quark (right).

convolution of the natural width and the experimental resolution — is determined almost completely by the experimental resolution rather than the natural width. Therefore, the narrow Z' samples can be used to model all resonances for which the natural width is much smaller than the $M_{t\bar{t}}$ resolution, and it is used to set limits on the topcolor Z' model with $\Gamma = 0.012 \times M_{Z'}$. As the narrow Z' samples have a small range of generated invariant mass values $m_{t\bar{t}}^{gen}$, they are suitable for studying different properties that change as a function of $m_{t\bar{t}}^{gen}$ such as the $M_{t\bar{t}}$ resolution and the selection efficiency; the narrow Z' signal is therefore used as the default signal type in the next chapters.

For increasing values of $m_{t\bar{t}}^{gen}$, the top quarks have larger transverse momenta. As a result, the decay products of the top quarks have smaller angular separation in the detector reference frame. This can be seen in figure 3.5, where the left graph shows the distribution of the distance ΔR in the η–ϕ plane of the b quark of the leptonically decaying top quark b_ℓ and the lepton ℓ; the right graph shows the distribution of the minimum ΔR between any pair of the three quarks of the hadronically decaying top quark $b_{had}, q, \bar{q}$. The angular separation decreases with increasing $M_{Z'}$ and this has significant consequences for the resulting event signature regarding the jet multiplicity and the lepton isolation at high $M_{Z'}$, which has to be considered in the event selection discussed in chapter 4.

3.2 Event Reconstruction

This section outlines the pattern recognition algorithms applied to the low-level CMS detector signals in order to find high-level particle candidates such as muons, electrons, jets, and missing transverse energy, which are used to study the underlying interaction.

3.2.1 Charged Particle Tracking

The tracking algorithm combines hits originating from charged particles traversing the inner tracking system of CMS. The resulting track parameters provide estimates for the momentum of the charged particle at the point of the hard interaction, as well as the closest distance to this point, the impact parameter.

The track reconstruction algorithm [107] starts with the *local reconstruction*, which clusters the raw detector signals from the pixel detector and the silicon strip detector into *hits*. For each hit, the hit position and its uncertainty are estimated.

In the *seeding* step, two or three hits are combined into so-called pairs and triplets; some of the algorithms applied also make use of the beamspot position [108]. Each seed provides an initial estimate for the track parameters that are used in the *track building* step. In this step, the current track parameters are used to estimate the position and the uncertainty of the hit position in the next layer, going from the inside to the outside of the CMS tracker. This track propagation accounts for energy loss of the particle in the tracker layers. At the next layer, compatible hits are included and the track parameter estimates are updated. This procedure of propagating the current estimate and updating it with new information is performed with a Kalman filter [109]. If there is more than one compatible hit, multiple track candidates are created with different track parameters; the algorithm also allows for the absence of a compatible hit in one layer.

Ambiguities in the track finding can arise if a given track is found by more than one seed or if one seed gives rise to multiple tracks. Therefore, tracks with a low quality (few hits and large χ^2) that share more than half of the hits with a high-quality track are removed. Finally, the track parameters are re-estimated by a global fit to the track using all assigned hits. This final fit removes any potential bias introduced in the seeding stage.

This track finding algorithm is applied multiple times; at the end of each iteration, all hits used in the track reconstruction are removed and the new iteration is performed with looser requirements for the seeds and other parameters in the track building [110]. This iterative approach allows track finding with reasonable computing time at a high efficiency.

The reconstructed tracks are used to find primary vertices by first clustering tracks based on their z coordinate at the point of the closest approach to the beam-line. A track can be assigned to multiple clusters with weights based on the compatibility of the track with the z position of the cluster; this clustering step is performed with the deterministic annealing algorithm [111,112]. In a second step, the vertex positions and uncertainties are estimated from the track clusters.

Primary vertices originating from pileup interactions usually have few and low-p_T tracks. Therefore, the primary vertices are sorted by the decreasing sum of the associated squared track transverse momenta. The first primary vertex after sorting is used as the position of the primary interaction one wants to study, all other vertices are considered to correspond to pileup interactions.

3.2.2 Reconstruction of Muons

For the reconstruction of muons [113], two types of tracks are used: Tracks reconstructed in the inner tracker as described in the previous section and *standalone-muon tracks* reconstructed from hits in the muon systems by first searching for short track segments in each muon system (DT or CSC), which are then combined in a track fit. From these two types of tracks, muon candidates are reconstructed by two algorithms:

1. The *Global Muon reconstruction* propagates the track position from standalone-muon tracks and from tracks from the inner tracker to a common surface. If they are compatible, a *global track* is found by fitting a track to all hits used in either one of the tracks.

2. The *Tracker Muon reconstruction* starts with tracks reconstructed in the inner tracking system and extrapolates their position to the muon system, allowing for energy loss as the muon traverses the detector. In the muon system, a compatible track segment is sought.

In most cases a prompt muon, i.e. a muon originating directly from the hard interaction, is successfully reconstructed by both algorithms. Sources of non-prompt muon include muons from the decay of mesons containing c and b quarks, muons from cosmic rays, and *decay-in-flight* muons from decays $K/\pi \to \mu\nu$, where the track from the kaon is combined with the hits of the muon in the muon chamber.

In order to suppress the rate of non-prompt muons, additional identification requirements on the muon candidates are imposed. The used requirements are:

- The global track fit has to fulfill $\chi^2/\text{ndof} < 10$, where ndof is the number of degrees of freedom in the track fit. Also, a minimum number of hits in the inner tracker is imposed. These two requirements reject decay-in-flight muons.

- The z distance of the muon track extrapolated to the closest approach of the primary vertex has to be smaller than 1 cm and the transverse impact parameter has to be $\leqslant 200\,\mu m$. These requirements reduce cosmic muon background and muons form heavy flavor decays.
- The number of muon chambers with hits used for the track reconstruction has to be at least 2, to be compatible with the requirement of the muon trigger.

Using simulated events the muon trigger and identification efficiency can be estimated by searching for a reconstructed muon for each generated muon in a $t\bar{t}$ decay. This efficiency is found to be larger than 90% for all types of $t\bar{t}$ events used in the analysis presented in this thesis. The efficiency for the muon identification and trigger requirements can also be studied on data using the so-called *tag and probe* method in which a pure sample of $Z \to \mu^+\mu^-$ candidate events is selected by imposing tight requirements on the *tag* muon and subsequently applying the identification requirements on the *probe* muon, which yields estimates for the efficiency of these requirements. With this technique it was shown that the agreement for the muon efficiency between data and simulation is good; differences are below 5% for all regions of p_T and η [114]. While these measurements could be used to apply an event reweighting for simulated events based on the muon p_T and η as discussed in section 3.3, such a detailed correction is not required for this analysis. Therefore, no correction to the simulation has been applied and the maximal deviation of 5% is used as a systematic uncertainty for the muon efficiency.

3.2.3 Reconstruction of Electrons

Before reaching the electromagnetic calorimeter, electrons traverse the inner tracker can lose a considerable part of their energy by photon radiation at the tracker layers. These photons are emitted approximately in the current flight direction. This energy loss in the inner tracker is larger for electrons than for other charged particles and the energy in the electromagnetic calorimeter has a large spread in ϕ. This is considered in the electron reconstruction algorithm used at CMS [115, 116], which starts by searching for clusters in the electromagnetic calorimeter, considering their η-ϕ asymmetry. For these clusters compatible tracks in the inner tracker are searched. However, instead of using the track reconstruction algorithm discussed in section 3.2.1, a dedicated tracking algorithm is used that accounts for the increased energy loss caused by the photon emissions. Seeds are generated from hits in the pixel detector compatible with the ECAL cluster. To account for the increased energy loss at each tracker layer, the track building uses a Gaussian sum filter [117, 118] instead of the Kalman filter.

Additional requirements are imposed on electron candidates in order to reduce fake electrons, e.g. from pions. In the analysis discussed in this thesis, a cut-based electron identification is used [119]. The variables used include track–cluster compatibility variables, shower shape variables of the ECAL cluster, the amount of energy measured in the hadron calorimeter, and track parameters such as the transverse impact parameter.

3.2.4 The Particle Flow Algorithm

The simplest and historically first approach at CMS for the reconstruction of jets and missing transverse energy was based only on the energy deposits measured in the electromagnetic and hadron calorimeters. The energy resolution of these calorimeter-based algorithms is limited due to various effects. One of these limitations is that calorimeter-based algorithms assume that the direction of energy flow associated with a calorimeter tower is given by a straight line extending from the primary vertex towards the position of the measured energy deposit. This is not true for the trajectories of charged particles, which are bent in the magnetic field. Another limitation is that the calorimeter response depends on the particle type and is not perfectly linear in the energy of the particle.

The particle flow (PF) algorithm [120] overcomes some of these limitations by combining track information with calorimeter information, which allows a much better direction resolution and a better energy calibration. The particle flow algorithm provides a set of particles of five classes: muons, electrons, photons, charged hadrons, and neutral hadrons. The reconstruction of these particle candidates is based on tracks and calorimeter clusters that are *linked* using a linking algorithm resulting in *blocks*. Each of these blocks is classified into one of the five particle categories and an energy correction is applied for each particle candidate.

The clustering algorithm starts with single calorimeter cells above a given threshold as *seeds* and aggregates neighbor cells if their energy exceeds twice the cell's noise level. Each seed results in one cluster, and a given cell can belong to more than one cluster. In this case, the cell energy is partitioned among all clusters based on the cell–cluster distance.

The linking algorithm extrapolates tracks to the expected maximum of the energy deposit in the electromagnetic and hadron calorimeter. If the track is within the boundaries of a cluster, or only one calorimeter cell away from a cluster, the track is linked to the cluster. For electron reconstruction, bremsstrahlung is collected by constructing tangents to the track at tracker layers that are extrapolated to the ECAL. If clusters are found, they are linked to the track. ECAL and HCAL clusters are linked if the ECAL cluster position is within the HCAL cluster envelope. For the

muon reconstruction, tracks reconstructed in the inner tracker are matched to track segments reconstructed in the muon system and linked if the global track fit has an acceptable χ^2.

To convert these blocks into particle flow candidates of one of the five categories, first all muon and electron candidates and the corresponding tracks and clusters are removed. Each of the remaining blocks with a track is classified as charged hadron. Some care has to be taken to avoid double-counting as one cluster can be linked to more than one track and vice versa. The calorimeter energy expected for a charged pion with the momentum given by the track is subtracted from the cluster. Remaining clusters without a linked track are classified as photons, or — if there is significant contribution of HCAL energy — as neutral hadron. The calorimeter clusters associated to hadrons are calibrated for nonlinearities in the HCAL response.

3.2.5 Reconstruction of Jets

Jets are the collimated streams of particles originating from partons of the underlying hard interaction undergoing hadronization. In general, jet algorithms can be applied to any set of four-vector input objects such as the final state partons of the interaction, the stable particles after hadronization (*generator jet* or *GenJets*), or the particle flow candidates (*particle flow jets* or *PFJets*). The jet algorithms used to cluster these four-vectors to jets are introduced in the first section.

The jets clustered from different types of input objects contain energy contributions from different sources, e.g. energy from pileup events and effects due to the imperfect detector response are included in particle flow jets, but not in the corresponding particle jets. The comparisons between the observables from the experiment and the theoretical modeling are usually based on generator jets, as depicted in figure 3.6. This requires correcting the energy of particle flow jets to the level of generator jets. This is discussed in the second section.

Sequential Jet Clustering Algorithms

A sequential jet clustering algorithm iteratively operates on a set of four-momenta called *protojets*, which initially is the set of input objects. At each iteration, all possible distances between two protojets i and j, d_{ij}, are calculated, as well as all beam-protojet distances d_{iB}:

$$d_{ij} = \min(p_{T,i}^{2n}, p_{T,j}^{2n}) \frac{\Delta R_{ij}}{R} \tag{3.2}$$

$$d_{iB} = p_{T,i}^{2n}\,, \tag{3.3}$$

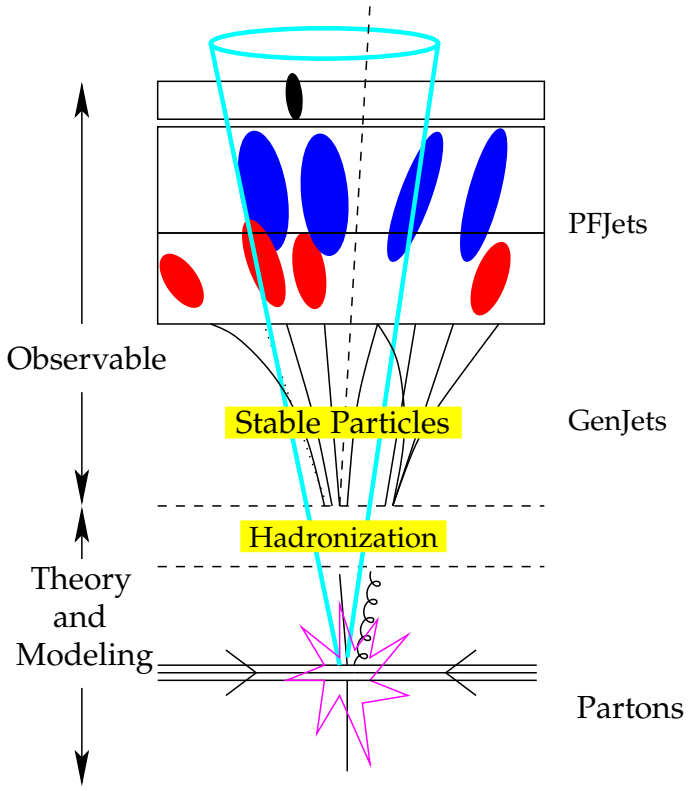

Figure 3.6: Illustration of the different steps of simulation and reconstruction, and the resulting jets (adapted from [121]). In this picture, the event modeling and simulation starts with the hard interaction at the bottom, whereas the jet reconstruction starts with particle flow jets at the top and corrects these to the level of generator jets, which defines the level at which theory and experimental observables are compared with each other.

where ΔR_{ij} is the distance of the protojets i and j in the y-ϕ plane; n and R are parameters of the algorithm discussed in more detail below.

If the smallest distance is a d_{ij}, the two protojets i and j are replaced by a protojet with the four-vector sum of i and j. If the smallest distance is a d_{iB}, the protojet i is a jet and it is removed from the list of protojets. This iteration is repeated until no protojets are left and all input objects are part of a jet.

The value of n specifies the type of the jet algorithm. For $n = 1$, the algorithm is called the k_T jet algorithm [122], $n = 0$ results in the Cambridge-Aachen algorithm [123], and $n = -1$ results in the anti-k_T algorithm [124]. All of these algorithms require the specification of the cutoff parameter R, which controls the size of the jets: All pairs of jets i, j satisfy $\Delta R_{ij} > R$.

The default choice at CMS for jet reconstruction is the anti-k_T algorithm with $R = 0.5$, which has the advantage of resulting in approximately cone-shaped jets. A straight-forward implementation of the sequential jet clustering algorithms requires a large number of distance evaluations, leading to a runtime rising at least quadratically in the number of input four-momenta N, which would make the algorithm unusable in practice at the LHC, where N is often on the order of one thousand. However, by not evaluating the distances d_{ij} in case it is known to be too large from geometrical arguments, the complexity can be reduced to $\mathcal{O}(N \log N)$, which was done in the FastJet package [125, 126] used at CMS.

One important property of jet algorithms in general is their stability with respect to higher-order corrections of perturbative QCD. In particular, the logarithmically divergent behavior for infinitely collinear and soft emissions arising in perturbative QCD must not change the result of the jet clustering; these requirements are known as *collinear safety* and *infrared safety*, respectively. All sequential clustering algorithms discussed here have these properties.

For the jet energy corrections discussed below, it is necessary to determine the area of a jet in the y-ϕ plane. As the jets can be irregularly shaped, this area cannot be calculated analytically. Instead, a large number of infinitely soft "ghost particles", which are evenly distributed in the y-ϕ plane, is added to the list of input objects of the jet clustering algorithm. The number of ghost particles is chosen such that the statistical uncertainty of the jet area due to the finite number of ghost particle is much smaller than other uncertainties. The configuration used at CMS is an average ghost area in the y-ϕ of 0.01, and the area determination is repeated five times with this setting. The jet algorithm is then applied on this new list and the jet area is given by the number of ghost particles clustered to this jet, divided by the number of ghost particles per y-ϕ unit area. This method was originally proposed in Reference [127]. Note that this method exploits both the infrared safety as well as the sub-quadratic runtime behavior of the clustering algorithm.

Jet Energy Corrections

The jets used in this analysis are anti-k_T jets using particle flow candidates as input objects. However, not all particle flow candidates found by the particle flow algorithm are used for jet clustering: All particle flow candidates that are identified as originating from pileup interactions, as well as isolated electrons and muons are removed from the original list. Particle flow candidates are considered as originating from pileup interactions if their track is associated to a primary vertex that is not the highest p_T primary vertex in the event. This method requires a track for the particle flow candidate and thus removes only the pileup contribution from charged particles within the tracker acceptance. Muons (electrons) are considered isolated if the p_T-sum of all particle flow candidates in a cone in the η-ϕ plane with a radius $\Delta R = 0.4$ is below 15% (20%) of the lepton's transverse momentum. These leptons are considered candidates for prompt leptons, and removing them from the jet clustering avoids double-counting of their energy in the analysis.

After jet clustering, the jet energies are corrected by applying a scale factor on the jet four-momenta such that the average jet energy response D is one, where

$$D(p_T^{gen}, \eta) = \left\langle \frac{p_T^{rec}}{p_T^{gen}} \right\rangle . \tag{3.4}$$

Here p_T^{gen} is the transverse momentum of the generator jet clustered from stable particles and p_T^{rec} is the corrected transverse momentum of the corresponding particle flow jet. To find this correspondence of generator jets and reconstructed jets is called *matching*. For jets, the used criterion is based on ΔR: The reconstructed jet and generator jet match if their distance in the η-ϕ plane fulfills $\Delta R < 0.3$.

equation (3.4) should hold for all values of η and p_T^{gen}. The jet energy corrections at CMS [128] are applied sequentially in different levels:

- The *level-1* or *offset correction* subtracts the energy shift due to pileup interactions and calorimeter noise.
- The *level-2* or *relative correction* is an η-dependent correction that makes the response $D(p_T^{gen}, \eta)$ flat in η.
- After applying the *level-3* or *absolute correction*, the response is flat in p_T^{gen}.

Technically, the corrections up to level-3 are derived for simulated events first, and the (small) difference to the actual response measured in recorded data is accounted for by applying an additional *residual correction* on recorded data only.

There are more correction levels, among them flavor-dependent corrections and corrections to the parton level instead of the generator jet level, but these are not

used in this analysis. The jet energy correction levels applied here are the level-1, level-2, and level-3 corrections and all jet energies in this thesis refer to the corrected energies up to level-3, unless mentioned otherwise. These three correction levels are discussed in more detail below. They are applied for both data and simulated events. As the corrections on simulation and data are very similar, the corrections derived from simulated events are applied in both cases, and the remaining difference after level-3 corrections between simulation and data is accounted for by applying a small *level-2,3-residual* correction on data only.

The remainder of this section briefly discusses the different jet energy correction levels. For more details, see reference [128].

The level-1 or offset correction removes the average pileup contribution. The component of transverse momentum for a jet due to pileup can be estimated by the area of the jet, multiplied with the pileup p_T density in the y-ϕ plane [129]. The jet area is determined using the ghost particle method described in the previous section. The p_T per unit area in y-ϕ due to pileup, ρ, is estimated for each event by taking the median of the values p_T^i/A_i where i runs over all jets clustered with the k_T algorithm with $R = 0.6$. The level-1 energy correction for jet j subtracts the energy $\rho' A_j$ where A_j is the area of the jet and ρ' is an estimate of the pileup energy density. It is based on ρ with corrections that account for the η dependence of the pileup density and the fact that a part of the pileup energy has already been removed by not using particle flow candidates identified as originating from pileup vertices. The contribution from the underlying event — which is contained in ρ' and thus was subtracted — is added back to the jet.

The level-2 or relative correction makes the response flat as a function of η. It is derived using the transverse momentum balance in dijet events: Events with one jet in the central region $|\eta| < 1.3$ are selected to derive the η-dependent correction for the other jet.

The level-3 or absolute correction is derived from the transverse momentum balance of γ+jet and Z+jet events (with $Z \to \mu^+\mu^-$ or $Z \to e^+e^-$), exploiting the precise momentum measurement for photons, electrons, and muons.

The analysis described in this thesis uses jets with $|\eta| < 2.4$ and $p_T > 50\,\text{GeV}$. Jets are required to pass identification requirements in order to suppress jets built from single noisy calorimeter cells.

The jet energy uncertainty after the correction depends on the jet p_T and η and is about $\delta_{jes} = 2$–3% for the kinematic range used in this analysis. Its impact on the analysis can be assessed by scaling the jet four-momenta in simulated events by a factor $1 \pm \delta_{jes}$, as discussed in more detail in section 6.1.

For a sample of jets at a fixed value of jet p_T^{gen}, the jet transverse momenta of the corresponding reconstructed, corrected jets, p_T^{rec}, follow a Gaussian distribution with

the same mean. The width of this distribution is the *jet transverse momentum resolution*. It can be measured by using the balance in the transverse plane in dijet events. These measurements suggest that the resolution in simulated events is smaller than in data by about 10% [128], which is taken into account by smearing the jet four-momenta in simulated events as discussed in section 3.3.1.

3.2.6 Identification of b Jets

The identification of b jets is an important tool to select events with b quarks in the final state in order to strongly suppress non-b background processes. Jets originating from a b quark contain a B meson after hadronization, which travels a distance in the order of millimeters in the detector before decaying via the weak interaction. The charged particles from this decay are reconstructed as tracks with a large impact parameter. In many cases, the tracks can be used to identify the position of the B meson decay as a *secondary vertex*.

The b-tagging algorithm used in this analysis is the *Combined Secondary Vertex* algorithm [130], which uses variables from the secondary vertex. These variables include the distance from and direction relative to the primary vertex and the invariant mass of the tracks associated to the secondary vertex. This information is combined with track parameters such as the impact parameters, yielding a single discriminator variable per jet, which takes large values for b jets and small values for other jets. Different working points are defined based on the average mistag rate for light flavor jets, i.e. the probability to wrongly classify a jet as b jet if it actually originates from a gluon or from u, d, or s quarks. The working point chosen in this analysis is the "tight" working point defined by the average mistag rate of 1‰. The average efficiency is around 50% and has been measured in $\mathrm{t\bar{t}}$ events [131] and by methods using other b-tagging criteria [130]. Differences of the b-tagging efficiency and mistag rate between simulated events and data are corrected for by reweighting the simulated events as discussed in section 3.3.

3.2.7 Reconstruction of Missing Transverse Energy

Some particles such as neutrinos (or certain hypothetical particles in theories beyond the Standard Model) escape the detector without leaving signals that could be used for a direct detection. However, such particles can be detected indirectly as they manifest as an imbalance in the total momentum of the final state: As the proton-proton initial state has a vanishing total momentum in the detector reference frame, this is also true for the total momentum of the final state. As the proton remnants leave the detector in the beam line, this principle can only be applied to the transverse

momentum. The missing transverse energy is the momentum vector in the x-y plane that restores the momentum balance and is thus given by

$$\vec{E}_T^{\text{miss}} = -\sum_{i=1}^{N} \vec{p}_{T,i} \ , \tag{3.5}$$

where i runs over all final state objects. As for jet algorithms, different types of input objects can be used, such as the stable particles in the simulation, energy deposits in the calorimeters, or particle flow candidates. In this analysis, the missing transverse energy is calculated from particle flow candidates.

The missing transverse energy can be taken as an estimate for the sum of the transverse momenta of all "invisible" particles in the final state of the interaction; in the muon+jets $t\bar{t}$ final state studied here, the only invisible particle is the muon-neutrino and $\vec{E}_T^{\text{miss}}$ thus directly provides an estimate for its transverse momentum. The magnitude of the vector $\vec{E}_T^{\text{miss}}$ is denoted with E_T^{miss}, which is a useful quantity to distinguish between processes with and without neutrinos in the final state.

The performance of the missing transverse energy reconstruction at CMS has been studied using Z+jet events (with $Z \to e^+e^-$ or $Z \to \mu^+\mu^-$), γ+jet events, and dijet events, in which the E_T^{miss} resolution and scale is dominated by detector effects as there are no neutrinos contributing to the missing transverse energy; the agreement between data and simulation is found to be good [132].

3.3 Simulation Corrections

While the simulation in general agrees well with the data, some aspects of the simulation are different than in data. In order to make meaningful comparisons between simulation and data, known differences between the simulation and data are taken into account by different techniques described in more detail in this section. Three quantities in which data–simulation differences appear are discussed here: Jet transverse momentum resolution, b-tagging rates, and the multiplicity of pileup events.

3.3.1 Jet Transverse Momentum Resolution

The jet transverse momentum resolution is defined as the width of the Gaussian core of the reconstructed jet p_T distribution for a fixed p_T^{gen}. This resolution is measured in data using dijet events [128], and it was found that the resolution in data is worse than in the simulation. One possibility to account for this difference would be to add additional Gaussian noise to the jet momenta in simulated events. This

procedure, however, does not allow to emulate values for the jet energy momentum resolution, which are smaller than simulated, but this is required to study systematic uncertainties. Therefore, in this analysis, a different method is used that also allows to change the jet momentum resolution in both directions [133].

The jet momentum resolution difference between data $\sigma(p_T^{gen})$ and simulation $\sigma_{sim}(p_T^{gen})$ is taken into account by scaling the difference of the reconstructed and corresponding generated transverse momentum by a factor $f = \sigma/\sigma_{sim}$. More formally, each corrected jet four-momentum p in simulated events is replaced by a scaled four-momentum p':

$$p' = p \cdot \alpha \,, \qquad \text{where} \tag{3.6}$$

$$\alpha = \frac{p_T^{gen} + f \cdot (p_T - p_T^{gen})}{p_T}. \tag{3.7}$$

In rare cases, the factor α can be smaller than zero in which case zero is used instead to avoid unphysical flips of the jet direction. As this method scales the difference of the reconstructed and generated transverse momentum, it re-uses many features already present in the simulation and e.g. keeps the non-Gaussian tails of the p_T distribution. Another advantage of this method is that it does not require the absolute value of the jet transverse momentum resolution at a given p_T^{gen}; also, there is no (pseudo-)randomness necessary, making results easier to reproduce.

This procedure is applied to all jets in simulated events with $p_T^{gen} > 15\,\text{GeV}$. It modifies the reconstructed transverse momentum in simulated events. It is assumed that the difference of the jet momentum resolution has its origin in a difference of the momentum resolution of particle-flow candidates. As the particle-flow candidates are used to reconstruct the missing transverse energy, this correction of the jet transverse momentum resolution has to be propagated to the missing transverse energy as well, changing the value of the missing transverse energy in simulated events to

$$\vec{E}_T^{miss\prime} = \vec{E}_T^{miss} + \sum_i (1 - \alpha_i)\vec{p}_{T,i}^{raw}, \tag{3.8}$$

where i runs over all jets for which the resolution correction is applied to, α_i is the scale factor defined in equation 3.7, and $\vec{p}_{T,i}^{raw}$ is the uncorrected transverse momentum of jet i, i.e. the sum of the four-momenta of the particle-flow candidates the jet consists of, without applying jet energy corrections.

The measurement of the jet transverse momentum resolution in data has limited precision. To take that into account, not only the "nominal" value of f is used, but also smaller and larger values, which cover the 1σ uncertainty of the resolution measurement from reference [128]. The values for f are summarized in table 3.2.

	scale factor f		
$\lvert\eta\rvert$ Range	nominal	up	down
< 0.5	1.05	1.11	0.99
0.5–1.1	1.06	1.12	1.00
1.1–1.7	1.10	1.16	1.04
1.7–2.3	1.13	1.23	1.03
> 2.3	1.29	1.49	1.09

Table 3.2: Values for the resolution scale factor f used to modify the jet momenta in simulated events. The "up" and "down" variation correspond to the 1σ interval of the resolution measurement [128, 133].

3.3.2 b-Tagging Rates

The b-tagging efficiency ϵ_b is defined as the probability that an actual b jet is tagged by the b-tagging algorithm; it is a function of the jet transverse momentum and pseudorapidity. On simulated events, this efficiency can be determined using generator information; it is the fraction of b jets that are tagged. For data, different methods are used as discussed in section 3.2.6. The difference of the b-tagging efficiency between data and simulation are expressed as a scale factor SF_b, with

$$SF_b = \frac{\epsilon_{b,data}}{\epsilon_{b,sim}}, \tag{3.9}$$

which in general depends on the jet η and p_T. Similarly, the scale factor SF_l is determined for the mistag rate for light jets ϵ_l, defined as the probability to tag a jet originating from u,d,s quarks or gluons. As jets from c quarks behave similarly to b jets, the scale factor SF_b is also used for correcting c jet tagging efficiencies.

The uncertainty on the efficiency measurements on data are propagated to SF_b and SF_l. The values and uncertainties for the scale factors for the Combined Secondary Vertex tagger at the tight working point are summarized in figure 3.7. The scale factors are determined as a function of the jet p_T. The scale factors are measured up to 670 GeV [130], and the scale factors and uncertainties used for jet $p_T > 670$ GeV correspond to the values at $p_T = 670$ GeV, with the uncertainty increased by a factor of two [134].

The scale factors SF_b and SF_l are used to correct the simulation by reweighting the simulated events. In general, the event weight w for such an efficiency correction is the ratio of the selection probability expected for data events, divided by the selection

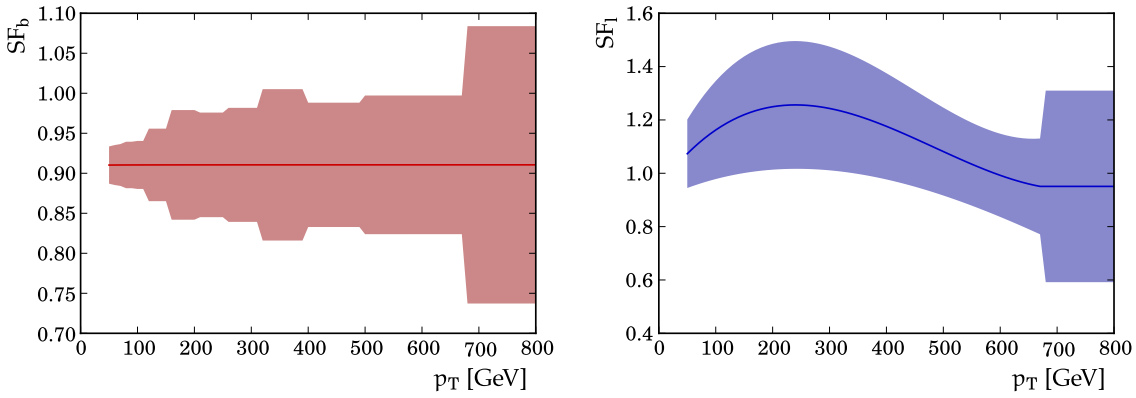

Figure 3.7: The data–simulation scale factors SF_b and SF_l for the b-tagging efficiency and mistag rate for the Combined Secondary Vertex tagger at the tight working point [130]. The bands indicate the 1σ uncertainty.

probability on simulated events,

$$w = \frac{p_{sel}^{data}}{p_{sel}^{sim}}. \tag{3.10}$$

The event selection probabilities are calculated for each event by considering all $2^{N_{jet}}$ possible combinations of which jets in the event are b tagged and which are not b tagged. The probability of a single combination c — in which the jets are numbered such that the jets $1, \ldots, k$ are b tagged and the jets $k+1, \ldots, N_{jet}$ are not b tagged — is given by

$$p_c = \prod_{i=1}^{k} \epsilon_{f_i} \prod_{i=k+1}^{N_{jet}} (1 - \epsilon_{f_i}), \tag{3.11}$$

where f_i denotes the jet flavor of jet i and is either "b" for a b jet or "l" for a light quark jet. The probability p_c can be calculated using either the tagging probabilities for data or for simulation, leading to $p_{c,data}$ and $p_{c,sim}$, respectively. The selection probabilities p_{sel} in equation (3.10) are then given by

$$p_{sel} = \sum_c p_c \tag{3.12}$$

where the sum runs over those combinations c for which the event would pass the event selection, i.e. using only combinations with a certain minimum and maximum number of b-tagged jets, according to the event selection the correction is applied for.

The systematic uncertainty on the b-tagging efficiency is considered by constructing two additional samples of simulated events in which the value used for SF_b in the

reweighting is shifted up or down by 1σ in the whole p_T range. Similarly, SF_l is varied by $\pm 1\sigma$ to derive different event weights.

3.3.3 Pileup Event Multiplicity

The distribution of the number of pileup events included in the simulation is different from the number of pileup events in data. This can be corrected for by reweighting simulated events.

For each simulated event, the number of pileup events to include is generated randomly in two steps:

1. A value λ for the mean number of pileup events per bunch crossing is drawn from a parent distribution p^{sim}_{pileup}.

2. The three numbers of pileup events (in-time; out-of-time before/after the current bunch crossing) are drawn independently from a Poisson distribution with mean λ.

While the pileup reweighting could also be based on the three numbers generated in the second step, the simpler choice of reweighting based on λ is pursued in this analysis. This requires the knowledge of the probability distributions p_{pileup} for simulation and data. For simulated events, the used value of λ is saved and the distribution p^{sim}_{pileup} is evaluated from all simulated events for a given sample. The distribution for data is estimated for a given luminosity section from the instantaneous luminosity and the total inelastic proton-proton cross section [135, 136]. The distributions p_{pileup} for the dataset used in this analysis and for the simulated W+jets sample are shown in figure 3.8. The fluctuations in the W+jets distribution are not of statistical origin, but rather an (unintentional) artifact of the seeding mechanism of the pseudo random number generators used to generate the number of pileup events.

The simulated events are reweighted such that the distribution of the Poisson mean λ of pileup events after reweighting, but before any event selection, reproduces the one for data. The weight for a simulated event with mean λ is thus given by

$$w_{pileup} = \frac{p^{data}_{pileup}(\lambda)}{p^{sim}_{pileup}(\lambda)}. \tag{3.13}$$

The uncertainty on the total inelastic cross section and other sources of uncertainties can be considered by using alternative distributions for p_{data}, constructed by varying the total inelastic cross section by $\pm 5\%$ [137] and re-deriving the event weights.

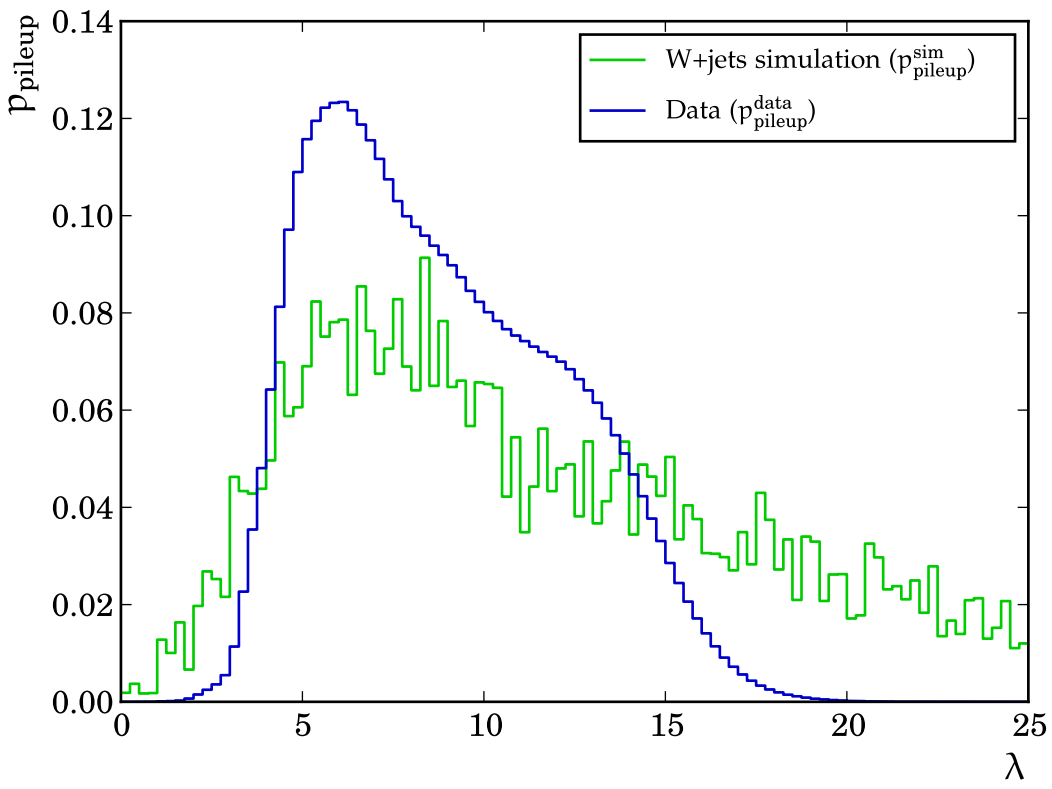

Figure 3.8: The distribution for the mean number of pileup events per bunch crossing λ for data and for the simulated W+jets sample.

3.4 Systematic Uncertainties

Systematic uncertainties for the simulation fall into two broad classes, theoretical uncertainties related to the event generation and uncertainties specific to the CMS detector, data taking, and reconstruction.

Theoretical uncertainties are considered by varying parameters used in the event simulation. Cross section uncertainties are considered for all standard model background processes. The uncertainties given in table 3.1 are the uncertainties on the corresponding higher-order result, while the simulation of most background processes — all except single top quark production — are based on tree-level Feynman graphs. This suggests to increase the uncertainties. Also, the statistical analysis can constrain the background rates in-situ anyway, and increased uncertainties on the background cross section do not have a large impact on the resulting sensitivity. The used uncertainties for the cross sections are 15% for the QCD $t\bar{t}$, 50% for the two single top quark production processes, and 100% for Z/γ^*+jets.

The W+jets background contains jets originating from heavy flavor quarks (c and b quarks) and from light flavor quarks and gluons. While the theoretical uncertainty from higher-order calculations on the inclusive W cross section is small, the fraction of W+heavy flavor has large uncertainties, e.g. differences of up to 50% are observed for the predicted W+b production rate between Pythia and MadGraph [138]. To account for this uncertainty, the W+jets events are split into two subsamples, a W+heavy flavor sample and a W+light flavor sample: If a simulated event contains at least one reconstructed jet originating from a heavy flavor quark, it is assigned to the W+heavy flavor sample; otherwise, it is assigned to the W+light flavor sample. The splitting allows to vary the contributions of both samples independently. A cross section uncertainty of 50% for the W+light flavor cross section is used and a value of 100% for the W+heavy flavor cross section.

Theoretical uncertainties also arise from the arbitrariness of some of the parameters used in the event generation discussed in section 1.3. The uncertainty due to the parton distribution functions typically changes the acceptance in the order of a few percent and is neglected in this analysis. The arbitrariness of the factorization/renormalization scale is considered by generating two samples in which both scales are simultaneously increased and decreased by a factor two. This has been done for the QCD $t\bar{t}$ and the W+jets sample. Another arbitrary parameter is the jet p_T threshold used in the MLM matching algorithm (see section 1.3), which is also varied up and down by a factor two for $t\bar{t}$ and W+jets. These samples are used to determine uncertainties on the rate and shape of distributions used in the statistical analysis as discussed in section 6.1.

The uncertainties specific to CMS are due to the uncertainties on the jet energy

correction discussed in section 3.2.5 and the simulation corrections introduced in section 3.3. They can be included by applying jet energy corrections or events weights to simulated events, in which the underlying correction is varied upwards or downwards by 1σ of their respective uncertainty. This generates two additional event samples per uncertainty, and the difference of these "up" and "down" variations with respect to the "nominal" sample is considered in the statistical analysis as discussed in detail in chapter 5 and section 6.1.

4 Event Selection and Reconstruction of the $t\bar{t}$ System

In order to make statistical statements about $t\bar{t}$ resonances, the employed method comprises: Selecting a pure sample of $t\bar{t}$ events by suppressing all non-$t\bar{t}$ backgrounds — in particular the QCD multijet background —, estimating the invariant $t\bar{t}$ mass $M_{t\bar{t}}$ for each of the remaining events, and comparing the simulated and observed $M_{t\bar{t}}$ distributions. The first two items are covered in this chapter; the last item is the topic of the next chapter.

Events undergo a common preprocessing and a first loose selection, the *preselection*, both discussed in section 4.1. The remaining events have a well-defined event content. This allows to apply the $t\bar{t}$ reconstruction algorithm discussed in section 4.2, which provides an estimate for the invariant $t\bar{t}$ mass, $M_{t\bar{t}}$. The suppression of the QCD multijet background is discussed in section 4.3. The chapter concludes with the final event selection presented in section 4.4.

4.1 Preprocessing and Preselection

This section outlines the processing and selection steps applied to the simulated and recorded events. The first section discusses preprocessing and filtering steps, while the second section describes the preselection requirements motivated by the event signature of $Z' \to t\bar{t}$ signal events.

4.1.1 Preprocessing and Filtering

The first step of the event selection is the high-level trigger discussed in section 2.2.5. For the selection of $t\bar{t}$ events in the muon+jets channel, high-level triggers are used that require the presence of one muon above a certain p_T threshold; in contrast to other analyses using prompt leptons, no isolation requirement on the muon is imposed. For simulated events, the requirement is $p_T > 30\,\text{GeV}$. For data, the trigger requirement depends on the run range as the trigger requirement changed to adapt to the increasing instantaneous luminosity during data taking. The most restrictive trigger, used for the latest runs, requires a muon with $p_T > 40\,\text{GeV}$ and $|\eta| < 2.1$. Which trigger is used for which run range is summarized in table 4.1. The muon p_T requirement $p_T > 42\,\text{GeV}$, which is part of the preselection discussed in section 4.1,

Run Range	Trigger	Integrated Luminosity (fb^{-1})
160431–163869	`HLT_Mu24`	0.22
165088–167913	`HLT_Mu30`	0.96
170826–173198	`HLT_Mu40`	0.83
173236–180252	`HLT_Mu40_eta2p1`	2.99

Table 4.1: Triggers used for the different run ranges, with the corresponding integrated luminosity. The number in the trigger name refers to the applied p_T cut, and `eta2p1` in the last row refers to the requirement $|\eta| < 2.1$. Gaps between the run ranges do not contain any certified runs.

is higher than the highest trigger p_T threshold. This ensures that all used triggers in data and simulation have the same efficiency within the assumed uncertainties.

Recorded events with anomalous noise in the hadron calorimeter are rejected, as well as so-called *beam-scraping* events with a large tracker occupancy leading to a high fraction of low-quality tracks. Also, the highest-p_T primary vertex is required to be consistent with proton-proton collisions and has to fulfill $|z| < 24\,\text{cm}$ and $\rho < 2\,\text{cm}$, where ρ is the distance from the center of the detector in the transverse plane. These conditions are designed to be effective against anomalous events only, rejecting much less than one permille of $t\bar{t}$ events.

Recorded events are only accepted if they belong to a run and luminosity section in which all detector components were found to be functional by a data certification procedure, as discussed in section 2.2.5.

As the muons are also particle-flow objects, they are clustered to particle-flow jets, unless the muon is isolated. In order to avoid double counting of the muon energy in the $t\bar{t}$ reconstruction, the non-isolated muon momentum is subtracted from the jet it has been clustered to.

The jet energy corrections discussed in section 3.2.5 and the jet energy resolution smearing described in section 3.3.1 are also applied at this stage.

4.1.2 Preselection

The preselection is a loose event selection with a high efficiency for $t\bar{t}$ events. It serves several purposes:

- It significantly reduces the amount of simulated and recorded events for further processing,

- it ensures that the trigger efficiency plateau for the muon trigger is reached,
- it removes any overlap with the e+jets selection from reference [139], required for a statistical combination, and
- it ensures that all events have a well-defined event content — a muon, and a minimum number of jets — for which a $t\bar{t}$ reconstruction algorithm can be developed, which is discussed in section 4.2.

As discussed in section 1.2.1, the final state of a $t\bar{t}$ event in the muon+jets channel comprises two b quarks from the top quark decays, two light quarks from the hadronic W decay and a muon and a neutrino via the leptonic W decay. The expected event signature for $t\bar{t}$ events therefore consists of four jets, two of which are b jets, one muon, and substantial E_T^{miss} due to the neutrino. For increasing generated invariant $t\bar{t}$ masses $m_{t\bar{t}}^{gen}$, the angular separation of the three quarks of the hadronically decaying top quark decreases, as discussed in section 3.1.2. As the distance of the quarks in ΔR becomes smaller, so does the distance of the corresponding reconstructed jets until, for high $m_{t\bar{t}}^{gen}$, fewer than three jets are reconstructed for a large fraction of events; this effect is referred to as *jet merging*. Therefore, the selection does not require four jets — as is commonly done to select QCD $t\bar{t}$ events, e.g. in reference [58] —, but only at least two jets in total, allowing for the three quarks of the hadronically decaying top quark to merge into a single jet. Similarly, the decay products of the leptonically decaying top quark have a small angular separation, and the small angle between the b quark and the muon leads to the muons not to be necessarily isolated. Therefore, no isolation requirement is imposed, neither at the trigger level nor later in the event selection.

Considering the desiderata and the event signature just discussed, the preselection requires

- at least one muon with $p_T > 42\,\text{GeV}$ and $|\eta| < 2.1$,
- at least two jets with $p_T > 50\,\text{GeV}$ and $|\eta| < 2.4$, and
- no electron with $p_T > 40\,\text{GeV}$ and $|\eta| < 2.5$.

Details about identification criteria applied for muons, electrons, and jets can be found in section 3.2.

4.2 Reconstruction of the $t\bar{t}$ System

The $t\bar{t}$ reconstruction provides an estimate for the four-momenta of the leptonically decaying top quark t_{lep} and the hadronically decaying top quark t_{had} for each event.

The reconstruction algorithm has to cope with the different expected jet multiplicities arising from the possible jet merging of the t_{had} decay products and it has to work for all events passing the preselection. The algorithm starts with the reconstructed objects: the four-momenta of the muon, the missing transverse energy, and the jets. It proceeds in three steps: Reconstruction of the neutrino, hypothesis list building, and hypothesis selection.

In a first step, the neutrino four-momentum is reconstructed by assuming that its transverse component is given by the missing transverse energy and that the neutrino and the muon originate from the decay of an on-shell W boson with an invariant mass m_W, as expected for $t\bar{t}$ events. This condition leads to a quadratic equation for the z component of the neutrino momentum, which has either zero, one, or two real solutions. The case that there is no real solution for $p_{z,\nu}$ arises if the reconstructed transverse W boson mass $M_{T,W}$, defined via

$$M_{T,W}^2 = E_W^2 - p_{x,W}^2 - p_{y,W}^2, \tag{4.1}$$

is larger than m_W. This happens mainly due to the limited resolution of the missing transverse energy. There are different strategies to estimate $p_{z,\nu}$ in this case [140], but the particular choice only has very little impact on the resulting $M_{t\bar{t}}$ resolution in the current analysis. Therefore, a simple approach is pursued, and the real part of the complex solution for $p_{z,\nu}$ is used. In case of two real solutions, both solutions are considered in the second step of the algorithm. The number of neutrino four-vector solutions is thus either one or two, denoted with $N_{\nu\text{-sol}}$.

The second step of the reconstruction algorithm consists of building a list of hypotheses. Each hypothesis picks one of the $N_{\nu\text{-sol}}$ neutrino solutions. Exactly one of the N_{jet} jets of the event is assigned to t_{lep}, and each of the $(N_{jet} - 1)$ remaining jets is either assigned to t_{had} or not considered for this hypothesis. The initial number of hypotheses is thus $N_{\nu\text{-sol}} \cdot N_{jet} \cdot 2^{N_{jet}-1}$, where N_{jet} is the total number of jets in the event. Hypotheses for which no jet is assigned to t_{had} are removed. For each hypothesis, the four-momentum for t_{lep} is given by the sum of the four-momenta of the muon, the neutrino, and the jet assigned to t_{lep}. The four-momentum for t_{had} is given by the sum of the four-momenta of all jets assigned to t_{had}.

The third and last step selects one hypothesis per event. In order to develop selection criteria, it is useful to study simulated $t\bar{t}$ events in the muon+jets channel for which the correct hypothesis is known. The notion of a *correct* hypothesis, however, is quite ambiguous and requires a more stringent definition. This is done by matching each of the four quarks of the $t\bar{t}$ final state to a jet, using $\Delta R < 0.3$ as matching criterion. Matching two (or three) quarks to the same jet is allowed to consider all possible cases of jet merging. The events in which this matching is successful are referred to as *matchable* events. If one or more jets from the $t\bar{t}$ decay are outside the

kinematic acceptance, the event is not matchable. The fraction of matchable events is 35% for a narrow Z' with $M_{Z'} = 2\,\text{TeV}$. For matchable events, there is a well-defined correct hypothesis, which is the hypothesis using the same assignment of jets to t_{had} and t_{lep} as found by the matching; in case there are two neutrino solutions, the hypothesis considered as the correct one is the one with smaller $|p_{z,\nu}^{hyp} - p_{z,\nu}^{true}|$. The properties of the correct hypothesis for matchable events are studied in order to find suitable hypothesis selection criteria.

There are various variables that could potentially be used for the hypothesis selection. One desired property of any hypothesis selection criterion is that it should work equally well for the different cases of jet merging (one, two, or three jets for t_{had}), and for a large range of invariant $t\bar{t}$ masses. This excludes using variables such as the distance ΔR between the decay products of t_{had} as this variable depends on both the jet multiplicity as well as on $m_{t\bar{t}}$. Two simple variables that have the desired property are the invariant top quark masses. For the correct hypothesis both $m_{t_{had}}$ and $m_{t_{lep}}$ are expected to be close to the top quark mass. Using these two variables, a single variable χ^2 is calculated for each hypothesis,

$$\chi^2 = \frac{(m_{t_{had}} - \bar{m}_{t_{had}})^2}{\sigma^2_{t_{had}}} + \frac{(m_{t_{lep}} - \bar{m}_{t_{lep}})^2}{\sigma^2_{t_{lep}}}. \tag{4.2}$$

The mean values $\bar{m}_{t_{had}}$, $\bar{m}_{t_{lep}}$ and standard deviations $\sigma_{t_{had}}$, $\sigma_{t_{lep}}$ entering this definition are the mean values and standard deviations obtained using a Gaussian fit to the core of the distributions of $m_{t_{had}}$ and $m_{t_{lep}}$ for the correct hypotheses in matchable events for a narrow Z' with $M_{Z'} = 2\,\text{TeV}$. The distributions for the top quark masses are shown in figure 4.1, which also shows that the dependence of those variables on $M_{Z'}$ is small. The mean values found for $\bar{m}_{t_{had}}$ and $\bar{m}_{t_{lep}}$ are 177 GeV and 173 GeV respectively; the values for the standard deviations $\sigma_{t_{had}}$ and $\sigma_{t_{lep}}$ are 17 GeV and 19 GeV respectively. The differences of the mean values and standard deviations for $m_{t_{had}}$ and $m_{t_{lep}}$ arise from the different resolutions of the input objects used to reconstruct these quantities and from the different reconstruction techniques applied for t_{had} and t_{lep}.

Note that the task of hypothesis selection can be seen as a statistical classification problem, separating the correct hypothesis from the wrong hypotheses. In such an approach, practical solutions can be obtained by applying multivariate classifiers. For this analysis, however, the adopted standpoint is that hypothesis selection is merely a heuristic method without this statistical background. In particular, this means that using the χ^2 variable does not imply that there is an assumption that the variables $m_{t_{lep}}$ and $m_{t_{had}}$ entering the χ^2 definition above actually follow a normal distribution.

For each event, the hypothesis with the smallest value for χ^2, χ^2_{min}, is selected and this hypothesis is used to estimate the invariant mass of the $t\bar{t}$ system $M_{t\bar{t}}$. Figure 4.2

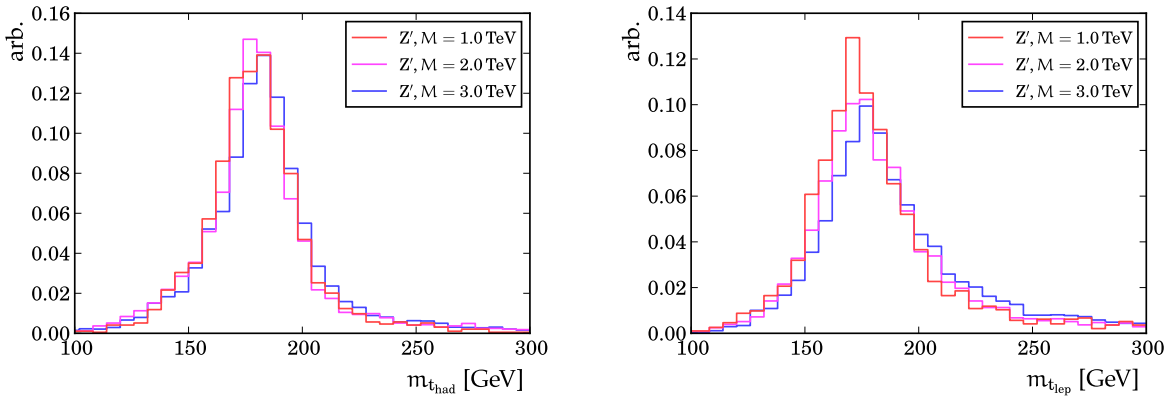

Figure 4.1: The invariant top quark masses $m_{t_{had}}$ and $m_{t_{lep}}$ for the correct hypothesis in matchable events for a narrow Z′ for different values of $M_{Z'}$.

shows the shape of the reconstructed $M_{t\bar{t}}$ for a narrow Z′ for different values of $M_{Z'}$. The tail towards lower $M_{t\bar{t}}$ values is due to various sources: A part of the tail is already present on generator-level $m_{t\bar{t}}^{gen}$ as shown in figure 3.3. Another contribution arises from $t\bar{t}$ dilepton events passing the event selection. For these events, the value for $M_{t\bar{t}}$ is systematically too low as the hypothesis is constructed assuming that E_T^{miss} is only due to one neutrino, not two. Finally, $t\bar{t}$ μ+jets events contribute to the tail if one or more of the $t\bar{t}$ decay products are outside the kinematic acceptance, which also leads to a $M_{t\bar{t}}$ value that is too low.

A valuable by-product of the hypothesis selection criterion is the value of χ^2_{min} for each event, which can be used as a compatibility measure for $t\bar{t}$ events: Correctly reconstructed $t\bar{t}$ events are expected to have a small value for χ^2_{min}, while events from background processes or incorrectly reconstructed $t\bar{t}$ events are expected to have large χ^2_{min} values. This is used in the event selection discussed in the next section.

The resolution of the $M_{t\bar{t}}$ reconstruction is defined as the width of the Gaussian core of the $M_{t\bar{t}}$ distribution for a fixed value of $m_{t\bar{t}}^{gen}$. The relative resolution is determined on simulated μ+jets events by iteratively fitting a Gaussian distribution to the distribution of $(M_{t\bar{t}} - m_{t\bar{t}}^{gen})/m_{t\bar{t}}^{gen}$, adapting the fit range after each iteration to the $\pm 2\sigma$ peak region, where σ is the Gaussian width determined by the previous fit iteration. In general, the resolution depends on the event selection, especially if it has a higher efficiency for correctly reconstructed $t\bar{t}$ events, which is the case for the final event selection as it applies a χ^2_{min} requirement. For events passing the final event selection, the relative resolution of $M_{t\bar{t}}$ is about 10% for $m_{t\bar{t}}^{gen} = 1\,\text{TeV}$ and improves (decreases) for larger $m_{t\bar{t}}^{gen}$, reaching a value of just below 6% for $m_{t\bar{t}}^{gen} = 3\,\text{TeV}$.

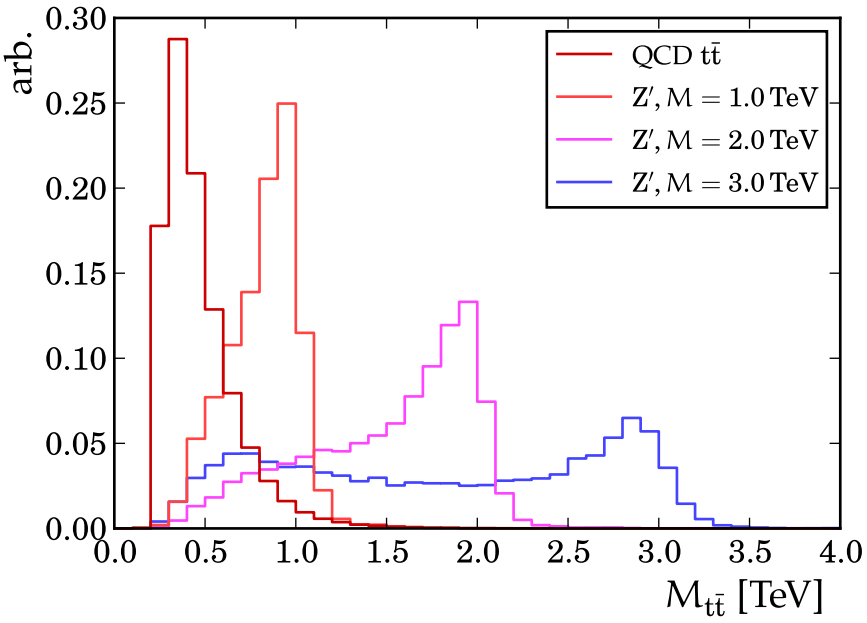

Figure 4.2: The reconstructed invariant $t\bar{t}$ mass $M_{t\bar{t}}$ for standard model $t\bar{t}$ production and narrow Z' samples.

4.2.1 $M_{t\bar{t}}$ Interpolation

The statistical inference is based on the $M_{t\bar{t}}$ distributions for Z′ and background processes. As discussed in section 3.1.2, the simulated Z′ samples have been generated with the masses $M_{Z'} = 1, 1.25, 1.5, 2$, and 3 TeV. In order to make statistical statements for other values of $M_{Z'}$, $M_{t\bar{t}}$ distributions for intermediate values of $M_{Z'}$ are required. These are obtained via the `RooMomentMorph` interpolation algorithm [141], which uses the templates for two $M_{Z'}$ masses to obtain the $M_{t\bar{t}}$ distribution at an intermediate mass value. An affine transformation (scale and shift) on the $M_{t\bar{t}}$-axis for each input distribution is applied to obtain distributions with the same mean and standard deviation. The interpolated template is then given by the weighted average of the two input distributions at each transformed $M_{t\bar{t}}$ value, and the affine transformation is undone, using a weighted average of the shift and scale factors used in the transformation of the input templates. Figure 4.3 shows an example for the output of the algorithm: The $M_{t\bar{t}}$ distributions for $M_{Z'} = 1$ TeV and $M_{Z'} = 1.5$ TeV are used to obtain an $M_{t\bar{t}}$ distribution for $M_{Z'} = 1.25$ TeV. This distribution is in reasonable agreement with the one obtained by using a simulated sample with $M_{Z'} = 1.25$ TeV.

4.3 QCD Multijet Suppression

After the preselection, the largest contribution is from QCD multijet production. As the QCD multijet production is harder to model from simulation than the other background processes, it is especially important to suppress this background.

The muons in QCD multijet production mainly originate from two sources: Decay-in-flight muons from the decay $K/\pi \to \mu + X$ and from heavy quark decays in $b\bar{b}$ and $c\bar{c}$ events. In all of these cases, the muon is created in association with hadrons or within a jet and thus particles close in ΔR are expected around the muon direction. A widely used approach to suppress QCD multijet production for the selection of prompt muons from W/Z+jets and $t\bar{t}$ events is therefore to require that the muon is isolated. A muon is considered isolated if the p_T-sum of all particle flow candidates in a cone in the η-ϕ plane with a radius $R = 0.4$ is below 15% of the muon transverse momentum. As mentioned in section 4.1, however, the small angles between the muon and the b quark from the leptonic top quark decay can lead to prompt muons in the signal not passing this isolation criterion. Therefore, an alternative criterion is applied here. It is based on the observation that muons in QCD multijet events are usually accompanied by a jet, which is close in ΔR and uses variables based on the muon and the nearest jet in ΔR, where in this case, a lower p_T requirement than usual is used for the jet definition, $p_T > 25$ GeV. For QCD multijet events, this jet is often the heavy flavor jet from which the muons originate. This jet is used to define the

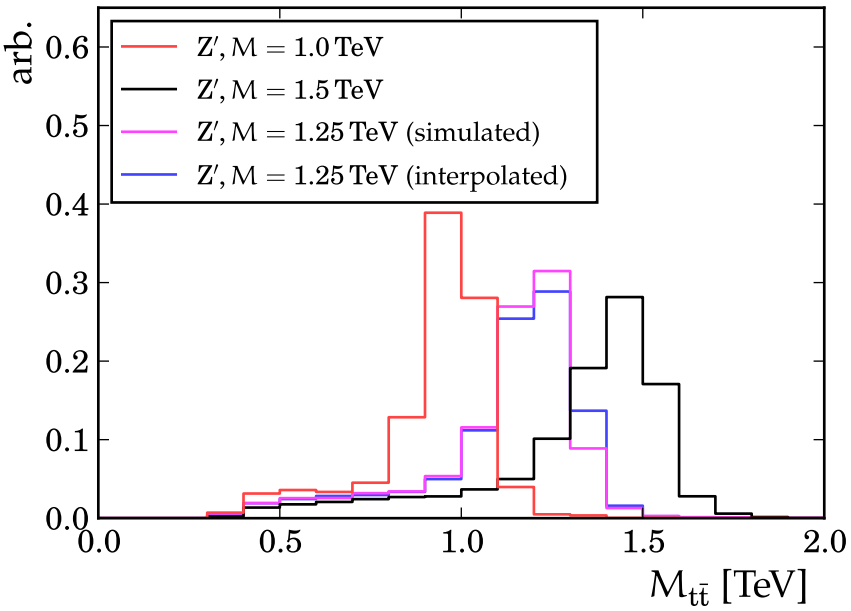

Figure 4.3: Example for the template interpolation: $M_{Z'} = 1\,\text{TeV}$ and $M_{Z'} = 1.5\,\text{TeV}$ distributions are used to obtain the interpolated distribution for $M_{Z'} = 1.25\,\text{TeV}$, which is compared to the distribution obtained directly from simulation.

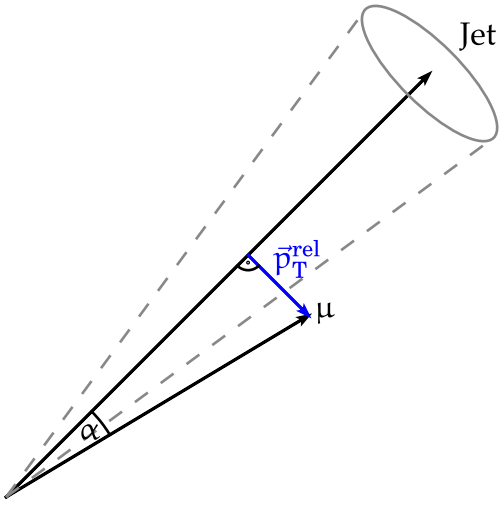

Figure 4.4: Illustration of the definition of the relative transverse momentum p_T^{rel}: It is defined as the length of the vector $\vec{p}_T^{rel}$, which is the component of the muon momentum perpendicular to the jet axis.

variable p_T^{rel}, which is the component of the momentum of the muon perpendicular to the jet axis. This is illustrated in figure 4.4 and can be expressed as

$$p_T^{rel} = p_\mu \sin \alpha \,, \tag{4.3}$$

where α is the angle between the jet and the muon momentum and p_μ is the magnitude of the three-momentum of the muon. This variable is used for b tagging algorithms [130] as it typically takes larger values for muons from semileptonic B meson decays in b jets than for muons originating from light quark jets. It takes even larger values for high-mass $t\bar{t}$ events and thus a requirement of a large p_T^{rel} can be used to keep muons in $t\bar{t}$ events while suppressing both decay-in-flight muons and muons from heavy flavor decays.

Muons in this analysis are selected based on two variables; the selection is referred to as the muon *2D-cut*. A muon passes this cut if it either has $\Delta R > 0.5$ or $p_T^{rel} > 25\,\text{GeV}$, both defined w.r.t. the nearest jet in ΔR, where any jet with $p_T > 25\,\text{GeV}$ is considered. To compare this cut with the isolation requirement, figure 4.5 shows the selection efficiencies of these two selections as a function of the Z' mass. For this comparison, the selection efficiency is calculated for a selection that also requires at least two jets with $p_T > 50\,\text{GeV}$; this jet requirement is the reason for the selection

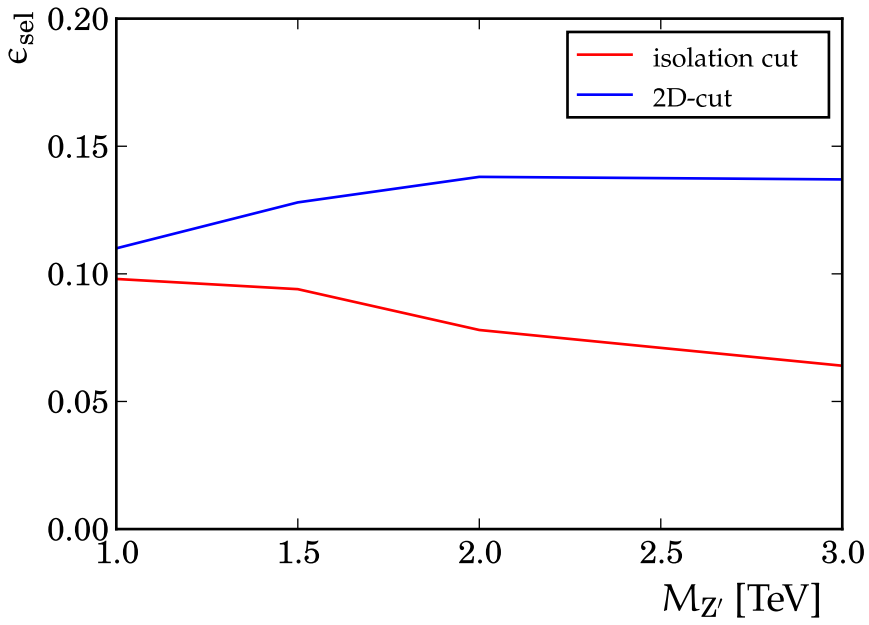

Figure 4.5: The signal event selection efficiency ϵ_{sel} for requiring the muon to be isolated or to fulfill the 2D-cut for a narrow Z′ as a function of $M_{Z'}$.

efficiency for the muon 2D-cut to increase as a function of $M_{Z'}$ for small $M_{Z'}$. The efficiency for the isolation requirement decreases with increasing $M_{Z'}$, while the 2D-cut efficiency is approximately constant. At high masses, the 2D-cut is two times more efficient than the isolation requirement. Therefore, the 2D-cut is used in this analysis to reduce QCD multijet background.

After applying the muon 2D-cut, still a large fraction of QCD multijet events remains. This fraction is further reduced by requiring $H_T^{lep} > 150\,\text{GeV}$, where H_T^{lep} is the scalar sum of the missing transverse energy and the muon transverse momentum. This requirement has a high efficiency for $t\bar{t}$ signal events in which a high-p_T muon and a high-p_T neutrino lead to a large value for H_T^{lep}, while both E_T^{miss} and p_T^{μ} are typically small for QCD multijet events, as is shown in section 4.4 in more detail.

The muon 2D-cut and the H_T^{lep} requirements do not only suppress the QCD multijet background, but also allow to construct sidebands to estimate the number of remaining QCD multijet events after the selection: Sidebands enriched in QCD multijet events can be defined by inverting the muon 2D-cut. From events in these sidebands, a shape for the QCD multijet distribution for H_T^{lep} is extracted and by fitting the H_T^{lep} distribution in the region $H_T^{lep} < 150\,\text{GeV}$, the number of QCD multijet

events with $H_T^{lep} > 150\,\text{GeV}$ can be estimated [27,28]. As the number of QCD multijet events is very small and negligible compared to the rate uncertainties due to the other background processes — the fraction of QCD multijet events is around 2% —, the QCD multijet background is not considered in the statistical analysis. The simulated sample for the QCD multijet background is still used, however, in the development of the final event selection.

4.4 Final Event Selection

The goal of the final event selection is to suppress the background processes while keeping a high signal efficiency in order to allow stringent statements about the cross section of resonances decaying to $t\bar{t}$. This suggests to develop an event selection that minimizes the expected limit. As the calculation of the expected limit including all uncertainties is hardly feasible, simpler quantities are used for the optimization, such as the ratio of the number of signal and background events S/B or the expected significance in the Gaussian approximation $S/\sqrt{B}$. Possible selection criteria have been studied in reference [27], using $S/\sqrt{B}$ in windows of $M_{t\bar{t}}$ as the optimality criterion. These studies suggest that the sensitivity can be increased by requiring a minimum transverse momentum for the leading jet (the highest-p_T jet), but no sensitivity is gained by requiring a minimum transverse momentum for the second jet or for the muon. A requirement for the leading jet of $p_T > 250\,\text{GeV}$ is used in this analysis.

The three requirements discussed so far — the muon 2D-cut and H_T^{lep} requirement to suppress the QCD multijet background and the cut on the leading jet p_T — are a suitable event selection and have been used as the final event selection in reference [28]. The expected limit can be further improved (reduced), however, by about a factor 2–3 if two additional steps are performed. The first step is a further selection step requiring $\chi^2_{min} < 8$. This suppresses the non-$t\bar{t}$ background and $t\bar{t}$ events with an unusually high χ^2_{min}, e.g. in dilepton events or in events in which one or more decay products of the $t\bar{t}$ events are outside the kinematic acceptance. To find the optimal threshold for this cut, the quantities S/B and $S/\sqrt{B}$ have been studied. Both quantities exhibit only a small dependence on the cut threshold, but suggest to use a small χ^2_{min} threshold that rejects a large fraction of the W+jets background, which is the main non-$t\bar{t}$ background. A very small threshold, however, would reduce the number of simulated events to a level that does not allow a reliable modeling of these backgrounds from simulation. The chosen threshold of 8 keeps around 50% of the signal and rejects about 96% of the W+jets background. The second step is to split the events into two disjoint channels, based on the number of b tagged jets

$N_{\text{b-tag}}$; the channels require $N_{\text{b-tag}} = 0$ and $N_{\text{b-tag}} \geqslant 1$, respectively. The background composition in these channels is different: The QCD $t\bar{t}$ process dominates the background in the $N_{\text{b-tag}} \geqslant 1$ channel, while the channel $N_{\text{b-tag}} = 0$ also contains a large fraction of W+jets events, which is affected by much larger uncertainties. Therefore, the background in the $N_{\text{b-tag}} \geqslant 1$ channel is better known and this increases the sensitivity.

In summary, the event selection criteria applied after the preselection are:

1. muon 2D-cut
2. leading jet $p_T > 250\,\text{GeV}$
3. $H_T^{\text{lep}} > 150\,\text{GeV}$
4. $\chi^2_{\text{min}} < 8$
5. either $N_{\text{b-tag}} = 0$ or $N_{\text{b-tag}} \geqslant 1$, using the CSV b tagging algorithm at the tight working point.

The selection efficiencies of the leading jet p_T requirement, of the H_T^{lep} requirement, and of the χ^2_{min} requirement for the main background processes and for Z′ signal are shown in figures 4.6 to 4.8, as functions of the applied thresholds.

The expected numbers of events for different processes, as well as the numbers of signal events and data, are summarized in table 4.2. The simulated samples are weighted according to the integrated luminosity using the corresponding cross sections, as discussed in section 3.1.1. The signal cross section is set to the arbitrary value of 1 pb. The corrections for the simulation discussed in section 3.3 have been applied. Between 20 and 30% fewer events are observed in data than expected for background only from the simulation. Considering the uncertainties on the backgrounds discussed in section 3.4, however, the observed number of events is compatible with the expected number of events. The events used in the statistical evaluation are those in the $N_{\text{b-tag}} = 0$ and $N_{\text{b-tag}} \geqslant 1$ channels, i.e. those in the last two columns in table 4.2.

One factor limiting the sensitivity of the analysis is the signal selection efficiency. It rises from 1.5% for $M_{Z'} = 1\,\text{TeV}$ — where the leading jet p_T requirement has a rather low efficiency — to 4.8% for $M_{Z'} = 2\,\text{TeV}$, and slightly decreases to 4.5% for $M_{Z'} = 3\,\text{TeV}$, where the decrease can be understood with the tail towards low $M_{t\bar{t}}$ values discussed above. This leads to a slight decrease in sensitivity for $M_{Z'} = 3\,\text{TeV}$, as will be discussed in more detail in chapter 6. Another cause for the loss of sensitivity is the b tagging efficiency: The fraction of the selected signal events in the channel $N_{\text{b-tag}} = 0$ rises for increasing $M_{Z'}$, as the b tagging efficiency decreases with

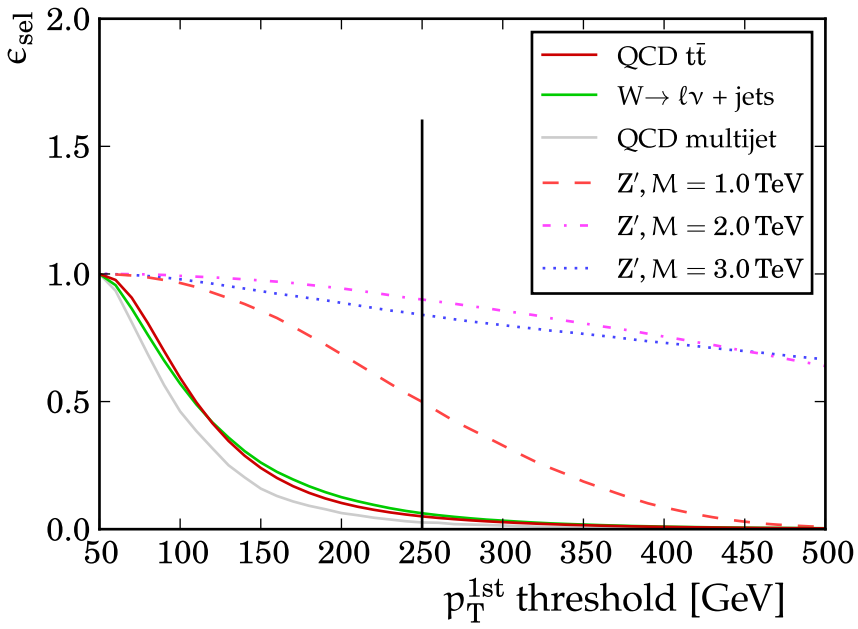

Figure 4.6: The selection efficiency ϵ_{sel} as a function of the leading jet p_T threshold, after applying the muon 2D-cut. This selection step reduces all background processes. The chosen threshold of 250 GeV is indicated with the vertical line.

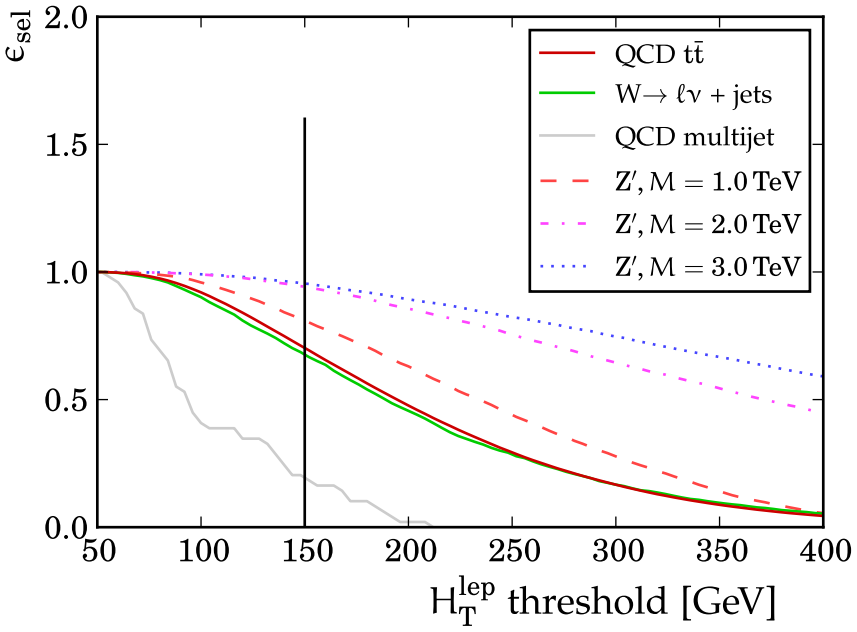

Figure 4.7: The selection efficiency ϵ_{sel} as a function of the H_T^{lep} threshold, after applying the leading jet p_T requirement. This requirement mainly reduces the QCD multijet background. As the simulated QCD multijet background sample contains only few events, the curve for this process exhibits statistical fluctuations. The chosen threshold of 150 GeV is indicated with the vertical line.

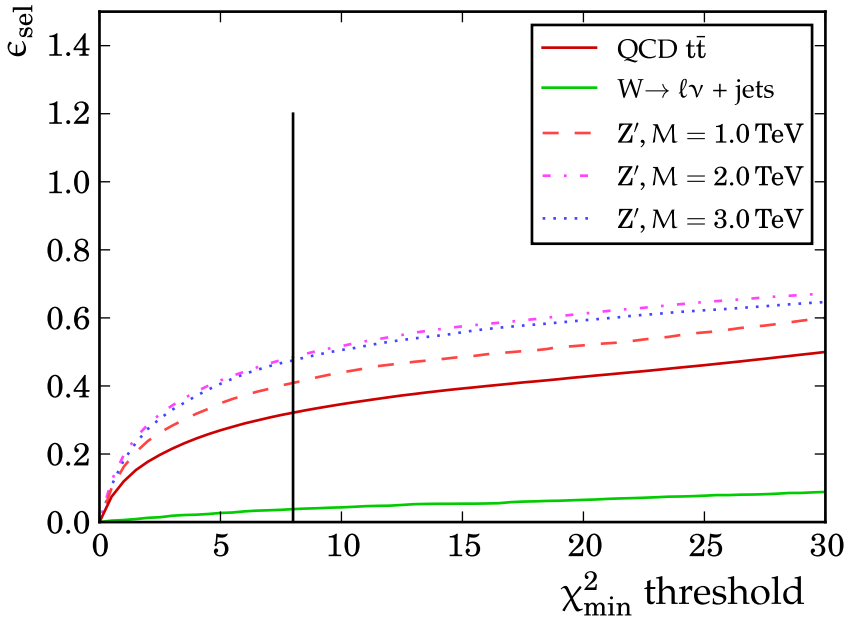

Figure 4.8: The selection efficiency ϵ_{sel} as a function of the χ^2_{min} threshold, after applying the H_T^{lep} requirement. This reduces all non-$t\bar{t}$ background processes. The chosen threshold of 8 is indicated with the vertical line. No simulated QCD multijet is shown due to the very low number of simulated events passing the selection.

increasing jet p_T. As the $N_{b\text{-tag}} = 0$ channel contains a considerable amount of the W+jets background affected by larger uncertainties, this leads to a loss of sensitivity as well.

	muon 2D-cut	leading jet p_T	H_T^{lep}	χ^2_{min} cut & $N_{b\text{-tag}} = 0$	χ^2_{min} cut & $N_{b\text{-tag}} \geqslant 1$
QCD $t\bar{t}$	45290	2274	1597	191	319
Single-Top	5905	303	212	9	12
$W \to \ell\nu$+heavy flavor	30802	1813	1196	42	6
$W \to \ell\nu$+light flavor	107471	6813	4631	172	2
Z/γ^*+jets	33193	1665	909	27	2
Total Background	—	—	8545	439	341
Z', $M = 1$ TeV	463	231	187	28	48
Z', $M = 1.5$ TeV	549	448	407	96	94
Z', $M = 2$ TeV	583	524	494	146	94
Z', $M = 3$ TeV	583	490	468	155	69
Data	245711	11553	7115	300	269

Table 4.2: Number of expected and observed events after the different steps of the event selection for $L = 5.0\,fb^{-1}$. The sum of the background processes is given only after QCD multijet background has been reduced to a negligible amount, i.e. after the H_T^{lep} requirement. The values given for Z' are for a narrow Z' with a cross section of 1 pb.

4.4.1 Modeling Checks

The statistical analysis relies on the simulation to model the properties of the data events within the assumed uncertainties. As a cross-check, distributions of various variables are compared between data and simulation in a sideband of the final event selection to find signs for possible sources of mismodeling. The chosen sideband is defined by inverting the leading jet p_T requirement and by not applying the χ^2_{min} and $N_{\text{b-tag}}$ requirements. This particular sideband was chosen as it is close to the final selection but does not contain a considerable fraction of QCD multijet events. The distributions checked fall into two broad classes: Distributions related to the reconstruction of the $t\bar{t}$ system and variables related to the reconstructed objects such as transverse momenta, pseudorapidities, multiplicities, and distances of jets, the muon, and missing transverse energy.

Figure 4.9 shows some variables of the latter class: The p_T and η of the muon, the number of jets N_{jet}, and the missing transverse energy E_T^{miss}. Figure 4.10 shows variables related to the $t\bar{t}$ event reconstruction: The distributions for the reconstructed top quark masses $m_{t_{\text{had}}}$ and $m_{t_{\text{lep}}}$ for the hypothesis with the smallest χ^2, the distribution of χ^2_{min}, and the $M_{t\bar{t}}$ distribution. The events with low $m_{t_{\text{had}}}$ are due to events with only two jets in which the hypothesis with the smallest χ^2 is a hypothesis with only one jet assigned to t_{had}, $m_{t_{\text{had}}}$ being the invariant mass of this jet. In both figures, the simulated events have been weighted according to the integrated luminosity and cross section. About 3% less data is observed than expected from the sum of the background processes. Various distributions have been checked and no signs of mismodeling have been found.

4.4.2 Selected Events

The statistical analysis is based on the simulated and observed distributions for $M_{t\bar{t}}$ in the channels $N_{\text{b-tag}} = 0$ and $N_{\text{b-tag}} \geqslant 1$. These are shown in figure 4.11. The simulated samples have been scaled to match the number of events observed in data. From these distributions, there is no visual indication for a resonant $t\bar{t}$ contribution; this conclusion is supported by the quantitative statistical analysis discussed in chapters 5 and 6.

Figure 4.12 shows a transverse view of the CMS detector with the selected event that has the highest value for $M_{t\bar{t}}$. It is an event in the $N_{\text{b-tag}} \geqslant 1$ channel and has many of the features expected for a high-mass $t\bar{t}$ event: It has only two jets in total — one b jet from the t_{lep} and one merged jet from t_{had} — and a non-isolated, high-p_T muon. Both reconstructed top quark candidates have an invariant mass close to the expected mass — the χ^2_{min} value is 1.1, much below the required value of 8. They

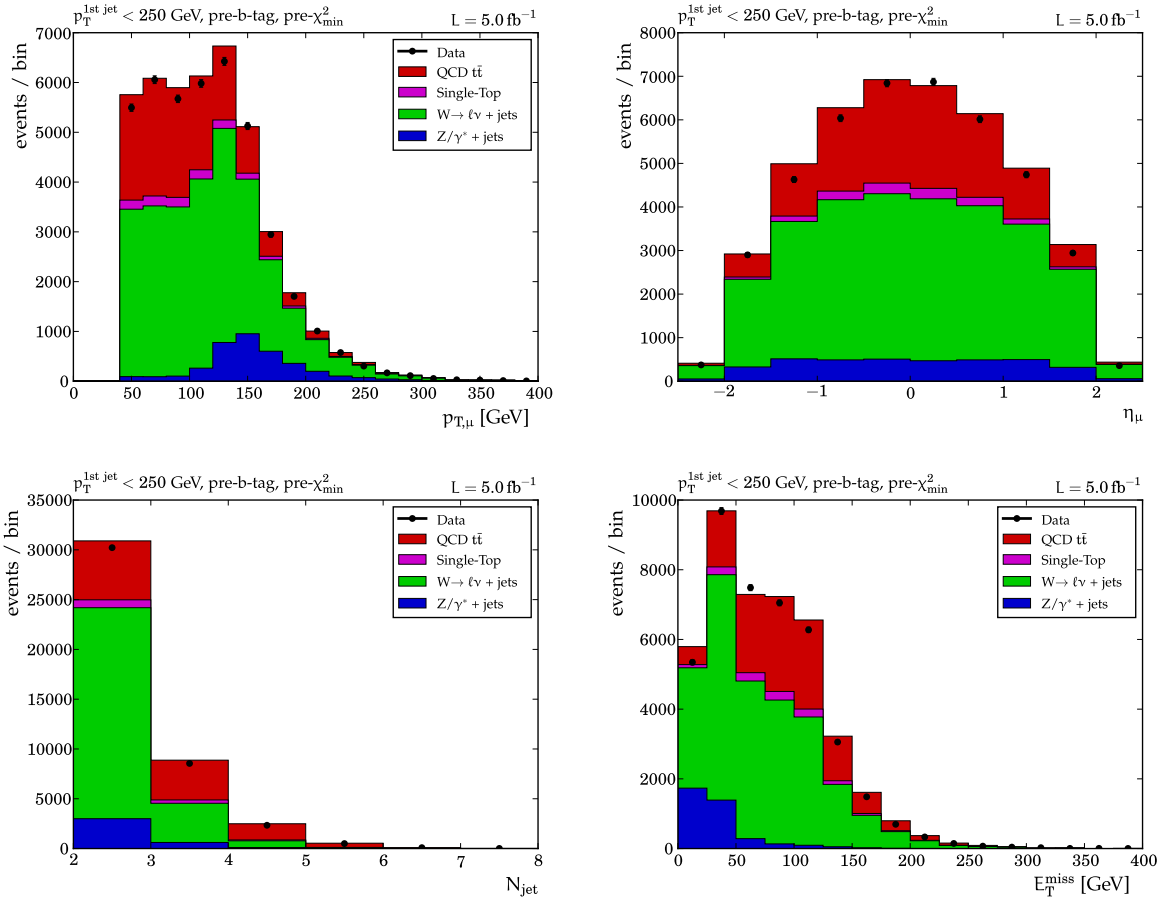

Figure 4.9: Distributions of the p_T and η of the muon, the number of jets N_{jets} and E_T^{miss} in the cross-check sideband with inverted leading jet p_T requirement and without χ^2_{min} and $N_{b\text{-}tag}$ requirements. Simulated events are weighted according to the luminosity and cross section.

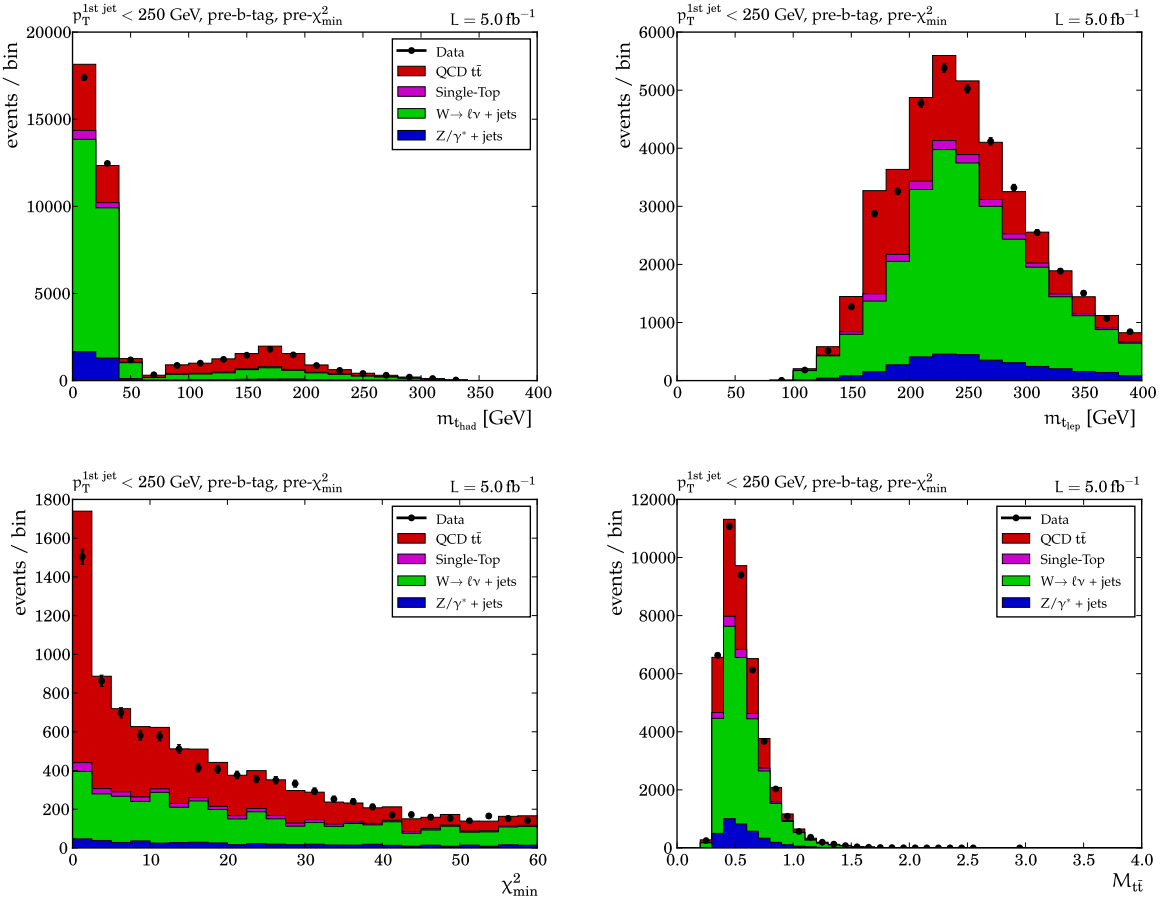

Figure 4.10: Distributions for variables connected to the $t\bar{t}$ reconstruction in the sideband: The reconstructed invariant masses for the top quarks for the selected hypothesis, χ^2_{min}, and the reconstructed $t\bar{t}$ mass $M_{t\bar{t}}$. Simulated events are weighted according to the luminosity and cross section.

are balanced in the transverse plane, one jet fulfills the tight CSV b tag, the other would pass the loose CSV b tag working point. Based on the purity of the $N_{\text{b-tag}} \geqslant 1$ channel, the probability that this is indeed a $t\bar{t}$ event is larger than 90%.

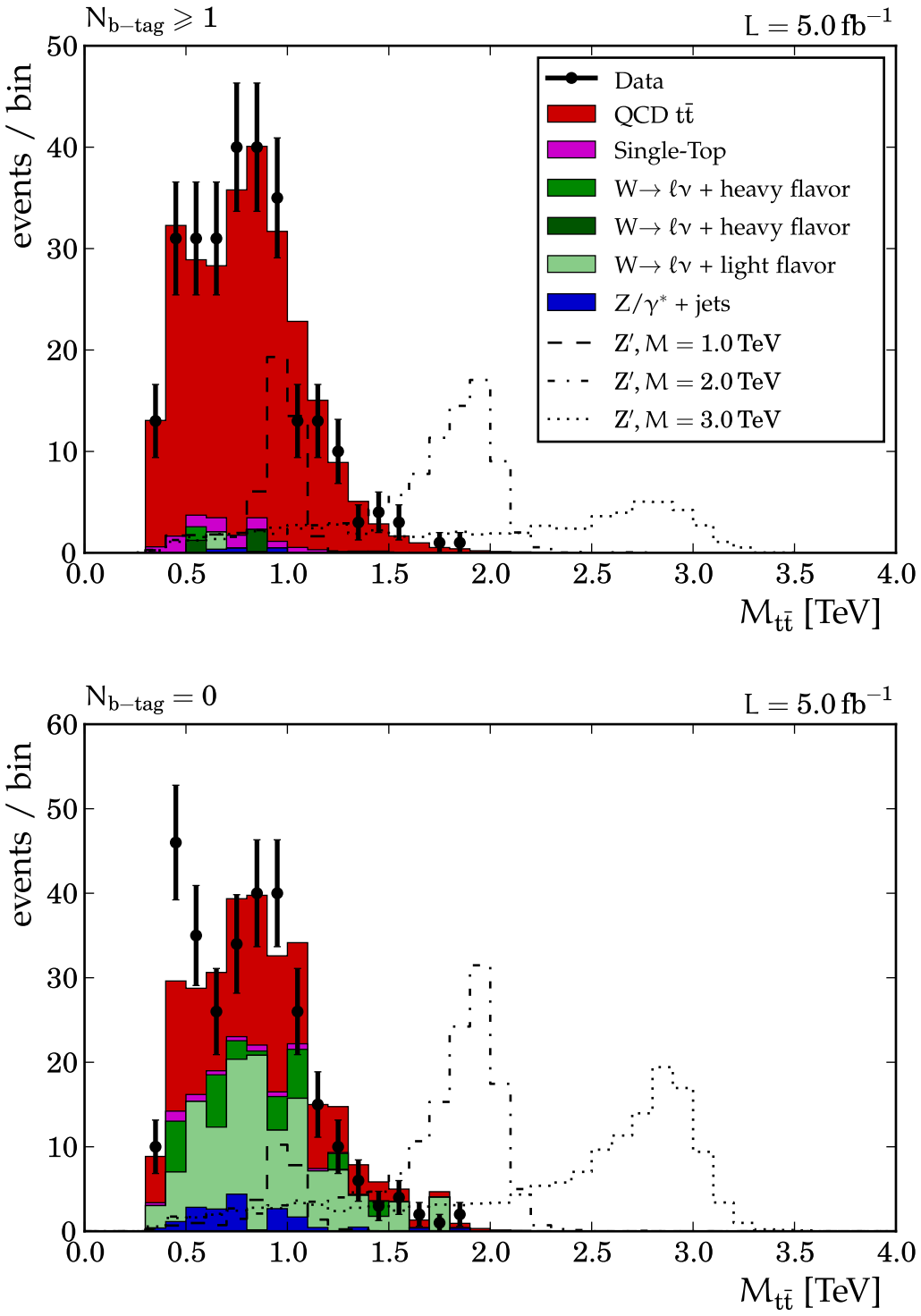

Figure 4.11: The $M_{t\bar{t}}$ distribution after the final event selection for the channels $N_{b\text{-tag}} \geqslant 0$ and $N_{b\text{-tag}} = 0$, showing narrow Z' signals using a cross section of 1 pb.

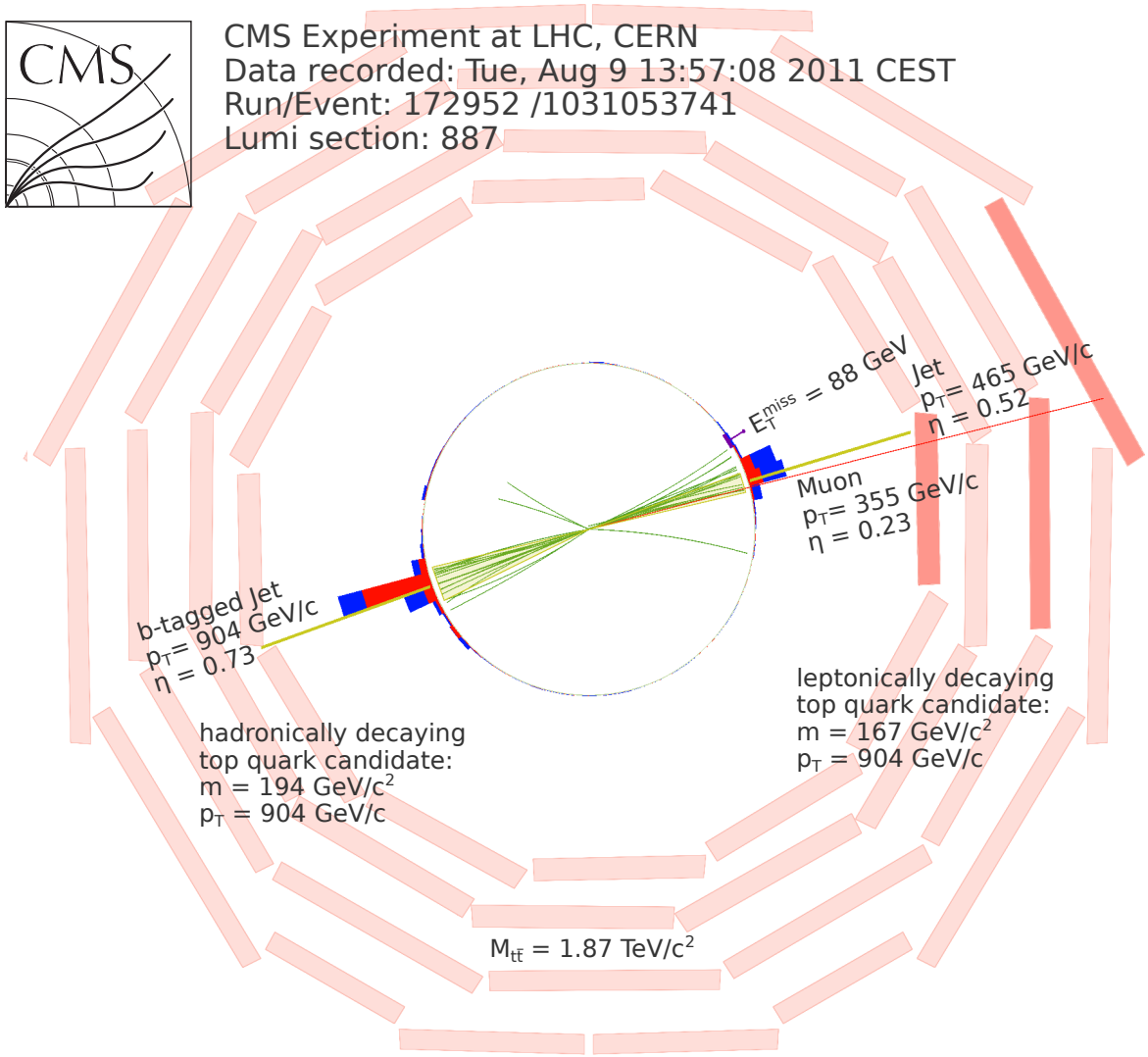

Figure 4.12: Transverse detector view showing the event with the highest value of $M_{t\bar{t}}$.

5 Statistical Analysis

The event selection and $t\bar{t}$ reconstruction discussed in chapter 4 allow the construction of $M_{t\bar{t}}$ distributions for both data and Monte-Carlo simulation. Comparing these distributions, upper limits on the cross sections for resonances $Z' \to t\bar{t}$ can be set. Formally, this involves defining a *statistical model* which specifies the probability to observe a certain dataset as a function of some underlying parameters such as the Z' cross section. This is described in section 5.1. Based on this model, various statistical methods for limit setting can be applied as introduced in section 5.2. The implementation of these methods in the theta framework, which has been developed in this analysis, is discussed in section 5.3.

This chapter introduces the methods and tools that are required in general to set upper limits on a cross section. The application of these methods to the $Z' \to t\bar{t}$ search is discussed in chapter 6, including the interpretation of these cross-section limits as lower mass limits within some specific Z' models.

5.1 Statistical Model

The statistical model specifies the probability to observe a certain dataset as a function of some real-valued parameters, including the parameter one wants to make statistical statements about, which is the signal cross section in this case. This section first introduces a simple statistical model which is subsequently extended to the more complicated model used in this analysis.

A simple model, which can be seen as a prototype for many analyses, is a counting experiment in one channel where the expected number of background events b is known and the signal cross section is the parameter of interest. In this case, the dataset is completely specified by the number of observed events, n, and the probability to observe n events follows a Poisson distribution,

$$\text{Poisson}(n|\lambda) = \frac{\lambda^n e^{-\lambda}}{n!}, \tag{5.1}$$

where λ is the Poisson mean predicted by the model. This Poisson mean λ is written as a function of the model parameters, the only model parameter being the unknown signal cross section σ_s. Rather than including σ_s as a model parameter directly, a *signal strength modifier* μ is used as parameter that scales the number of expected

signal events s. This expected number of signal events s is calculated for an arbitrary, but known signal cross section $\sigma_{s,0}$. Thus, the dimensionless parameter μ is the signal cross section in units of the cross section $\sigma_{s,0}$. The final result is expressed as a cross section and is given by $\mu \cdot \sigma_{s,0}$, which will not depend on the choice of $\sigma_{s,0}$. Now μ is the only model parameter and λ is given by

$$\lambda(\mu) = b + \mu \cdot s. \tag{5.2}$$

This completes the definition of the prototype model: The probability to observe a certain dataset (n), given the values of the model parameters (μ), is completely specified by equations (5.1) and (5.2).

The first extension to this prototype model is to use histograms instead of a single event count. In this case, the dataset n as well as the prediction λ are histograms whose bin contents for bin $i = 1, \ldots, N_{bin}$ are given by n_i and λ_i, respectively. The probability to observe the dataset n is given by the product of Poisson probabilities over all bins,

$$p(n|\lambda) = \prod_{i=1}^{N_{bin}} \text{Poisson}(n_i|\lambda_i) = \prod_{i=1}^{N_{bin}} \frac{\lambda_i^{n_i} e^{-\lambda_i}}{n_i!}. \tag{5.3}$$

For each bin i, λ_i is given by the sum of the expected number of background events and the scaled expected number of signal events as in equation (5.2). In general, more than one selection and physical observable is used, in which case the probability is given by taking the product over all these N_{chan} channels,

$$p(n|\lambda) = \prod_{c=1}^{N_{chan}} \prod_{i=1}^{N_{bin}^c} \text{Poisson}(n_{i,c}|\lambda_{i,c}), \tag{5.4}$$

where c denotes the channel and the dataset n. The prediction λ and number of bins N_{bin} both acquire a dependency on the channel c. However, note that equations (5.3) and (5.4) are equivalent if the bin index i in equation (5.3) runs over all bins in all channels. Therefore, the slightly simpler notation of equation (5.3) will be used in the following discussion, with the understanding that more than one channel can be used and the bin index i always runs over all bins used in the statistical analysis.

The second modification to the model is to explicitly write the expected number of background events b as a sum of the different contributing background processes which are determined separately,

$$b = \sum_{p=1}^{N_p} \lambda_p, \tag{5.5}$$

where N_p is the number of background processes considered. For more consistency of notation, the expected number of signal events s is called λ_s. This modification allows a simpler formulation of systematic uncertainties which often affect the different background process differently.

The third and last extension is to introduce systematic uncertainties. For each source of systematic uncertainty u, an additional model parameter θ_u is introduced. The expected number of events for process p in bin i, $\lambda_{p,i}$, is written as a function of these nuisance parameters. Different types of systematic uncertainties lead to different choices for the functional dependency of $\lambda_{p,i}$ on the nuisance parameters θ_u and will be discussed in sections 5.1.1 to 5.1.3.

In this analysis, a Bayesian concept for systematic uncertainties is used, which allows to write down a prior probability distribution for the nuisance parameters. The nuisance parameter priors are independent normal distributions with a mean of zero and a standard deviation of one. This can be assumed without loss of generality, as it is always possible to apply a transformation on a model parameter such that the prior in the new parameter is such a normal distribution with mean zero and width one.

The complete model can now be written as

$$p(n|\mu,\theta) = \prod_{i=1}^{N_{bin}} \text{Poisson}(n_i|\lambda_i(\mu,\theta)) \qquad \text{with} \tag{5.6}$$

$$\lambda_i(\mu,\theta) = \sum_{p=1}^{N_p} \lambda_{p,i}(\theta) + \mu \cdot \lambda_{s,i}(\theta), \tag{5.7}$$

$$\pi(\theta) = \prod_{u=1}^{N_{syst}} \text{Gauss}(\theta_u|0,1), \tag{5.8}$$

where the last line specifies the prior π for the nuisance parameters θ_u where

$$\text{Gauss}(x|x_0,\sigma) = \frac{1}{\sqrt{2\pi}\sigma} e^{-\frac{1}{2}\left(\frac{x_0-x}{\sigma}\right)^2} \tag{5.9}$$

is the Gaussian probability density for x with mean x_0 and standard deviation σ.

Equations (5.6) and (5.7) define the probability to observe the dataset n, given model parameters μ and θ. For a fixed dataset n, this expression can also be read as a function of μ and θ, known as the *likelihood function* $\mathcal{L}(\theta,\mu|n)$. In this thesis, the likelihood function always includes the prior terms for the nuisance parameters θ according to equation (5.8), and the likelihood function is thus given by

$$\mathcal{L}(\theta,\mu|n) = p(n|\mu,\theta) \cdot \prod_{u=1}^{N_{syst}} \text{Gauss}(\theta_u|0,1). \tag{5.10}$$

In the next sections, different types of systematic uncertainties are discussed and how they affect the prediction λ.

5.1.1 Rate Uncertainties

Theory cross-section uncertainties and uncertainties on the selection efficiency affect the overall rate of a process. They are included in the model by scaling all bins i of the histogram for process p, $\lambda_{p,i}$, by a bin-independent factor. If the nuisance parameter for the considered source of the uncertainty is θ_u and the best prediction for the mean in process p in bin i is $\lambda_{p,i,0}$, then the scaling used is

$$\lambda_{p,i}(\theta_u) = e^{\delta_{p,u}\theta_u} \cdot \lambda_{p,i,0}\,, \tag{5.11}$$

where $\delta_{p,u}$ is a constant connected to the relative uncertainty for this process assigned to this source of uncertainty; note that $\delta_{p,u}$ depends on the process p but not on the bin index i. If there are multiple rate uncertainties affecting the rate, each of them is included by adding another exponential factor.

To better understand how this uncertainty changes the prediction λ, one can choose a different but equivalent way to parameterize this uncertainty by replacing the exponential factor in equation (5.11) with a scale parameter ξ,

$$\xi := e^{\delta_{p,u}\theta_u}$$

The Gaussian prior for θ_u with mean 0 and width 1 is equivalent to a log-normal prior for ξ given by

$$p(\xi|\delta_{p,u}) = \frac{1}{\xi\delta_{p,u}\sqrt{2\pi}} e^{-\frac{(\ln\xi)^2}{2\delta_{p,u}^2}}\,, \qquad \xi > 0. \tag{5.12}$$

This probability density is shown in figure 5.1 for $\delta_{p,u} = 0.3$. One advantage of this distribution over using a scale factor with a Gaussian prior is that unphysical values $\xi < 0$ do not occur by construction. On the other hand, it can be observed that this log-normal distribution is not symmetric, which is reflected in the non-coincidence of the median, mean, and maximum of the log-normal density given in figure 5.1. If the relative systematic uncertainty for a process is Δ, the corresponding value for $\delta_{p,u}$ is set to $\log(1+\Delta)$. This results in a 1σ interval for the factor ξ of $\left[\frac{1}{1+\Delta}, 1+\Delta\right]$. The asymmetry of the log-normal distribution in ξ can be seen for large uncertainties, e.g. a "100% uncertainty" $\Delta = 1$ leads to a 1σ interval for ξ of $[1/2, 2]$.

Equation (5.11) can be generalized to asymmetric log-normal uncertainties by using two different coefficients $\delta_{p,u,\pm}$, where the sign of θ_u determines which one of those is used.

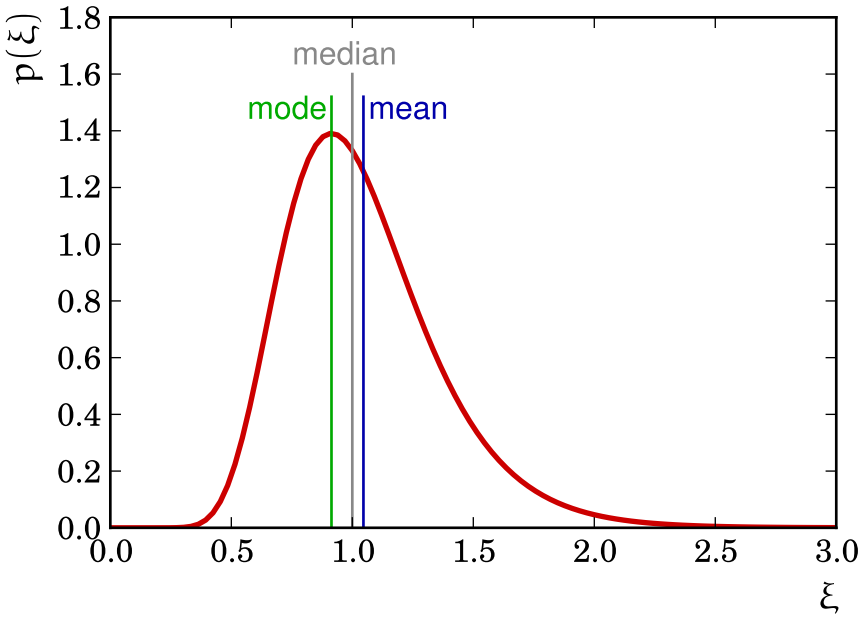

Figure 5.1: Log-normal probability density function $p(\xi|\delta_{p,u})$ for a scale factor ξ used to model rate uncertainties for $\delta_{p,u} = 0.3$. The mean is at $\xi = e^{\delta^2_{p,u}/2}$, the median is at $\xi = 1$ and the mode at $\xi = e^{-\delta^2_{p,u}}$.

5.1.2 Shape Uncertainties: Template Morphing

Some uncertainties do not only affect the expected overall rate of a process but also the shape of the histogram. One example would be the jet energy scale uncertainty shift, which would move an invariant mass peak to smaller or larger invariant masses.

For each uncertainty of this kind, in addition to the nominal prediction template for process p, $\lambda_{p,i,0}$, two more templates, one "up" and one "down" template are constructed by applying the $+1\sigma$ systematic shift and the -1σ shift corresponding to this uncertainty in the simulated events. Details about how such a shift is applied in simulated events depends on the uncertainty and are discussed in section 6.1. To include this effect in the statistical model, the nuisance parameter θ_u is used to interpolate between the nominal histogram and these two additional histograms. This is known as *template morphing*. The interpolation for $\lambda_{p,i}$ is performed such that for $\theta_u = 0$, the nominal histogram $\lambda_{p,i,0}$ is reproduced, and $\theta_u = \pm 1$ yields the "up" and "down" histograms. For values $|\theta_u| > 1$, $\lambda_{p,i}$ is chosen to be a linear function of θ_u going through the points at $\theta_u = 0$ and $\theta_u = \pm 1$. For the interpolation ($|\theta_u| < 1$), a cubic function is used such that the predicted event yield as a function of θ_u, $\lambda_{p,i}(\theta_u)$, is continuously differentiable at the points $\theta_u = \pm 1$ and its derivative at $\theta_u = 0$ is the average of the slopes of the linear extrapolation. These conditions determine the parameterization for the interpolation completely and for $|\theta_u| < 1$, it is

$$\lambda_{p,i}(\theta_u) = \lambda_{p,i,0} + \frac{1}{2}\theta_u \left(\lambda_{p,i,+} - \lambda_{p,i,-}\right) + \left(\theta_u^2 - \frac{1}{2}|\theta_u|^3\right)\left(\lambda_{p,i,+} + \lambda_{p,i,-}\right) \tag{5.13}$$

where $\lambda_{p,i,\pm}$ is the bin content of bin i for the "up" and "down" histograms for process p. This function is shown in figure 5.2. If more than one shape uncertainty is considered, the difference to the nominal bin content, $\lambda_{p,i}(\theta_u) - \lambda_{p,i,0}$, is determined for each uncertainty u and all these differences are added to the nominal bin content. For $|\theta_u| > 1$, it is possible that the resulting prediction after template morphing is smaller than zero. As this is unphysical, the value is set to zero in this case.

Template morphing techniques have been used, see e.g. [142], although with different dependence of the predicted yield as a function of the nuisance parameter. The functional dependence chosen here — with a cubic interpolation and a linear extrapolation — has the advantage that it is continuously differentiable. This leads to a continuously differentiable negative log-likelihood function, which is important for the numerical minimization. This parameterization was proposed by Jan Steggemann (unpublished).

An example for template morphing is shown in figure 5.3. The left plot shows the three templates for $M_{t\bar{t}}$ used for the jet energy scale uncertainty; the nominal template was constructed using the nominal jet energy corrections, while for the

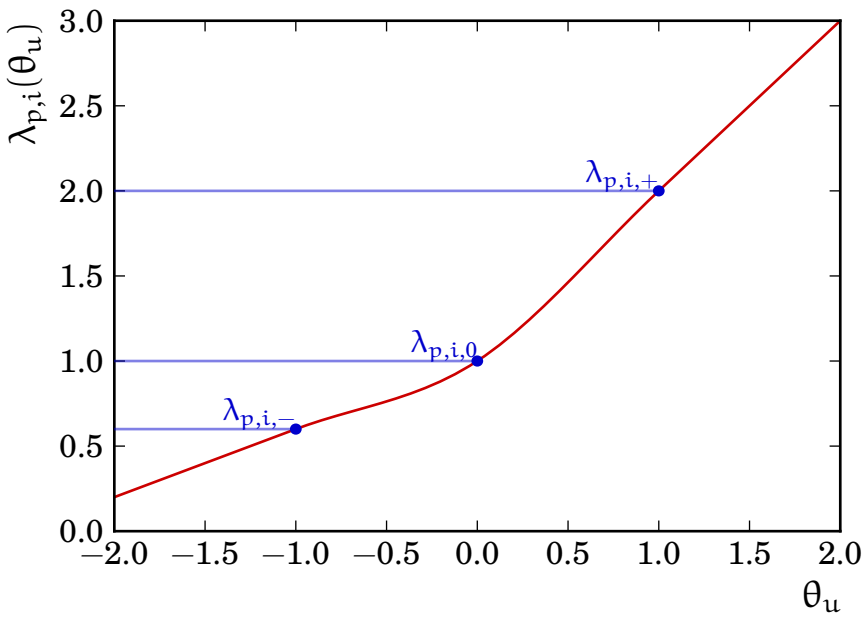

Figure 5.2: The prediction for process p in bin i, $\lambda_{p,i}$, as a function of the nuisance parameter θ_u used for template morphing. The interpolation for $|\theta_u| < 1$ uses a cubic function and the extrapolation for $|\theta_u| > 1$ is linear.

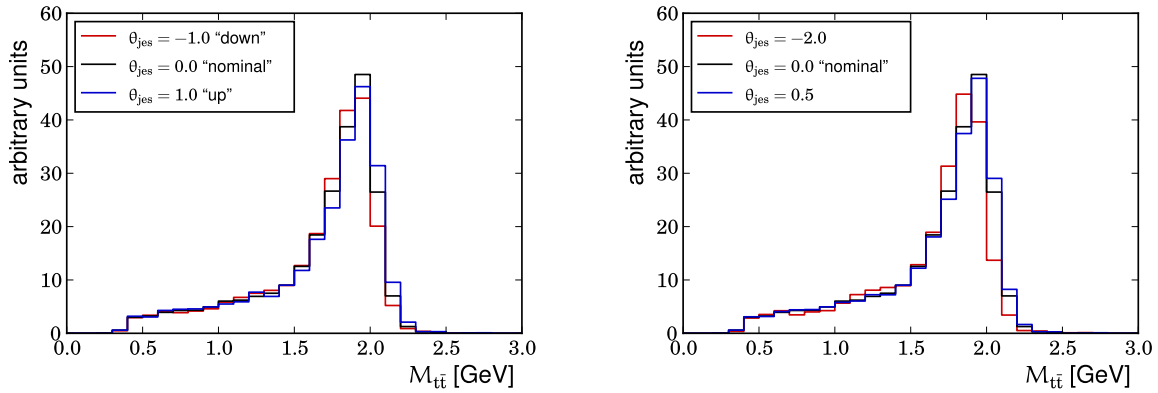

Figure 5.3: Example for template morphing for the Z′ sample with $M_{Z'} = 2\,\text{TeV}$ for the jet energy scale uncertainty. The left plot shows the input histograms used for the template morphing, while on the right, the output of the template morphing for different values of θ_{jes} is shown.

"up" ("down") template, the jet energies have been shifted up (down) by the p_T and η-dependent 1σ uncertainties. As expected, a small shift in the peak position can be observed. These templates are used as input for the template morphing; they are reproduced for values of the nuisance parameter $\theta_{jes} = 0, \pm 1$. The right plot shows the output of the template morphing for $\theta_{jes} = -2.0$, which results in a more extreme downward shift of the peak than the "down" histogram, and for $\theta_{jes} = 0.5$, which results in a peak shift between the "nominal" ($\theta_u = 0$) and "up" histogram ($\theta_u = 1$). This demonstrates that the template morphing qualitatively behaves as expected.

5.1.3 Uncertainties due to Limited Number of Simulated Events

If a histogram used in the statistical model for the description for the signal or a background process is built from a sample of simulated events, the limited number of simulated events in that sample is an additional source of systematic uncertainty. The predicted event yield for process p and bin i, $\lambda_{p,i,0}$, is obtained by counting the number of simulated events falling in bin i after the event selection, $N_{p,i,pass}$, multiplied by a weight factor which depends on the cross section of the considered process, σ_p, and integrated luminosity L,

$$\lambda_{p,i,0} = \frac{N_{p,i,pass} L \sigma_p}{N_{p,total}}, \tag{5.14}$$

where $N_{p,total}$ is the total number of simulated events in the sample for process p, before applying the event selection. In this procedure, the number of simulated events

$N_{p,i,pass}$ is a random variable with a binomial probability distribution with some selection efficiency $\epsilon_{p,i}$. For small selection efficiencies, the number of unweighted simulated events in bin i, $N_{p,i,pass}$, can be considered to follow a Poisson distribution with mean $\epsilon_{p,i} \cdot N_{p,total}$ with very good approximation. To include this uncertainty into the statistical model, one possibility is to include these Poisson probabilities for each process explicitly into the statistical model, a solution originally proposed by Barlow and Beeston in Reference [143]. In that proposal, the statistical model is extended to include one additional nuisance parameter per bin and process that is the true mean, denoted with $\lambda_{p,i,0,t}$. Using these additional parameters, one can write down the joint probability to observe both n_i data events in bin i, and $\lambda_{p,i,0}$ weighted simulated events in this bin.

In practice, this approach introduces a large number of additional nuisance parameters and numerical minimization algorithms used to find the maximum of the likelihood function often fail to converge. Also, this approach is only applicable directly if all simulated events for a given process have the same event weight. However, in this analysis, the event reweighting to correct the simulation for b-tagging and pileup discussed in section 3.3 assigns a different weight to each event.

The suggested modification in Reference [142] is to approximate the Poisson probability for $N_{p,i,pass}$ by a Gaussian. For a given process p and bin i, one can estimate the appropriate width for this Gaussian uncertainty on $\lambda_{p,i}(\theta)$ by the square root of the sum of the squared weights of the simulated events in this bin. This uncertainty is then propagated to the total predicted event yield in bin i, λ_i given in equation (5.7). This uncertainty on λ_i is denoted with Δ_i. The statistical model is extended to include one additional nuisance parameter per bin i, ν_i, which denotes the additive shift of the estimated mean λ_i to the true mean $\lambda_{i,t}$ which one would obtain with an infinite number of simulated events,

$$\lambda_{i,t}(\theta, \nu_i) = \lambda_i(\theta) + \nu_i, \tag{5.15}$$

where ν_i has a Gaussian prior around 0 with width Δ_i. Note that this approach is slightly different to the one in Reference [142] where the nuisance parameter is a factor, not a summand. The probability to observe dataset n, originally given in equation (5.6), is now

$$p(n|\mu, \theta, \nu) = \prod_{i=1}^{N_{bin}} \text{Poisson}(n_i|\lambda_i(\mu, \theta) + \nu_i). \tag{5.16}$$

The statistical methods discussed in the next section do not require the full likelihood function but rather the value of the likelihood function at the maximum taken

over all nuisance parameters. As intermediate step, the *profile likelihood function* $\mathcal{L}_p$ is defined which carries out this maximization in the parameters ν,

$$\mathcal{L}_p(\mu, \theta|n) = \max_{\nu} \mathcal{L}(\mu, \theta, \nu|n), \tag{5.17}$$

where $\mathcal{L}$ is the likelihood function defined in analogy to equation (5.10) based on the probability given in equation (5.16). The function $\mathcal{L}_p$ has very similar properties as the full likelihood function for all practical applications.

The important observation is that this maximization over ν can be performed analytically: Consider the partial derivatives of the logarithm of the likelihood function with respect to ν_i,

$$\frac{\partial \log L}{\partial \nu_i} = \frac{\partial}{\partial \nu_i} \left(\log \text{Poisson}(n_i|\lambda_i(\mu, \theta) + \nu_i) + \log \text{Gauss}(\nu_i|0, \Delta_i)\right) \tag{5.18}$$

$$= -1 + \frac{n_i}{\lambda_i(\mu, \theta) + \nu_i} - \frac{\nu_i}{\Delta_i^2}. \tag{5.19}$$

Setting this to zero for all ν_i in order to find the local extrema yields the following quadratic equation for each ν_i:

$$\nu_i^2 + \nu_i(\lambda_i(\mu, \theta) + \Delta_i^2) + \Delta_i^2(\lambda_i(\mu, \theta) - n_i) = 0, \tag{5.20}$$

which can be solved for ν_i. Only one of the two solutions yields a physical (non-negative) prediction $\lambda_i + \nu_i$ which is used to evaluate the full likelihood function. This procedure allows to calculate the profile likelihood function numerically in a robust way, avoiding the practical problems arising when applying minimization algorithms directly on the high-dimensional, full likelihood function based on equation (5.16).

5.2 Limit Setting Methods

In the field of statistics, one can identify two different schools: classical statistics (also known as "frequentist" statistics) and Bayesian statistics. These two approaches differ in their use of the term *probability* and actually give rise to different statistical methods.

In classical statistics, probability is defined as the relative frequency of an event. It is not meaningful to make statements about the probability distribution of a model parameter, such as the signal cross section μ: The signal cross section, while unknown, has one well-defined value in nature and is no random variable for which one can define a probability in the sense of a relative frequency, as there is no well-defined experiment one could repeat.

In Bayesian statistics, the term probability is not only used for relative frequencies as in classical statistics but can also be used to refer to a "degree of belief" and it is valid to make probabilistic statement about a model parameter, such as a probability density for the signal cross section.

In the analysis discussed in this thesis, the goal is to derive upper limits on the signal cross section. Both the classical and Bayesian approaches are used which lead to quite different methods. The classical interval construction is introduced first. Some modifications of this approach lead to the CL_s limit construction discussed in the second section and finally, the Bayesian approach is explained in section 5.2.3.

5.2.1 Classical Limits

For a given statistical model, any method setting upper limits on the parameter μ (which is considered to be the only model parameter) can be considered as a function assigning each observed dataset n the upper limit $\mu_\alpha(n)$, where α is a probability introduced below. In classical methods, the central property of a limit setting procedure is the *coverage probability*. It is the probability that the true parameter value is below the cited upper limit and is written as

$$p_\mu(\mu < \mu_\alpha(n)). \tag{5.21}$$

In general, this coverage probability depends on the true value of μ. A *confidence level* $(1-\alpha)$ means that the coverage probability of the method is at least $(1-\alpha)$ for all values of μ,

$$\forall_\mu p(\mu < \mu_\alpha(n)) \geqslant 1-\alpha. \tag{5.22}$$

Note that one would usually prefer equality in this Equation, but this is not always possible (e.g. due to discreteness of the data n), and the usual convention is to require the coverage to be larger in such cases, not smaller. This is known as *overcoverage* and the limit setting method used is said to be *conservative*.

The classical interval construction method is the Neyman construction [144], which guarantees the correct (over-)coverage. This construction is first introduced using a counting experiment where the outcome of the experiment is the number of observed events, n; generalizations will be discussed later.

The Neyman construction can be illustrated as constructing a belt in the n-μ-plane[1]: For a confidence level of $(1-\alpha)$, for each value of μ the belt in the n direction consists of the values n from n_0 to infinity such that the probability at this value of μ to measure a value $n \geqslant n_0$ is at least the confidence level $(1-\alpha)$. This belt is shown in

[1]Note that "belt" refers to the general case of a two-sided interval construction. In the case of upper limits discussed here, this "belt" extends to positive infinity in n.

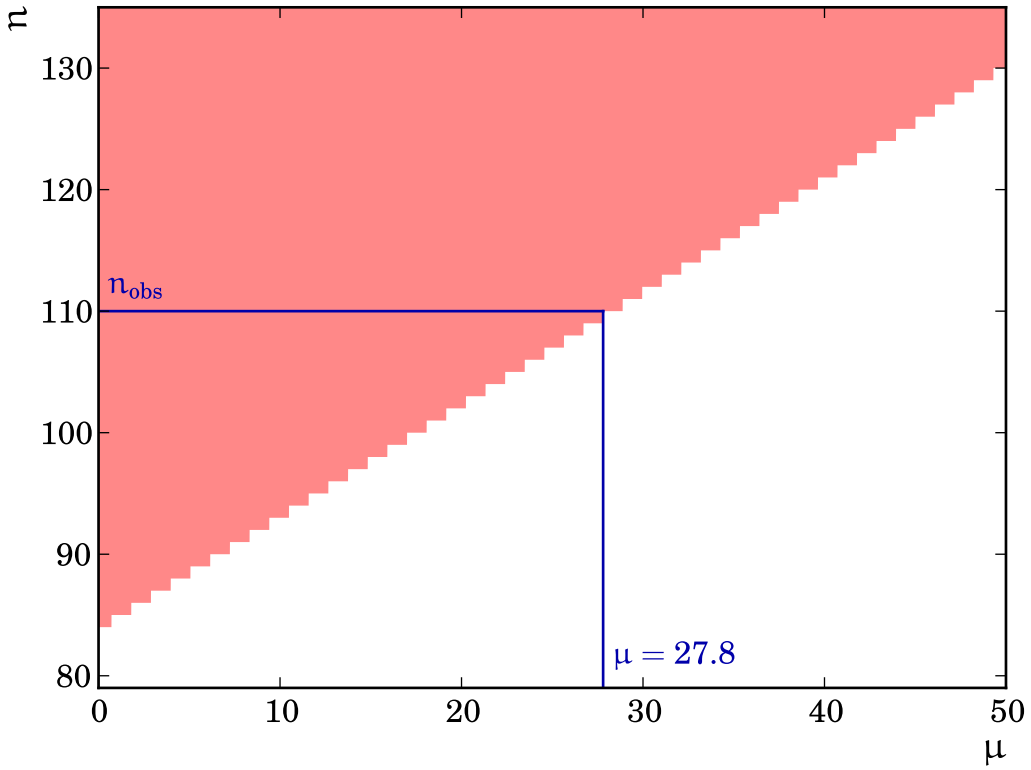

Figure 5.4: Neyman construction for 95% C.L. upper limits for a counting experiment with 100 expected background events and a measurement of $n_{obs} = 110$. The resulting 95% C.L. upper limit on the mean number of signal events is $\mu = 27.8$.

figure 5.4. For the measurement, the observed data n_{obs} is used to read off the upper limit for μ, as indicated in the figure. To see that this construction yields correct coverage, choose an arbitrary but fixed true value for μ. The probability to measure a value n within the belt is at least $(1 - \alpha)$, and exactly in those cases, this value for μ is part of the resulting interval. This is true for all values of μ and therefore equation (5.22) holds.

This construction can also be seen as an inverted hypothesis test where for upper limits, the null hypothesis $\mu = \mu_0$ is tested versus the (composite) alternative $\mu < \mu_0$. The 95% confidence level (C.L.) upper limit for μ is the smallest value of μ_0 for which the null hypothesis cannot be rejected at the $\alpha = 0.05$ level.

To generalize this construction to analyses with more than one channel, the multi-

dimensional dataset has to be reduced to one real number that summarizes the compatibility with the tested hypothesis, known as the *test statistic*. In the convention used here, large test statistic values refer to greater incompatibility with the null hypothesis. The optimal choice for the test statistic is the likelihood ratio test statistic, according to the Neyman-Pearson lemma [145]. It is optimal in the sense that it maximizes the probability to reject the null hypothesis for a given type-I error rate α, which is the probability to reject the null hypothesis although it is true. However, this is only applicable in cases where both the null hypothesis and the alternative hypothesis are not composite hypotheses, i.e., do not contain any free parameters, and it is therefore not directly applicable here. A common choice for the test statistic in this case is to use the ratio of profile likelihood functions [146], where the full likelihood function is maximized over all parameters in the parameter space allowed by the respective hypothesis. In the case for upper limits where the null hypothesis is $\mu = \mu_0$ and the alternative is $\mu < \mu_0$, the test statistic thus is

$$q_{\mu_0}(n) = \ln \frac{\max_{\mu<\mu_0,\theta} L(\mu, \theta|n)}{\max_{\theta} L(\mu_0, \theta|n)}, \tag{5.23}$$

where θ denotes the nuisance parameters.[2]

To construct the Neyman band, the probability distribution for q_{μ_0} has to be known. In general, this distribution is not known analytically. Rather, the statistical model is used to construct an empirical distribution function by generating a large sample of random pseudo datasets and for each pseudo dataset, the value for the test statistic is calculated. This ensemble can then be used for the construction of intervals.

If introducing systematic uncertainties via nuisance parameters into the problem, the classical approach requires that the coverage probability in equation (5.22) holds not only for all values of μ but also for all values of the nuisance parameters θ. However, most interval construction schemes (such as the Neyman construction discussed above) in general have many issues in practice as they require projecting the generalized band construction, which is performed in the full model parameter space, onto the axis of the parameter of interest. These problems of eliminating nuisance parameters in classical interval construction are known in the statistics literature, for example the Behrens-Fisher problem, for which it is impossible to construct intervals with the desired properties [147], or Fillier's problem, which can lead to infinite confidence intervals [148] which are useless in practice. Therefore,

[2]The logarithm is included here mainly for implementation and illustration purposes in order to avoid extremely small values while calculating the test statistic which in practice would often be smaller than the smallest number representable by usual floating point arithmetic used on CPUs. The result of the limit setting method itself is not affected and in general, any strictly monotonic transformation can be applied to the test statistic without changing the result.

an approach often taken that is also followed in this analysis is to adopt a Bayesian standpoint for the nuisance parameters and replace the coverage condition from equation (5.22) by an *average* coverage where the average is taken over all nuisance parameters using their priors, while this coverage condition is still required to hold for all true values μ; no averaging over μ is performed.

5.2.2 CL_s Method

The CL_s method [149, 150] modifies the classical interval construction to remove some undesired properties of a purely classical interval construction that appear in searches for a small signal on top of a large background, where overestimating the background yields smaller upper limits on the signal cross section. This effect is mitigated in the CL_s construction by also considering the compatibility of the observation with the background-only hypothesis. The CL_s upper limit at $(1-\alpha)$ confidence level is the value of μ for which

$$CL_s(\mu, q_\mu^{obs}) = \frac{CL_{s+b}(\mu, q_\mu^{obs})}{CL_b(q_\mu^{obs})} = \alpha, \tag{5.24}$$

where CL_{s+b} is the probability to observe a dataset with true signal μ with a test statistic value larger than q_μ, and CL_b is the corresponding probability without signal ($\mu = 0$). Note that setting the denominator CL_b to 1.0 corresponds to the original Neyman construction discussed in the previous section. The limits obtained with the CL_s method are therefore always larger than the one obtained from a Neyman construction, but they are more robust in cases where the background level is overestimated.

5.2.3 Bayesian Method

The Bayesian method uses the Bayesian concept of probabilities introduced above, which allows to assign probability densities to the parameters of a model such as μ. Bayes' theorem is used to derive an expression for the posterior density for the model parameters μ and θ:

$$p(\mu, \theta|n) = \frac{p(n|\mu, \theta)\pi(\mu)\pi(\theta)}{p(n)}, \tag{5.25}$$

where $p(n|\mu, \theta)$ is given by the statistical model explained in section 5.1, $\pi(\theta)$ is the prior for the nuisance parameters, $\pi(\mu)$ is the prior for the signal cross section and the denominator $p(n)$ is the total probability to observe the dataset n. The denominator

can be expressed with the other ingredients,

$$p(n) = \int_{\theta,\mu} \pi(\theta)\pi(\mu)p(n|\mu,\theta), \tag{5.26}$$

and is a constant ensuring that the posterior density $p(\mu,\theta|n)$ is a properly normalized probability density function. Note that this probability is not well-defined if using improper priors such as flat priors in the signal strength μ, as the expression in the integral diverges. However, all the methods applied later do not require explicit normalization of the posterior, and only the nominator in the right hand side of equation (5.25) has to be calculated.

The prior for μ can be chosen to be constant on the interval from zero to infinity. While this is not a proper probability density (as it cannot be normalized), the expression for the posterior on the right hand side of equation (5.25) can still be calculated and normalized, given that the probability $p(n|\mu,\theta)$ falls fast enough as a function of μ—which is always fulfilled in the cases considered here. The priors for the nuisance parameters θ, $\pi(\theta)$, are independent normal distributions with mean zero and standard deviation one, as introduced in the model earlier in section 5.1.

The choice of priors, in particular for the parameter of interest μ, is arbitrary to some extent and considered subjective. This is a main source of criticism of the Bayesian approach which has inspired the developments of formal selection rules for the priors [151]. However, they are not widely used in high-energy physics and for setting upper limits on a Poisson signal, a flat prior for the signal cross section μ yields similar results as the classical construction and has similar coverage properties. Therefore, a flat prior for μ is used in this analysis.

While equation (5.25) defines the posterior in all model parameters, the marginal posterior in the signal cross section μ is required to construct upper limits for μ. This marginal posterior $p(\mu|n)$ is given by integrating over all nuisance parameters,

$$p(\mu|n) = \int_{\theta} p(\mu,\theta|n)d\theta\,, \tag{5.27}$$

where the integrand $p(\mu,\theta|n)$ is the posterior given by equation (5.25) includes the prior. This integral often has many dimensions (more than 10), and its calculation requires numerical integration methods suitable for those situations. The used algorithm is discussed in section 5.3.2.

5.3 The theta Framework

The theta framework is a set of computer programs, scripts, and libraries developed within this thesis. It is designed for making statistical analyses for template-based

models, as introduced in section 5.1. The statistical model is the product of Poisson probabilities as given in equation (5.6). In general, theta is an extensible framework that allows the user to create C++ plugins to model arbitrary dependencies of the prediction λ_i on the model parameters μ and θ.

Many methods, especially classical frequentist methods, require the generation of a large number of pseudo datasets, e.g. to get an empirical distribution of a test statistic, or for coverage tests. For this reason, theta is optimized for this use case and contains many speed optimizations, for example by making use of vector instructions found in modern CPUs and the available methods of parallelization and distributed computing.

In many analyses, including the Z′ search discussed here, only the log-normal rate uncertainties and the template morphing discussed in section 5.1 are used. For this case, Python scripts have been developed which automatically build the statistical model from a ROOT [152] file. This file has to contain all histograms required to define the statistical model in a certain naming convention, i.e. the histograms with the predictions for all channels and processes for the "nominal" templates and the "up" and "down" shifted histograms used for template morphing. The log-normal rate uncertainties are added using simple Python statements in a script.

One useful construction used in the algorithms discussed below is the *Asimov dataset*. This is a fictitious dataset n that is defined by setting the number of observed events in bin i, n_i, to the predicted number of events λ_i, evaluated at the most likely values of the nuisance parameters. While the Poisson means λ_i are in general not integers, this is not a problem as the expressions defining the likelihood function given in equation (5.6) can still be evaluated. This likelihood function of the Asimov dataset can be used to derive reasonable values for the step sizes for the nuisance parameters required by Markov Chain Monte-Carlo method and numerical minimization algorithms, as discussed below. The dataset also represents the "most likely" outcome and can be used as observed dataset to evaluate the expected outcome of a statistical method.

5.3.1 CL_s Method

The CL_s method is based on solving equation (5.24) numerically. First, the test statistic values q_μ are determined for data for different values of μ, q_μ^{obs}. The test statistic in equation (5.23) is found by numerical minimization of the negative log-likelihood using the general-purpose minimizer MINUIT [153]. For these values q_μ^{obs}, the value of CL_s is determined by using pseudo datasets. These pseudo datasets are generated according to the statistical model given in equations (5.6) to (5.8) and the test statistic value $q_\mu(n)$ is calculated for each pseudo-dataset n to get an empirical distribution

function for the underlying test statistic distribution.

As an example, two test statistic distributions for a narrow resonance Z' with $M = 2\,\text{TeV}$ are shown in figure 5.5 which were made using 10,000 pseudo datasets in each case. For this example, the signal normalization is chosen such that μ is the signal cross section in picobarn. It shows the q_μ distribution for $\mu = 0.05$ for pseudo datasets generated without signal for the calculation of CL_b ("b only") and for with the signal scale factor set to $\mu = 0.05$ to calculate CL_{s+b} ("s+b"), see equation (5.24). The q_μ distribution has a peak at 0.0 for both cases. This happens when the likelihood values at the maximum of the likelihood in the nominator and denominator in equation (5.23) coincide. The test statistic value for data, q_μ^{obs}, is also indicated in the plot. The fraction of s+b (b only) pseudo datasets with larger values than q_μ^{obs} define CL_{s+b} (CL_b). In this case, the found values are

$$\begin{aligned} CL_{s+b} &= 0.017 \pm 0.0013, \\ CL_b &= 0.12 \pm 0.003, \quad \text{and} \\ \Rightarrow CL_s &= \frac{CL_{s+b}}{CL_b} = 0.14 \pm 0.012, \end{aligned}$$

where the uncertainties for CL_{s+b} and CL_b are the binomial uncertainties due to the limited number of generated pseudo datasets, which are propagated to CL_s using Gaussian error propagation. As the CL_s value is above $\alpha = 0.05$, the 95% C.L. upper limit $\mu_{0.05}$ will be larger than the tested value $\mu = 0.05$.

While the method discussed so far allows to calculate the value of CL_s as a function of μ, the 95% C.L. upper limit requires to find the value $\mu_{0.05}$ for μ such that the CL_s value is $\alpha = 0.05$. The algorithm used is similar to the tool based on RooStats [154] that is used for computing Higgs boson cross-section limits at CMS and ATLAS [146]. First, the CL_s calculation is repeated for different values of μ in order to find an interval in μ that contains CL_s values significantly above and below the desired CL_s value of $\alpha = 0.05$. In this interval in μ, an exponential fit to the CL_s values as a function of μ is performed in order to find an estimate for the limit $\mu_{0.05}$. The uncertainties due to the limited number of pseudo datasets are propagated to $\mu_{0.05}$; more pseudo datasets are generated for a random value of μ in the fit interval until the desired accuracy on $\mu_{0.05}$ is reached.

5.3.2 Markov Chain Monte-Carlo

The Markov chain Monte-Carlo method is an algorithm to sample from a probability density function. It generates points $x \in R^k$ in the k-dimensional parameter space which are distributed according to a probability density function given by f. It is particularly suitable if the number of dimensions k is large. In these cases the

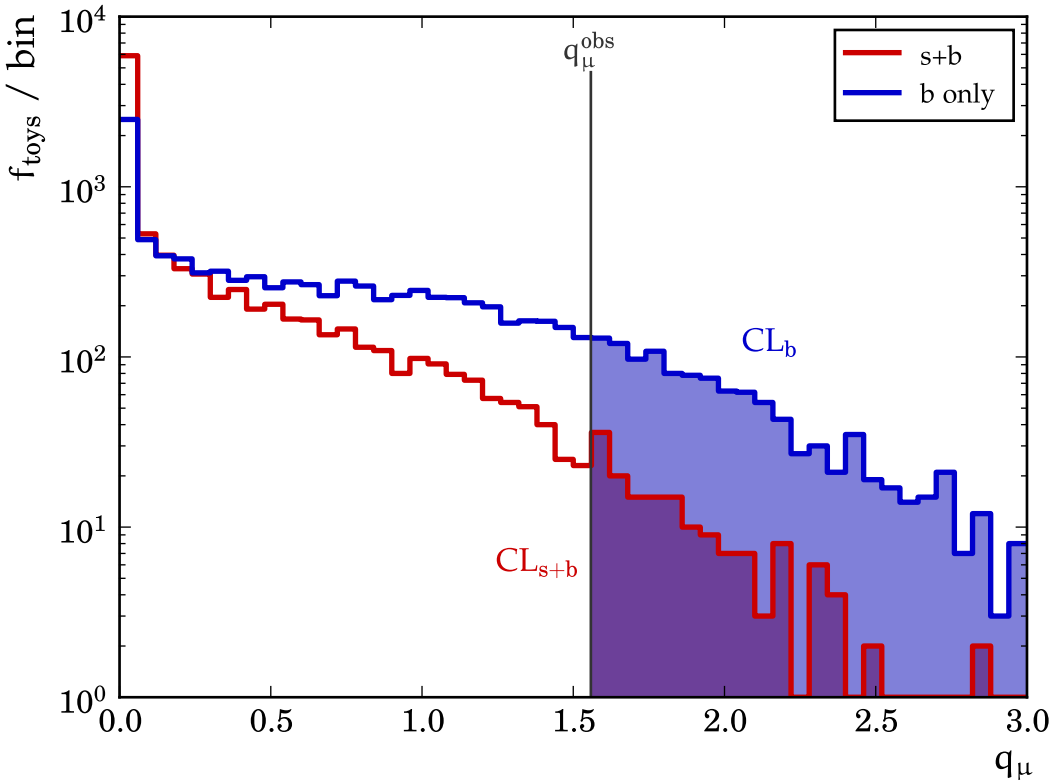

Figure 5.5: Distribution for the test statistic q_μ with the fraction of pseudo datasets per bin for pseudo datasets either generated with signal ($\mu = 0.05$) or without signal ($\mu = 0$). The shaded areas are the fraction of pseudo datasets (toys) with test statistic values above q_μ^{obs} and define the CL_{s+b} and the CL_b values used for the calculation of CL_s.

straight-forward integration algorithm of calculating $f(x)$ for values x arranged in a regularly-spaced grid in k dimensions requires a large number of function evaluations which grows exponentially with the number of dimensions k. Depending on the problem, the practical limit is already reached with $k = 3$–5. On the other hand, the Markov chain Monte-Carlo method does not require an exponentially growing number of function evaluations and is thus suitable to integrate the posterior density which for the current analysis has $k = 17$ (see section 6.1).

The Markov chain Monte-Carlo algorithm used here was first introduced by Metropolis et al. in the context of generating microstates distributed according to the Boltzmann distribution in a thermodynamical system [155]. This idea was later generalized by Hastings [156], and the algorithm is therefore known as *Metropolis-Hastings* algorithm. The algorithm to construct the Markov Chain $x_0, \ldots, x_n$, given the probability density f, consists of the following steps:

1. Pick a starting point x_0 for which $f(x_0) > 0$.

2. Using the current point x_i, construct a proposal point

$$x'_i = x_i + \Delta x \tag{5.28}$$

   where Δx is a random vector distributed according to the *proposal density* $p(x)$ discussed in more detail below.

3. The proposal point is *accepted* with the probability $\min(1, \frac{f(x'_i)}{f(x_i)})$ and *rejected* otherwise. Accepting the proposal point means setting $x_{i+1} := x'_i$; rejecting it repeats the current point, $x_{i+1} := x_i$.

4. Repeat steps 2 and 3 until the desired chain length is reached.

Note that according to step 3, the proposal point x'_i is always accepted if the posterior density at the proposal point is larger than the one at the current point. So the chain will always go to the proposal point x' if the posterior density is larger there, but it will also allow a decreasing density with some probability. A more detailed analysis, which is not discussed here, shows that the values x_i in the resulting Markov chain are distributed according to the density f, if some rather general conditions for the proposal density p are met, which is always the case for the choices of p discussed here.

This algorithm is applied using the posterior from equation (5.25) as the density f. Note that the algorithm does not require the density f to actually be normalized as the algorithm only depends on ratios of density values where any constant factor cancels. Therefore, it is enough to know the nominator on the right hand side of equation (5.25), as already discussed in section 5.2.3.

The crucial point for the algorithm to work in practice is the choice of the proposal probability density function $p(x)$. One possible choice is to use a multivariate Gaussian. However, the covariance matrix has to be chosen with care: if the width of the Gaussian is much smaller than the typical scale in x with which f changes, then the proposal point will be accepted very often and the Markov chain is effectively a random walk, which would require a huge chain length to reasonably cover all allowed regions of the parameter space. If on the other hand the width is too large, the function value at the proposal point is always be very small and most proposals are rejected, again requiring very long chains to reasonably cover the allowed parameter values. According to [157], the ideal choice in case f is a multivariate Gaussian is to use a multivariate proposal function with the same covariance, but scaled by a factor of $2.38/\sqrt{k}$ where k is the dimensionality of the problem. This proposal density is used in theta.

From the arguments about the correct proposal density it can also be seen that the acceptance rate is an important indicator of whether the chosen proposal function is reasonable. While typical acceptance rates in general depend on the problem and can span large ranges, extreme values such as acceptance rates lower than 5–10% or over 70–80% usually indicate that the choice for the proposal function is not adequate.

In general, many similar pseudo datasets are analyzed in theta, and their posteriors will have similar covariances. Therefore, the covariance matrix for the proposal function is determined once for many pseudo datasets, using the posterior constructed with the Asimov dataset introduced in section 5.3. The covariance matrix is estimated iteratively from Markov chains: The first covariance matrix is a diagonal matrix in which the diagonal elements are derived from the change of the posterior density along the respective axis. Using this matrix for the proposal density a Markov chain is constructed and the covariance matrix from the chain elements is calculated. This covariance matrix is then used for the proposal density of the next chain. This is repeated until the acceptance rate of the Markov chain is stable, or a maximum number of iterations has been reached.

A Markov chain for the posterior consists of points in the μ-θ space. The μ values of this chain are distributed according to the marginal posterior $p(\mu|n)$ defined in equation (5.27). The 95% C.L. upper limit can be estimated as the 95% quantile of the μ values in the chain. The upper limit obtained in this way carries an uncertainty due to the limited length of the Markov chain. As the chain elements are not statistically independent, and the dependence is not known, this uncertainty cannot be calculated directly. Instead, this uncertainty can be estimated with a bootstrapping method by repeating the limit setting procedure with different random seeds and using the variance of the obtained limits as an estimate for this uncertainty.

The chain elements can also be used to estimate the posterior density for $p(\mu|n)$ by

filling the values for μ in a histogram. While this procedure yields a valid estimate for the posterior, the chain length required to obtain a histogram with reasonably small uncertainties in each bin is very large. Therefore, a method has been developed which calculates the marginal posterior density $p(\mu|n)$ at l equidistant points $\mu_{min}, \ldots, \mu_{max}$ directly, yielding a smooth estimate for the posterior. For $j = 1, ..., l$, the estimated posterior density at μ_j is given by

$$\hat{p}(\mu_j|n) = \int_\theta p(\mu_j, \theta|n) d\theta.$$

This integral can be evaluated using the values for θ from the Markov chain by evaluating the posterior values $p(\mu_j, \theta|n)$ for all $j = 1, \ldots, l$ and each chain element θ. As an example, the posterior density obtained with this method for a narrow Z' resonance with $M = 2\,\text{TeV}$ is shown in figure 5.6.

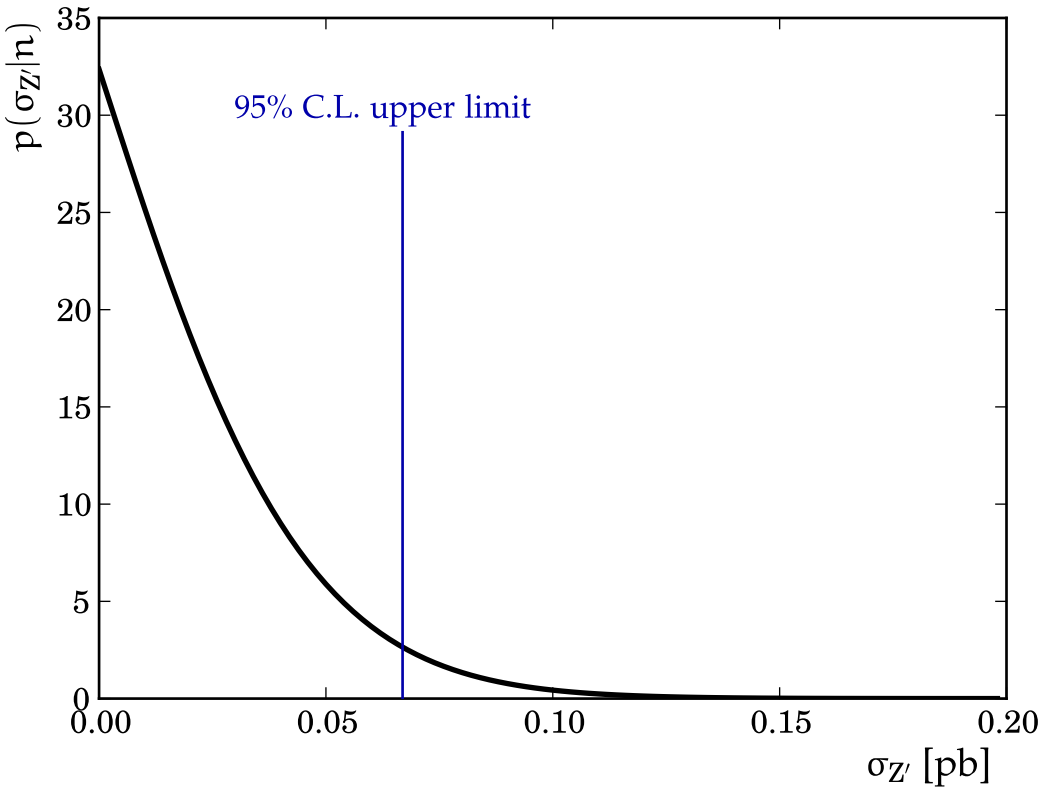

Figure 5.6: The marginal posterior for the cross section $\sigma(pp \to Z' \to t\bar{t})$ for a narrow resonance Z' with $M = 2\,\text{TeV}$. The 95% C.L. upper limit on the signal cross section is the 95% quantile of this posterior; it is indicated with the vertical line.

6 Results

This chapter describes how the methods for setting upper limits introduced in chapter 5 are applied to the analysis described in this thesis. Section 6.1 summarizes all systematic uncertainties considered in the statistical model, which is discussed in more detail in section 6.2. Finally, the results for the upper limits on $\sigma(pp \to Z' \to t\bar{t})$ as a function of the mass of the resonance for different resonance types Z' are presented in section 6.3, which also interprets these limits as lower limits on the resonance mass within a some specific Z' models.

6.1 Summary of Systematic Uncertainties

This section summarizes all sources of systematic uncertainties considered in the statistical model used in this analysis. As discussed in section 5.1, each source of uncertainty corresponds to one nuisance parameter in the statistical model with a Gaussian prior. In total 16 sources of uncertainty are considered in this analysis. Of these uncertainties, 9 are rate uncertainties as discussed in section 5.1.1. The relative rate uncertainties for the processes are given in table 6.1. The theory cross-section and acceptance uncertainties given in this table have been introduced in section 3.4. The acceptance uncertainties for the W+jets matching and scale uncertainties are derived from the alternate W+jets samples discussed in section 3.4. As these samples have only a few number of simulated events, the $M_{t\bar{t}}$ shape and rate change is determined for a looser event selection that omits the χ^2_{min} requirement and the b tagging categorization. As no shape difference has been found, both uncertainties are treated as rate uncertainties rather than as shape uncertainties.

The muon efficiency uncertainty is discussed in section 3.2.2; for details about the luminosity uncertainty see section 2.2.5.

The remaining 7 uncertainties are shape uncertainties treated via template morphing as discussed in section 5.1.2. For each shape uncertainty and affected process two alternative templates "up" and "down" are constructed using the simulated samples in which the systematic shift is applied at $+1\sigma$ and -1σ and re-deriving the $M_{t\bar{t}}$ templates. What this means specifically for each uncertainty is discussed in more detail for each uncertainty:

- The **jet energy scale** (JES) uncertainty is evaluated by simultaneously changing

all jet four vectors in all simulated events by the p_T and η-dependent jet energy scale uncertainties discussed in section 3.2.5 by $1 \pm \delta_{jes}(p_T, \eta)$ for the "up" and "down" templates, where δ_{jes} is the relative jet energy scale uncertainty. The typical impact of the JES uncertainty on the acceptance is about 6–8% for the background processes and about 3–6% for the signal, decreasing with increasing resonance mass.

- The **jet energy resolution** (JER) uncertainty is evaluated by scaling the difference of the reconstructed and generated jet p_T by different, η-dependent factors, as discussed in section 3.2.5. The typical impact of the JER uncertainty on the process yields is about 1–3%.
- The **b-tagging efficiency** and **b mistag rate** uncertainties are treated via event reweighting by using the $\pm 1\sigma$ scale factors as discussed in section 3.3. The typical change in acceptance due to the efficiency uncertainty is about 5–7% for processes containing b quarks, and smaller for other processes. The impact of the b mistag rate uncertainty is $\ll 1\%$ for all processes.
- The **pileup uncertainty** is treated by reweighting the generated pileup spectrum to the pileup expected in data with different assumptions about the total inelastic cross section as discussed in section 3.3. The change in acceptance is around 1% and becomes smaller for higher invariant $t\bar{t}$ masses.
- The **$t\bar{t}$ Q^2 scale** and **$t\bar{t}$ matching** uncertainties are derived by using alternative simulated $t\bar{t}$ samples with altered generator settings as discussed in section 3.4. This uncertainty only affects the $t\bar{t}$ background and changes the acceptance of up to 20%, depending on the channel.

6.2 Statistical Model

The histograms used for the statistical model are the two $M_{t\bar{t}}$ distributions for $N_{b\text{-tag}} = 0$ and for $N_{b\text{-tag}} \geqslant 1$ as introduced in section 4.4.2. In the histogram bins for small and for large values of $M_{t\bar{t}}$, the number of simulated events is low, resulting in a large uncertainty as discussed in section 5.1.3. Therefore, some of the $M_{t\bar{t}}$ bins are merged to ensure that this uncertainty does exceed 20% only for very few bins. The chosen binning has one low-mass bin from 0 to 0.4 TeV, followed by an equidistant binning with a bin width of 0.1 TeV between 0.4 and 1.3 TeV and one high-mass bin extending from 1.3 to 3 TeV. The remaining uncertainty due to the limited number of simulated events is treated with the method discussed in section 5.1.3. In addition, all uncertainties discussed in section 6.1 are also included in the statistical model.

Process	Relative yield change (%)
Theory cross-section uncertainties	
Z+jets	± 100
W+light flavor	± 50
W+heavy flavor	± 100
$t\bar{t}$	± 15
Single-Top	± 50
Theory acceptance uncertainties	
W+jets matching	$\pm\ 8$
W+jets Q^2 scale	$+76/-38$
Experimental uncertainties	
Luminosity	± 2.2
Muon efficiency	± 5

Table 6.1: Systematic uncertainties treated as rate uncertainties. The values in this table are the relative uncertainty on the yields Δ as introduced in section 5.1.1.

In order to illustrate whether the model can qualitatively describe the data, a maximum likelihood fit is performed, which yields estimates for all nuisance parameters. The parameter values at the maximum are found to be in agreement with the prior expectation, i.e. the values found indicate no disagreement to the assumed Gaussian priors around 0 with width 1. Using these parameter values, the model prediction is evaluated by applying template morphing and rate uncertainties as discussed in sections 5.1.1 and 5.1.2. The values for the nuisance parameters ν_i introduced to treat the uncertainty due to the limited number of simulated events discussed in section 5.1.3 are not explicitly determined and used for the evaluation of the prediction of the statistical model, effectively setting them to zero. The resulting histograms for both channels and all processes are shown in figure 6.1. The uncertainty bands show the only uncertainty which is not propagated to the model prediction after minimizing it, i.e. the uncertainty due to the limited number of simulated events corresponding to the nuisance parameters ν_i.

Three different types of resonances, all referred to as Z' are used, as discussed in section 3.1.2: A *narrow* resonance with a natural width of 1% which is a generic model for any resonance whose natural width is much smaller than the experimental $M_{t\bar{t}}$ resolution, a *wide* resonance with 10% natural width, and *Kaluza-Klein gluons*.

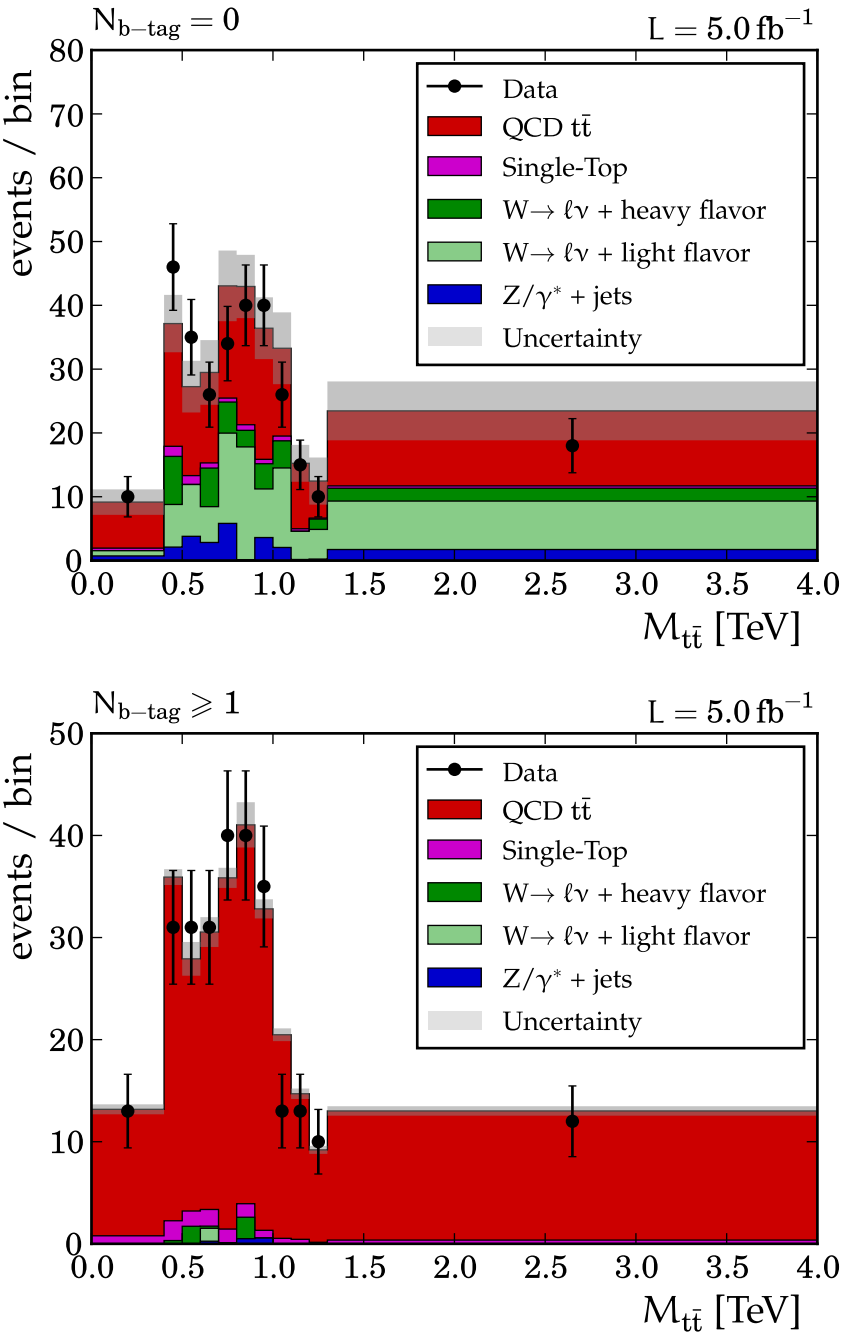

Figure 6.1: Comparison of data and the prediction of the statistical model for the $M_{t\bar{t}}$ distribution, evaluated at the parameter values which maximize the likelihood function in case of background only. The uncertainty is from limited size of the simulated Monte-Carlo samples.

In all cases, the considered mass range extends from 1–3 TeV, where the limits are evaluated at a spacing of 50 GeV, which is well below the $M_{t\bar{t}}$ resolution.

The models used to derive mass limits from the cross-section limits are a leptophobic topcolor Z′ [3] model with 1.2% and 10% width denoted with Z'_t and the Kaluza-Klein gluon model described in Reference [5].

6.3 Cross Section and Mass Limits

The CL_s method and the Bayesian method introduced in chapter 5 are now applied for setting upper limits on the cross section $\sigma(pp \to Z' \to t\bar{t})$ as a function of the resonance mass and the type of the resonance (narrow, wide, KK gluon).

For both limit setting methods, the *expected* limit can be evaluated using background-only pseudo datasets. These datasets are generated according to the statistical model by first generating random values for all nuisance parameters θ by sampling from their priors. These nuisance parameter values are used to calculate the predicted mean value λ_i in bin i. The number of events in bin i, n_i, is drawn from a Poisson distribution around λ_i. Then the limit is computed for this pseudo dataset as if it were real data. This is repeated two thousand times. The median value of these limits at each mass point define the expected limit. In order to illustrate the spread of expected limits, the 16% and 84% quantiles of these limits are displayed as the 1σ band of expected limits, with the rationale that if repeating the experiment many times, the observed limit is expected to be within this band in 68% of the cases, which corresponds to the area under a Gaussian distribution within $\pm 1\sigma$. Correspondingly, the 2σ band indicates the central 95% of the limits obtained from the 2.5% and the 97.5% quantiles of the limits obtained from the pseudo datasets. As these expected limit bands are susceptible to fluctuations in the pseudo datasets, the curve of the expected limit as a function of the mass is smoothed in the plots.

The limits on the cross section can also be interpreted in the context of specific models that predict such resonances: Any resonance mass for which an excluded cross section value is predicted is excluded. This leads to a lower limit on the resonance mass. It should be emphasized, however, that any mass limit is inherently model-dependent, while the upper limits on the cross section do not carry such strong dependencies on the considered model.

Section 6.3.1 summarizes the CL_s limits, which are considered as the main result. As a cross-check, limits are also set with a Bayesian method discussed in section 6.3.2, and section 6.3.3 briefly revisits the presented results.

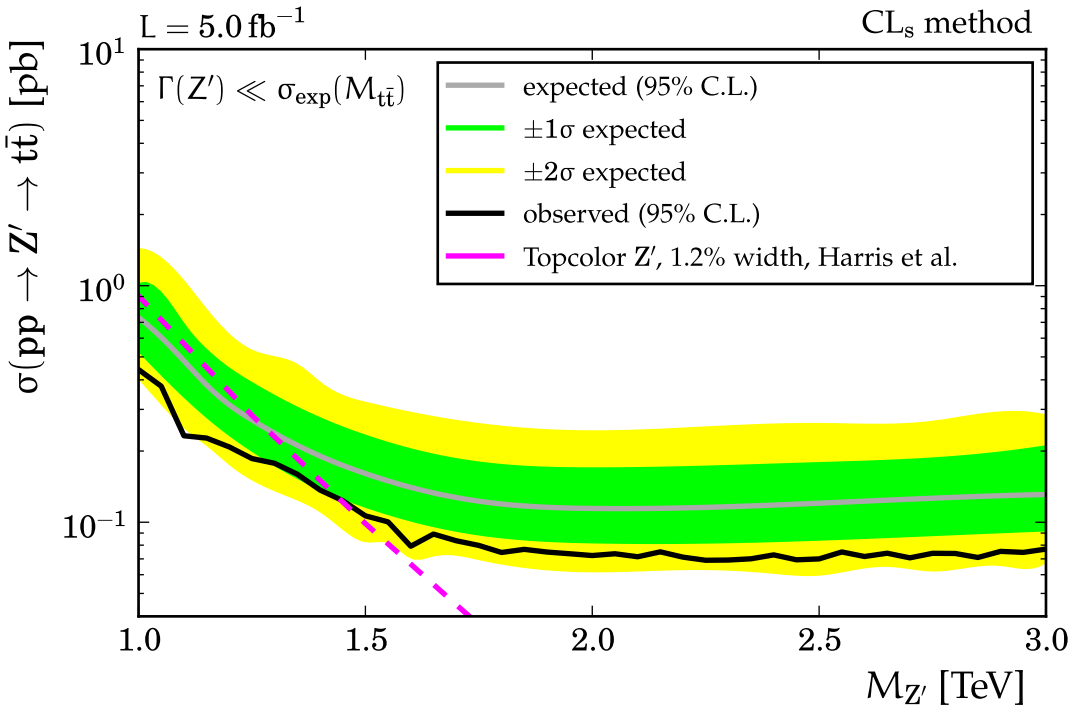

Figure 6.2: Expected and observed upper limits using the CL$_s$ method for the cross section $\sigma(pp \to Z' \to t\bar{t})$ for narrow resonances Z′ with a natural width much smaller than the experimental resolution. The excluded mass region for this topcolor Z′ model [3] is $M_{Z'} < 1.44\,\text{TeV}$.

6.3.1 CL$_s$ limits

The expected and observed limits for the CL$_s$ method for the three different types of resonances are shown in figures 6.2 to 6.4. The excluded cross sections for the different signal types at some mass points are given in table 6.2. As discussed in section 4.4, the selection efficiency for narrow Z′ become smaller in the region $M_{Z'} \geqslant 2\,\text{TeV}$, leading to a larger limit for $M_{Z'} = 3\,\text{TeV}$ than for $M_{Z'} = 2\,\text{TeV}$. The limits on the wide Z′ are higher than for the narrow Z′ as the signal shape in the $M_{t\bar{t}}$ distribution is broader.

In table 6.3, the mass limits for these models are summarized. The observed limits on the cross section are consistently lower than the expected ones, reflecting that the prediction used in the statistical model predicts more events than actually observed, as discussed in section 4.4. Overall, the data is consistent with the standard model background, and there is no hint for resonant $t\bar{t}$ production.

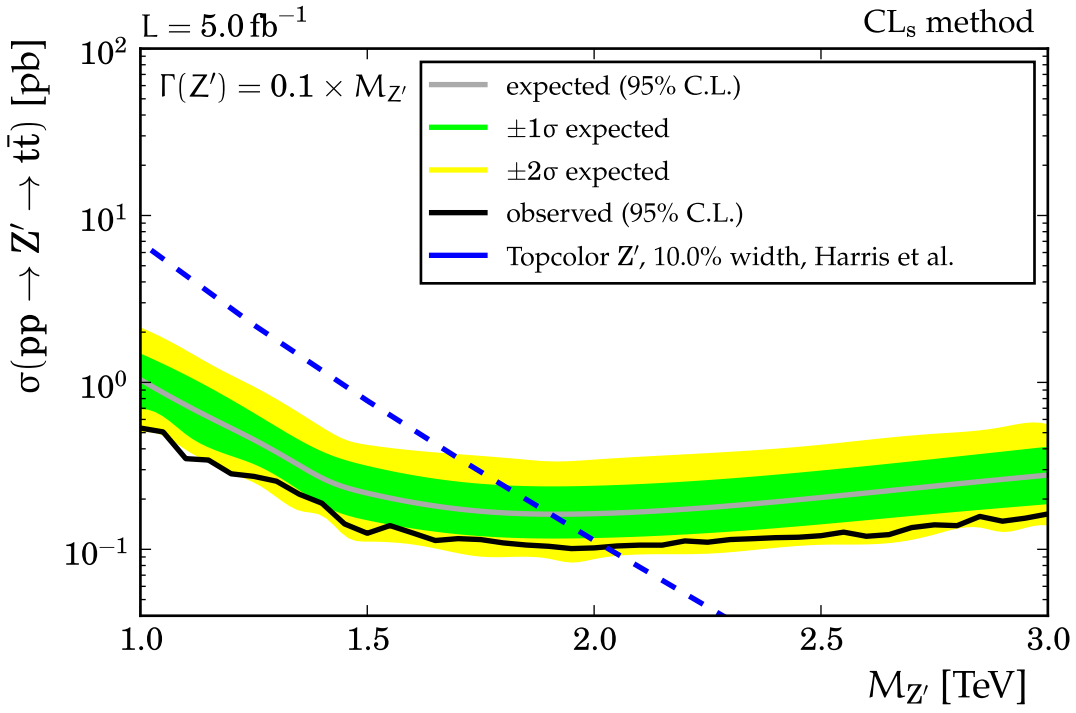

Figure 6.3: Expected and observed upper limits using the CL_s method for the cross section $\sigma(pp \to Z' \to t\bar{t})$ for resonances Z′ with a natural width of 10% of its mass. The excluded mass region for this topcolor Z′ model [3] is $M_{Z'} < 2.02\,TeV$.

	upper cross-section limit (pb)		
$M_{Z'}$ (TeV)	narrow	wide	KK gluon
1.0	0.44	0.53	0.87
1.5	0.106	0.125	0.20
2.0	0.072	0.102	0.14
3.0	0.077	0.163	0.25

Table 6.2: Upper limits for the cross section $\sigma(pp \to Z' \to t\bar{t})$ at 95% confidence level for some selected masses for the different signal types using the CL_s method.

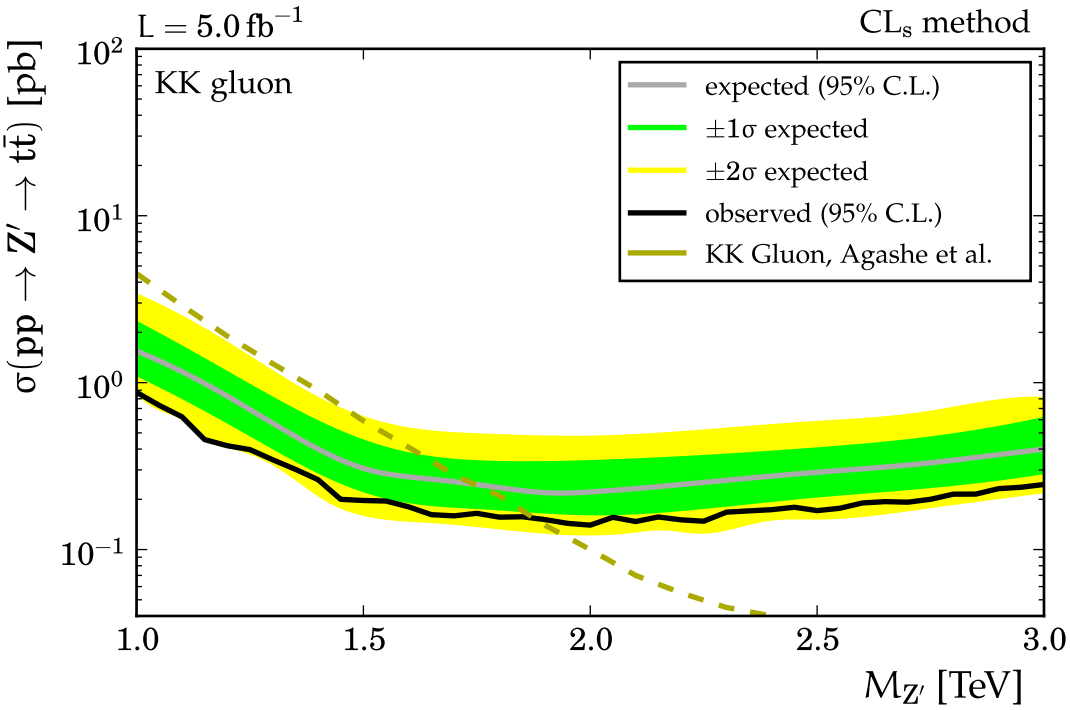

Figure 6.4: Expected and observed upper limits using the CL_s method for the cross section $\sigma(pp \to Z' \to t\bar{t})$ of Kaluza-Klein gluons [5]. The excluded mass region is $M_{Z'} < 1.88\,\text{TeV}$.

	lower $M_{Z'}$ limit (TeV)		
	Z'_t, 1.2% width	Z'_t, 10% width	KK gluon
expected	1.28	1.90	1.74
observed	1.44	2.02	1.88

Table 6.3: Expected and observed lower mass limits for the three considered signal models at 95% C.L. using the CL_s method.

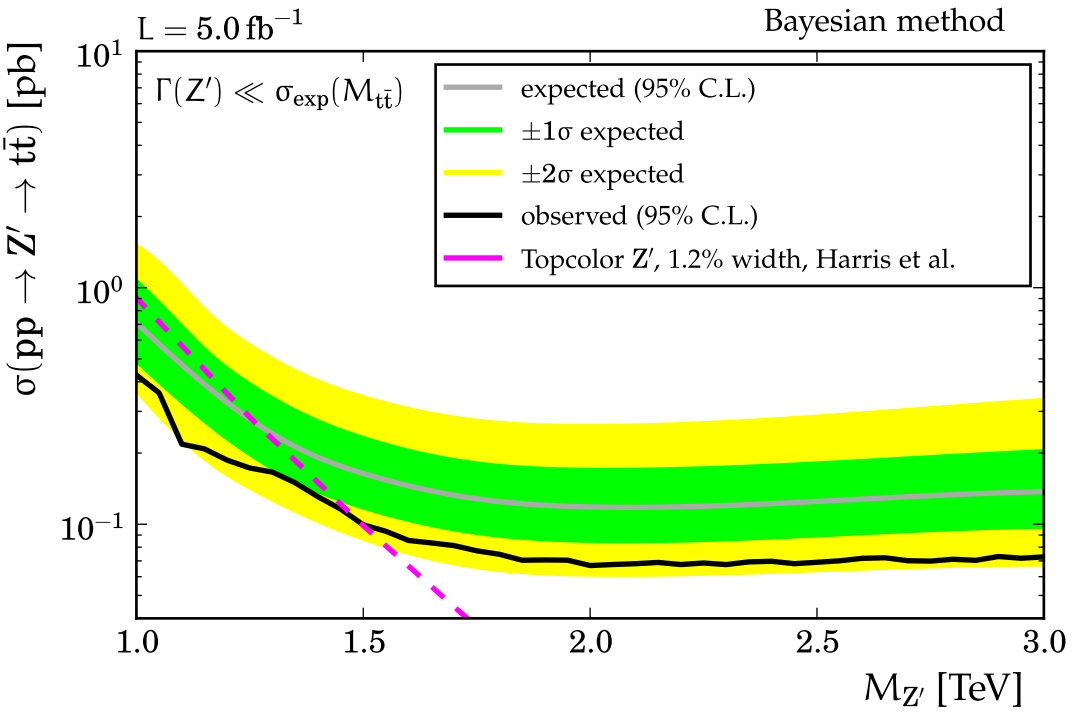

Figure 6.5: Expected and observed upper limits using the Bayesian method for the cross section $\sigma(pp \to Z' \to t\bar{t})$ for narrow resonances Z′ with a natural width much smaller than the experimental resolution. The excluded mass region for this topcolor Z′ model [3] is $M_{Z'} < 1.49\,\text{TeV}$.

6.3.2 Bayesian limits

In addition to the CL_s limits in the previous section, the Bayesian limits are given here as a cross-check. While a perfect agreement with the CL_s limits is not expected due to the different underlying concepts, a deviation of more than e.g. 20–30% in the upper limit could point to a problem in one of the implementations or it could indicate a genuine difference between the Bayesian and frequentist approach. In any case, such a deviation would suggest to conduct more studies to understand the origin of this difference.

The expected and observed limits for the different signal types are shown in Figures 6.5 to 6.7. The upper limit for some mass points are given in table 6.4. Comparing the obtained limits to the CL_s limits given in table 6.2 shows that the agreement between these methods is around 10%. The resulting mass limits are given in table 6.5.

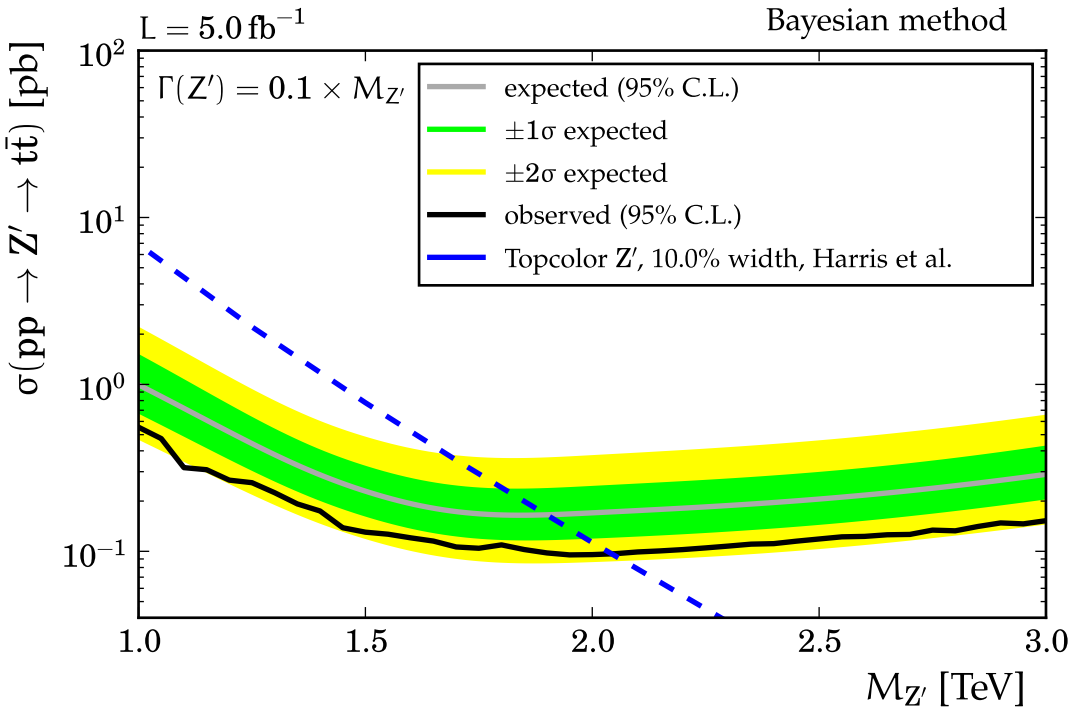

Figure 6.6: Expected and observed upper limits using the Bayesian method for the cross section $\sigma(pp \to Z' \to t\bar{t})$ for resonances Z′ with a natural width 10% of its mass. The excluded mass region for this topcolor Z′ model [3] is $M_{Z'} < 2.04\,\text{TeV}$.

	upper cross-section limit (pb)		
$M_{Z'}$ (TeV)	narrow	wide	KK gluon
1.0	0.43	0.55	0.82
1.5	0.099	0.130	0.184
2.0	0.067	0.095	0.138
3.0	0.072	0.152	0.23

Table 6.4: Upper limits for the cross section $\sigma(pp \to Z' \to t\bar{t})$ at 95% confidence level for some selected masses for the different signal types using the Bayesian method.

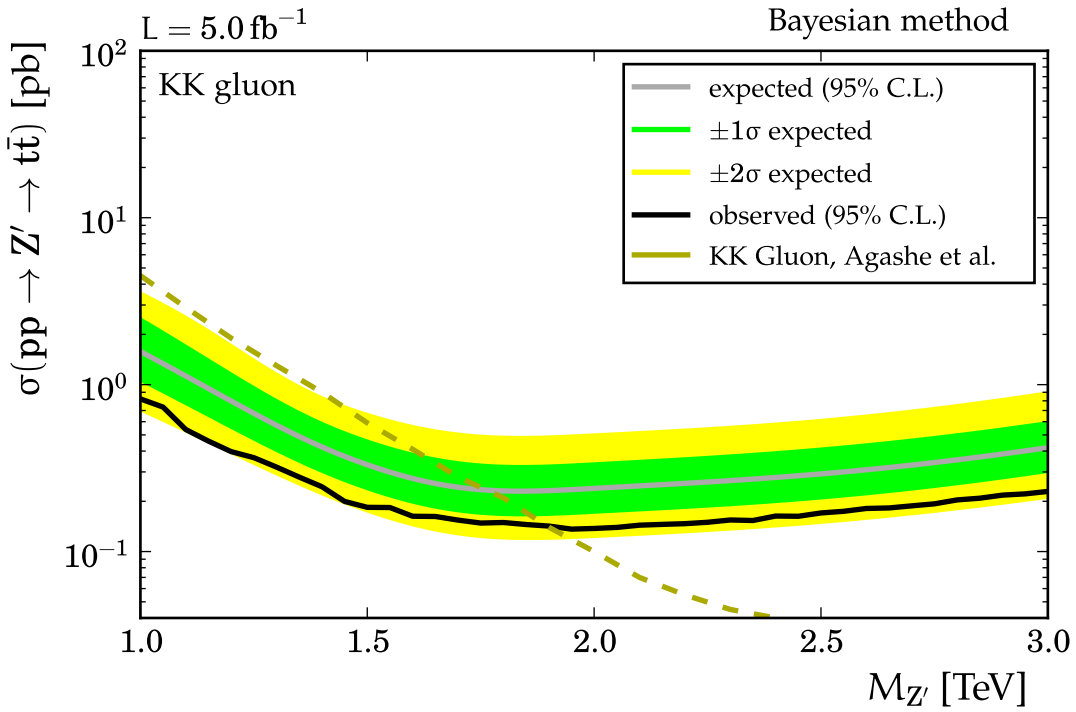

Figure 6.7: Expected and observed upper limits using the Bayesian method for the cross section $\sigma(pp \to Z' \to t\bar{t})$ of Kaluza-Klein gluons [5]. The excluded mass region is $M_{KKG} < 1.90\,\text{TeV}$.

	lower $M_{Z'}$ limit (TeV)		
	Z'_t, 1.2% width	Z'_t, 10% width	KK gluon
expected	1.26	1.90	1.76
observed	1.49	2.04	1.90

Table 6.5: Expected and observed lower mass limits for the three considered signal models at 95% C.L. using the Bayesian method.

6.3.3 Discussion

For narrow resonances Z′, the upper limits on the cross sections ranges from 0.5 pb for $M_{Z'} = 1\,\text{TeV}$ and decreases for higher Z′ masses to 0.07 pb for $M_{Z'} = 2\,\text{TeV}$. These limits apply to any resonance for which the natural width is much smaller than the experimental resolution. In particular, the leptophobic topcolor Z′ model with a width of 1.2% of $M_{Z'}$ [3] fulfills this criterion and this model is excluded for $1 < M_{Z'} < 1.44\,\text{TeV}$.

For resonances with 10% width, the $M_{t\bar{t}}$ distribution after event selection and reconstruction is broader. Therefore, the resulting limits are higher than for the narrow resonances and are in the region 0.10–0.53 pb for the whole considered mass range 1–3 TeV. Interpreting the limits on the context of a leptophobic topcolor Z′ with a width of 10%, the excluded mass range is $1 < M_{Z'} < 2.02\,\text{TeV}$.

The Kaluza-Klein excitations in the Randall-Sundrum model [5] have an even larger width of around 17% of the mass and thus results in even higher limits of about 0.14–0.9 pb in the 1–3 TeV range. This Kaluza-Klein gluon model is excluded for $M_{KKG} < 1.88\,\text{TeV}$.

7 Conclusion

In summary, this thesis presents a search for resonant $t\bar{t}$ production in the muon+jets channel, using proton–proton collisions at $\sqrt{s} = 7\,\text{TeV}$ recorded with the CMS experiment. The event signature of muon+jets $t\bar{t}$ events at high invariant $t\bar{t}$ masses includes cases in which the three quarks of the hadronic top quark decay merge to a single jet and the muon of the top quark decay is not isolated. This prohibits re-using selection and $t\bar{t}$ reconstruction techniques applied for standard model $t\bar{t}$ analyses, and a new event selection and reconstruction is applied in this analysis, which have been studied and validated on data. The most important improvements of the analysis technique over the previous version of this analysis documented in [28] are the use of b-tagging and the use of the χ^2_{min} requirement in the event selection. Both of these requirements increase the $t\bar{t}$ purity and applying both enhancements improves the expected limit by a factor 2–3, depending on the Z' mass.

The statistical analysis is performed using both a Bayesian method and the modified frequentist (CL_s) method with the theta framework. The theta framework — which I developed originally for this analysis — implements many functions for statistical modeling, e.g. template morphing and the treatment of uncertainties due to limited Monte-Carlo sample size. It also implements various statistical methods, including the CL_s method and Bayesian methods with a Markov chain Monte-Carlo algorithm. In the meantime, theta is also used in other analyses at CMS, including [25, 26, 48, 49].

Model-independent limits are set on the cross section $\sigma(pp \to Z' \to t\bar{t})$ for narrow Z' resonances and resonances with a width of 10%. In both cases, the upper limits are set as a function of the Z' mass in the mass range 1–3 TeV. The obtained limits are well below 1 pb; for $M_{Z'} > 1.5\,\text{TeV}$, the limits are in the region 0.07–0.17 pb.

Model-dependent limits are derived for a leptophobic topcolor Z' model [3] with 1.2% width, which is excluded in the region $1 < M_{Z'} < 1.44\,\text{TeV}$. Leptophobic topcolor Z' models with 10% width are excluded for $1 < M_{Z'} < 2.02\,\text{TeV}$, and Kaluza-Klein gluon excitations in the Randall-Sundrum model [5] are excluded in the region $1 < M_{KKG} < 1.88\,\text{TeV}$.

A similar analysis has been performed in the electron+jets channel at CMS, which uses similar event selection criteria and the same method for $t\bar{t}$ reconstruction [139]. The statistical combination of the muon+jets analysis discussed in this thesis and the electron+jets analysis is published in reference [30], which also includes a lepton+jets analysis focusing on lower $M_{Z'}$, mainly using a $t\bar{t}$ event topology without jet merging

and with isolated leptons. This "low-mass" analysis extends the search to the mass range $0.5 < M_{Z'} < 1\,\text{TeV}$, whereas the combination of the electron+jets and muon+jets "high-mass" analyses is more sensitive in the region $M_{Z'} > 1\,\text{TeV}$, and while the expected limits of the low-mass and high-mass analyses almost coincide for $M_{Z'} = 1\,\text{TeV}$, the high-mass analysis expected limits are lower by about a factor 2 for $M_{Z'} > 1.5\,\text{TeV}$, indicating the benefit of using analysis techniques adapted to the event topology in this mass regime. The muon+jets analysis discussed here is the single most sensitive analysis in this mass range at CMS.

The limits substantially extend previous limits for a leptophobic topcolor Z′ of, which has been excluded in the region $M_{Z'} < 0.9\,\text{TeV}$ at the Tevatron [19]. ATLAS reports comparable or slightly better results for a combined electron+jets and muon+jets analysis using substructure techniques [22].

The current analysis could be further improved by including more data taken at $\sqrt{s} = 8\,\text{TeV}$ and further optimizing the event selection, for example by replacing the currently used simple χ^2 reconstruction approach by an algorithm better adapted to the different event topologies due to the different cases of which jets merged and using more information such as b-tagging. Such an improved reconstruction could allow a better separation of the W+jets background and yield an improved mass resolution. Another possible area of improvements is the application of novel techniques for identifying high-p_T hadronically decaying top quarks by searching jet substructure. This approach has been proposed in references [158, 159]. I contributed to studies of such algorithms [27, 160–162]. Similar techniques are used in a $Z' \to t\bar{t}$ search in the $t\bar{t}$ all-hadronic channel at CMS [25]. These techniques are interesting especially for invariant $t\bar{t}$ masses even larger than the ones considered here, which will be even more important for searches performed in data taken at future runs of the LHC with higher center-of-mass energies.

Bibliography

[1] D. E. Morrissey, T. Plehn, and T. M. P. Tait. Physics searches at the LHC. *Phys. Rept.*, 515:1–113, 2012. arXiv:0912.3259 [hep-ph].

[2] R. M. Harris, C. T. Hill, and S. J. Park. Cross Section for Topcolor Z'_t decaying to $t\bar{t}$. 1999. arXiv:hep-ph/9911288.

[3] R. M. Harris and S. Jain. Cross sections for leptophobic topcolor Z′ decaying to top-antitop. *Eur. Phys. J.*, C72:2072, 2012. arXiv:1112.4928 [hep-ph].

[4] L. Randall and R. Sundrum. Large mass hierarchy from a small extra dimension. *Phys. Rev. Lett.*, 83:3370–3373, 1999. arXiv:hep-ph/9905221.

[5] K. Agashe, A. Belyaev, T. Krupovnickas, G. Perez, and J. Virzi. CERN LHC Signals from Warped Extra Dimensions. *Phys. Rev.*, D77:015003, 2008. arXiv:hep-ph/0612015.

[6] A. Leike. The phenomenology of extra neutral gauge bosons. *Phys. Rept.*, 317:143, 1999. arXiv:hep-ph/9805494.

[7] The DØ Collaboration. Measurement of the Forward-Backward Charge Asymmetry in Top-Quark Pair Production. *Phys. Rev. Lett.*, 100:142002, 2008. arXiv:0712.0851 [hep-ex].

[8] The DØ Collaboration. Forward-backward asymmetry in top quark-antiquark production. *Phys. Rev.*, D84:112005, 2011. arXiv:1107.4995 [hep-ex].

[9] The DØ Collaboration. Measurement of Leptonic Asymmetries and Top Quark Polarization in $t\bar{t}$ Production. 2012. arXiv:1207.0364 [hep-ex]. Submitted to PRL.

[10] The CDF Collaboration. Forward-Backward Asymmetry in Top Quark Production in $p\bar{p}$ Collisions at $\sqrt{s} = 1.96\,\text{TeV}$. *Phys. Rev. Lett.*, 101:202001, 2008. arXiv:0806.2472 [hep-ex].

[11] The CDF Collaboration. Evidence for a Mass Dependent Forward-Backward Asymmetry in Top Quark Pair Production. *Phys. Rev.*, D101:112003, 2011. arXiv:1101.0034 [hep-ex].

[12] The CDF Collaboration. Measurement of the top quark forward-backward production asymmetry and its dependence on event kinematic properties. 2012. arXiv:1211.1003 [hep-ex].

[13] Y. Bai, J. Hewett, J. Kaplan, and T. Rizzo. LHC predictions from a Tevatron Anomaly in the Top Quark Forward-Backward Asymmetry. *JHEP*, 2011:1–32, 2011. arXiv:1101.5203 [hep-ph].

[14] P. H. Frampton, J. Shu, and K. Wang. Axigluon as Possible Explanation for $p\bar{p} \to t\bar{t}$ Forward-Backward Asymmetry. *Phys. Lett.*, B683:294–297, 2010. arXiv:0911.2955 [hep-ph].

[15] M. I. Gresham, I. Kim, and K. M. Zurek. On Models of New Physics for the Tevatron Top A_{FB}. *Phys. Rev.*, D83:114027, 2011. arXiv:1103.3501 [hep-ph].

[16] O. Antunano, J. H. Kühn, and G. Rodrigo. Top quarks, axigluons and charge asymmetries at hadron colliders. *Phys. Rev.*, D77:014003, 2008. arXiv:0709.1652 [hep-ph].

[17] E. Alvarez, L. Da Rold, J. I. S. Vietto, and A. Szynkman. Phenomenology of a light gluon resonance in top-physics at Tevatron and LHC. *JHEP*, 1109:007, 2011. arXiv:1107.1473 [hep-ph].

[18] The CDF Collaboration. Search for resonant production of $t\bar{t}$ decaying to jets in $p\bar{p}$ collisions at $\sqrt{s} = 1.96\,\text{TeV}$. *Phys. Rev.*, D84:072003, 2011. arXiv:1108.4755 [hep-ex].

[19] The CDF Collaboration. A Search for resonant production of $t\bar{t}$ pairs in $4.8\,\text{fb}^{-1}$ of integrated luminosity of $p\bar{p}$ collisions at $\sqrt{s} = 1.96\,\text{TeV}$. *Phys. Rev.*, D84:072004, 2011. arXiv:1107.5063 [hep-ex].

[20] The DØ Collaboration. Search for a Narrow $t\bar{t}$ Resonance in $p\bar{p}$ Collisions at $\sqrt{s} = 1.96\,\text{TeV}$. *Phys. Rev.*, D85:051101, 2012. arXiv:1111.1271 [hep-ex].

[21] The ATLAS Collaboration. A search for $t\bar{t}$ resonances in lepton+jets events with highly boosted top quarks collected in pp collisions at $\sqrt{s} = 7$ TeV with the ATLAS detector. *JHEP*, 1209:041, 2012. arXiv:1207.2409 [hep-ex].

[22] The ATLAS Collaboration. A search for $t\bar{t}$ resonances in the lepton plus jets final state using $4.66\,\text{fb}^{-1}$ of pp collisions at $\sqrt{s} = 7\,\text{TeV}$. *ATLAS-CONF-2012-136*, 2012. `http://cdsweb.cern.ch/record/1478974`.

[23] The ATLAS Collaboration. A search for $t\bar{t}$ resonances with the ATLAS detector in 2.05 fb^{-1} of proton-proton collisions at $\sqrt{s} = 7$ TeV. *Eur. Phys. J.*, C72:2083, 2012. arXiv:1205.5371 [hep-ex].

[24] The ATLAS Collaboration. Search for resonances decaying into top-quark pairs using fully hadronic decays in pp collisions with ATLAS at sqrt(s) = 7 TeV. 2012. arXiv:1211.2202 [hep-ex]. Submitted to JHEP.

[25] The CMS Collaboration. Search for anomalous $t\bar{t}$ production in the highly-boosted all-hadronic final state. *JHEP*, 1209:029, 2012. arXiv:1204.2488 [hep-ex].

[26] The CMS Collaboration. Search for Z' resonances decaying to top quark-antiquark pairs in dilepton+jets final states. 2012. To be submitted to PRD.

[27] J. Ott. Studies for the Search of Heavy Particles Decaying in Top Quark Pairs with the CMS Detector. 2009. IEKP-KA/2009-20, CERN-THESIS-2009-045; `http://cdsweb.cern.ch/record/1187544`.

[28] The CMS Collaboration. Search for heavy narrow resonances decaying to $t\bar{t}$ in the muon+jets channel. *CMS PAS EXO-11-055*, 2011. `http://cdsweb.cern.ch/record/1376673`.

[29] The CMS Collaboration. Search for high-mass resonances decaying to $t\bar{t}$ in the lepton+jets channel. *CMS PAS EXO-11-093*, 2012. `http://cdsweb.cern.ch/record/1454695`.

[30] The CMS Collaboration. Search for resonant $t\bar{t}$ production in lepton+jets events in pp collisions at $\sqrt{s} = 7$ TeV. 2012. arXiv:1209.4397 [hep-ex]. Accepted for publication by JHEP.

[31] D. Griffiths. *Introduction to Elementary Particles*. Wiley-VCH, 1987.

[32] G. Moore and C. Burgess. *The Standard Model – A Primer*. Cambridge University Press, 2007.

[33] M. E. Peskin and D. V. Schroeder. *An Introduction to Quantum Field Theory*. Addison-Wesley, 1997.

[34] F. Mandl and G. Shaw. *Quantum Field Theory*. Wiley, 1984.

[35] J. Beringer et al. (Particle Data Group). The Review of Particle Physics. *Phys. Rev.*, D86:010001, 2012. `http://pdg.lbl.gov/`.

[36] G. Altarelli. The Standard model of particle physics. 2005. arXiv:hep-ph/0510281.

[37] W. Hollik. Quantum field theory and the Standard Model. 2010. arXiv:1012.3883 [hep-ph].

[38] J. L. Rosner. The Standard model in 2001. 2001. arXiv:hep-ph/0108195.

[39] P. Langacker. Introduction to the Standard Model and Electroweak Physics. 2009. arXiv:0901.0241 [hep-ph].

[40] The CMS Collaboration. Observation of a new boson at a mass of 125 GeV with the CMS experiment at the LHC. *Phys. Lett.*, B716:30–61, 2012. arXiv:1207.7235 [hep-ex].

[41] The ATLAS Collaboration. Observation of a new particle in the search for the Standard Model Higgs boson with the ATLAS detector at the LHC. *Phys. Lett.*, B716:1–29, 2012. arXiv:1207.7214 [hep-ex].

[42] The CDF Collaboration. Observation of top quark production in $\bar{\mathrm{p}}\mathrm{p}$ collisions. *Phys. Rev. Lett.*, 74:2626–2631, 1995. arXiv:hep-ex/9503002.

[43] The DØ Collaboration. Observation of the top quark. *Phys. Rev. Lett.*, 74:2632–2637, 1995. arXiv:hep-ex/9503003.

[44] The CDF and DØ Collaborations. Combination of the top-quark mass measurements from the Tevatron collider. 2012. arXiv:1207.1069 [hep-ex].

[45] The CMS Collaboration. Combination of CMS results on the mass of the top quark using up to $5.0\,\mathrm{fb}^{-1}$ of data. *CMS PAS TOP-11-018*, 2012. `http://cdsweb.cern.ch/record/1478194`.

[46] Nikolaos Kidonakis. Next-to-next-to-leading soft-gluon corrections for the top quark cross section and transverse momentum distribution. *Phys. Rev.*, D82:114030, 2010. arXiv:1009.4935 [hep-ph].

[47] The ATLAS and CMS Collaborations. Combination of ATLAS and CMS top-quark pair cross section measurements using proton-proton collisions at $\sqrt{s} = 7\,\mathrm{TeV}$. *CMS PAS TOP-12-003; ATLAS-CONF-2012-166*, 2012.

[48] The CMS Collaboration. Measurement of the single-top-quark t-channel cross section in pp collisions at $\sqrt{s} = 7\,\mathrm{TeV}$. 2012. arXiv:1209.4533 [hep-ex]. Accepcted for publication by JHEP.

[49] The CMS Collaboration. Evidence for associated production of a single top quark and W boson in pp collisions at 7 TeV. 2012. arXiv:1209.3489 [hep-ex]. Submitted to Phys. Rev. Lett.

[50] The ATLAS Collaboration. Measurement of the t-channel single top-quark production cross section in pp collisions at $\sqrt{s} = 7$ TeV with the ATLAS detector. *Phys. Lett.*, B717:330–350, 2012. arXiv:1205.3130 [hep-ex].

[51] The ATLAS Collaboration. Evidence for the associated production of a W boson and a top quark in ATLAS at $\sqrt{s} = 7$ TeV. *Phys. Lett.*, B716:142–159, 2012. arXiv:1205.5764 [hep-ex].

[52] The CMS Collaboration. Search for flavor changing neutral currents in top quark decays in pp collisions at 7 TeV. 2012. arXiv:1208.0957 [hep-ex]. Submitted to Phys. Lett. B.

[53] The ATLAS Collaboration. A search for flavour changing neutral currents in top-quark decays in pp collision data collected with the ATLAS detector at $\sqrt{s} = 7$ TeV. *JHEP*, 1209:139, 2012. arXiv:1206.0257 [hep-ex].

[54] The CMS Collaboration. Constraints on the Top-Quark Charge from Top-Pair Events. *CMS PAS TOP-11-031*, 2012. `http://cdsweb.cern.ch/record/1429970`.

[55] The ATLAS Collaboration. Measurement of the top quark charge in pp collisions at sqrts = 7 TeV in the ATLAS experiment. *ATLAS-CONF-2011-141*, 2011. `http://cdsweb.cern.ch/record/1385517`.

[56] J. H. Kühn and G. Rodrigo. Charge asymmetry of heavy quarks at hadron colliders. *Phys. Rev.*, D59:054017, 1999. arXiv:hep-ph/9807420.

[57] The CMS Collaboration. Measurement of the charge asymmetry in top-quark pair production in proton-proton collisions at $\sqrt{s} = 7$ TeV. *Phys. Lett.*, B709:28–49, 2012. arXiv:1112.5100 [hep-ex].

[58] The CMS Collaboration. Inclusive and differential measurements of the $t\bar{t}$ charge asymmetry in proton-proton collisions at 7 TeV. *Phys. Lett.*, B717:129–150, 2012. arXiv:1207.0065 [hep-ex].

[59] The ATLAS Collaboration. Measurement of the charge asymmetry in top quark pair production in pp collisions at $\sqrt{s} = 7$ TeV using the ATLAS detector. *Eur. Phys. J.*, C72:2039, 2012. arXiv:1203.4211 [hep-ex].

[60] The ATLAS Collaboration. Measurement of the charge asymmetry in dileptonic decay of top quark pairs in pp collisions at $\sqrt{s} = 7\,\text{TeV}$ using the ATLAS detector. *ATLAS-CONF-2012-057*, 2012. `http://cdsweb.cern.ch/record/1453785`.

[61] B. Lillie, L. Randall, and L. Wang. The Bulk RS KK-gluon at the LHC. *JHEP*, 0709:074, 2007. arXiv:hep-ph/0701166.

[62] J. M. Campbell, J. W. Huston, and W. J. Stirling. Hard Interactions of Quarks and Gluons: a Primer for LHC Physics. *Rep. Prog. Phys.*, 70:89, 2007. arXiv:hep-ph/0611148.

[63] M. A. Dobbs et al. Les Houches guidebook to Monte Carlo generators for hadron collider physics. 2004. arXiv:hep-ph/0403045.

[64] J. Alwall, M. Herquet, F. Maltoni, O. Mattelaer, and T. Stelzer. MadGraph 5: Going Beyond. *JHEP*, 1106:128, 2011. arXiv:1106.0522 [hep-ph].

[65] T. Sjöstrand, S. Mrenna, and P. Z. Skands. PYTHIA 6.4 Physics and Manual. *JHEP*, 0605:026, 2006. arXiv:hep-ph/0603175.

[66] The CMS Collaboration. Measurement of the underlying event activity in pp collisions at $\sqrt{s} = 0.9$ and 7 TeV with the novel jet-area/median approach. *JHEP*, 1208:130, 2012. arXiv:1207.2392 [hep-ex].

[67] J. Alwall, S. Hoche, F. Krauss, N. Lavesson, L. Lonnblad, et al. Comparative study of various algorithms for the merging of parton showers and matrix elements in hadronic collisions. *Eur. Phys. J.*, C53:473–500, 2008. arXiv:0706.2569 [hep-ph].

[68] CERN AC Team. The four main LHC experiments. `http://cdsweb.cern.ch/record/40525`, 1999. CERN-AC-9906026.

[69] E. Lyndon et al. LHC Machine. *JINST*, 3:S08001, 2008. `http://cdsweb.cern.ch/record/1129806`.

[70] The ALICE Collaboration. The ALICE experiment at the CERN LHC. A Large Ion Collider Experiment. *JINST*, 3:S08002, 2008. `http://cdsweb.cern.ch/record/1129812`.

[71] The LHCb Collaboration. The LHCb Detector at the LHC. *JINST*, 3:S08005, 2008. `http://cdsweb.cern.ch/record/1129809`.

[72] CERN Web Communications. CERN LHC: the guide – faq. http://cdsweb.cern.ch/record/999421, 2006. CERN-BROCHURE-2006-003-ENG.

[73] CERN. Summary of the analysis of the 19 September 2008 incident at the LHC. http://cdsweb.cern.ch/record/1135729, 2008.

[74] CERN. Final LHC magnet goes underground. http://press.web.cern.ch/press-releases/2009/04/final-lhc-magnet-goes-underground, 2009.

[75] CERN. LHC to run at 3.5 TeV for early part of 2009–2010 run rising later. http://press.web.cern.ch/press-releases/2009/08/lhc-run-35-tev-early-part-2009-2010-run-rising-later, 2009.

[76] CERN. LHC Performance and Statistics. http://lhc-statistics.web.cern.ch/LHC-Statistics/.

[77] The CMS Collaboration. The CMS experiment at the CERN LHC. *JINST*, 3:S08004, 2008. http://cdsweb.cern.ch/record/1129810.

[78] The CMS Collaboration. CMS physics: Technical design report. *CERN-LHCC-2006-001*, 2006. http://cdsweb.cern.ch/record/922757.

[79] The CMS Collaboration. Detector Drawings. *CMS-PHO-GEN-2012-002*. http://cdsweb.cern.ch/record/1433717.

[80] The CMS Collaboration. CMS: Tracker Technical Design Report. *CERN-LHCC-98-006*, 1998. http://cdsweb.cern.ch/record/368412.

[81] The CMS Collaboration. CMS: The electromagnetic calorimeter. Technical design report. *CERN-LHCC-97-033*, 1997. http://cdsweb.cern.ch/record/349375.

[82] G. Della Ricca for the CMS Collaboration. Performance of the CMS Electromagnetic Calorimeter at the LHC. *CMS-CR-2011-297*, 2011. http://cdsweb.cern.ch/record/1455282.

[83] The CMS Collaboration. CMS: The hadron calorimeter technical design report. *CERN-LHCC-97-31*, 1997. http://cdsweb.cern.ch/record/357153.

[84] P. Gras for the CMS Collaboration. Commissioning and performance of the CMS calorimeter system with proton-proton collisions at the LHC. *CMS-CR-2010-272*, 2010.

[85] The CMS Collaboration. The CMS muon project: Technical Design Report. *CERN-LHCC-97-032*, 1997. http://cdsweb.cern.ch/record/343814.

[86] The CMS Collaboration. CMS TriDAS project. Volume 1: The Trigger Systems. *CERN-LHCC-2000-038*, 2000. http://cdsweb.cern.ch/record/706847.

[87] The CMS Collaboration. CMS TriDAS project. Volume 2: Data Acquisition and High-Level Trigger. *CERN-LHCC-2002-026*, 2002. http://cdsweb.cern.ch/record/578006.

[88] The CMS Collaboration. CMS: The computing project. Technical design report. *CERN-LHCC-2005-023*, 2005. http://cdsweb.cern.ch/record/838359.

[89] HEPiX CPU Benchmark Working Group. HEP-SPEC06 Benchmark. https://hepix.caspur.it/afs/hepix.org/project/benchmarks/doku.php.

[90] K. Bloom for the CMS Collaboration. CMS resource utilization and limitations on the grid after the first two years of LHC collisions. *CMS-CR-2012-078*, 2012. http://cdsweb.cern.ch/record/1457420.

[91] The CMS Collaboration. Absolute Calibration of the CMS Luminosity Measurement: Summer 2011 Update. *CMS PAS EWK-11-001*, 2011.

[92] S. van der Meer. Calibration of the effective beam height in the ISR. *CERN-ISR-PO-68-31*, 1968. http://cdsweb.cern.ch/record/296752.

[93] The CMS Collaboration. Absolute Calibration of the Luminosity Measurement at CMS: Winter 2012 Update. *CMS PAS SMP-12-008*, 2012. http://cdsweb.cern.ch/record/1434360.

[94] The CMS Collaboration. CMS Luminosity - Public Results. 2012. http://twiki.cern.ch/twiki/bin/view/CMSPublic/LumiPublicResults2011.

[95] S. Agostinelli et al. (GEANT4 Collaboration). GEANT4—a simulation toolkit. *Nucl. Instrum. and Methods*, A506:250–303, 2003.

[96] P. Nason. A New method for combining NLO QCD with shower Monte Carlo algorithms. *JHEP*, 0411:040, 2004. arXiv:hep-ph/0409146.

[97] S. Frixione, P. Nason, and C. Oleari. Matching NLO QCD computations with Parton Shower simulations: the POWHEG method. *JHEP*, 0711:070, 2007. arXiv:0709.2092 [hep-ph].

[98] S. Alioli, P. Nason, C. Oleari, and E. Re. A general framework for implementing NLO calculations in shower Monte Carlo programs: the POWHEG BOX. *JHEP*, 1006:043, 2010. arXiv:1002.2581 [hep-ph].

[99] S. Alioli, P. Nason, C. Oleari, and E. Re. NLO single-top production matched with shower in POWHEG: s- and t-channel contributions. *JHEP*, 0909:111, 2009. arXiv:0907.4076 [hep-ph].

[100] E. Re. Single-top Wt-channel production matched with parton showers using the POWHEG method. *Eur. Phys. J.*, C71:1547, 2011. arXiv:1009.2450 [hep-ph].

[101] J. Pumplin, D.R. Stump, J. Huston, H.L. Lai, P. M. Nadolsky, et al. New generation of parton distributions with uncertainties from global QCD analysis. *JHEP*, 0207:012, 2002. arXiv:hep-ph/0201195.

[102] P. Bartalini and L. Fanò for the CMS Collaboration. Multiple Parton Interactions Studies at CMS. *CMS-CR-2011-048*, 2011. arXiv:1103.6201 [hep-ex].

[103] J. M. Campbell, R. K. Ellis, and C. Williams. MCFM web page. `http://mcfm.fnal.gov/`.

[104] N. Kidonakis. Next-to-next-to-leading-order collinear and soft gluon corrections for t-channel single top quark production. *Phys. Rev.*, D83:091503, 2011. arXiv:1103.2792 [hep-ph].

[105] N. Kidonakis. Two-loop soft anomalous dimensions for single top quark associated production with a W^- or H^-. *Phys. Rev.*, D82:054018, 2010. arXiv:1005.4451 [hep-ph].

[106] T. Sjöstrand, S. Mrenna, and P. Z. Skands. A Brief Introduction to PYTHIA 8.1. *Comput. Phys. Commun.*, 178:852–867, 2008. arXiv:0710.3820 [hep-ph].

[107] W. Adam, B. Mangano, Th. Speer, and T. Todorov. Track Reconstruction in the CMS Tracker. *CMS-NOTE-2006-041*, 2006. `http://cdsweb.cern.ch/record/934067`.

[108] S. Cucciarelli, M. Konecki, D. Kotlinski, and T. Todorov. Track reconstruction, primary vertex finding and seed generation with the Pixel Detector. *CMS-NOTE-2006-026*, 2006. `http://cdsweb.cern.ch/record/927384`.

[109] R. E. Kalman. A New Approach to Linear Filtering and Prediction Problems. *Trans. ASME*, D82:35–45, 1960.

[110] G. Sguazzoni for the CMS Collaboration. CMS reconstruction improvements for the tracking in large pile-up events. *CMS-CR-2012-085*, 2012. http://cdsweb.cern.ch/record/1457651.

[111] W. Erdmann. Offline Primary Vertex Reconstruction with Deterministic Annealing Clustering. *CMS IN-2011-014*, 2011. http://cdsweb.cern.ch/record/1365063.

[112] K. Rose. Deterministic annealing for clustering, compression, classification, regression, and related optimization problems. *Proceedings of the IEEE*, 86(11):2210–2239, 1998.

[113] The CMS Collaboration. Performance of muon reconstruction in pp collision events at $\sqrt{s} = 7$ TeV. *JINST*, 7:10002, 2012. arXiv:1206.4071.

[114] CMS Muon POG. Reference muon id and isolation efficiencies. http://twiki.cern.ch/twiki/bin/viewauth/CMS/MuonReferenceEffs.

[115] S. Baffioni et al. Electron reconstruction in CMS. *Eur. Phys. J.*, C49:1099–1116, 2007. http://cdsweb.cern.ch/record/934070.

[116] The CMS Collaboration. Electron reconstruction and identification at $\sqrt{s} =$ 7 TeV. *CMS PAS EGM-10-004*, 2010. http://cdsweb.cern.ch/record/1299116.

[117] R. Frühwirth. Track fitting with non-Gaussian noise. *Comp. Phys. Commun.*, 100(1–2):1–16, 1997. http://dx.doi.org/10.1016/S0010-4655(96)00155-5.

[118] W. Adam, R. Frühwirth, A. Strandlie, and T. Todor. Reconstruction of Electrons with the Gaussian-Sum Filter in the CMS Tracker at the LHC. *CMS-NOTE-2005-001*, 2005. http://cdsweb.cern.ch/record/815410.

[119] CMS EGamma POG. Cut Based Electron ID , 2012. http://twiki.cern.ch/twiki/bin/viewauth/CMS/EgammaCutBasedIdentification.

[120] The CMS Collaboration. Particle–Flow Event Reconstruction in CMS and Performance for Jets, Taus, and $\mathrm{E}_{\mathrm{T}}^{\mathrm{miss}}$. *CMS PAS PFT-09-001*, 2009. http://cdsweb.cern.ch/record/1194487.

[121] A. Bhatti et al. Performance of the SISCone Jet Clustering Algorithm. *CMS AN-2008/002*, 2008.

[122] S. D. Ellis and D. E. Soper. Successive Combination Jet Algorithm For Hadron Collisions. *Phys. Rev.*, D48:3160–3166, 1993. arXiv:hep-ph/9305266.

[123] Yu. L. Dokshitzer, G. D. Leder, S. Moretti, and B. R. Webber. Better jet clustering algorithms. *JHEP*, 9708:001, 1997. arXiv:hep-ph/9707323.

[124] M. Cacciari, G. P. Salam, and G. Soyez. The anti-k_t jet clustering algorithm. *JHEP*, 04:63, 2008. arXiv:0802.1189 [hep-ex].

[125] M. Cacciari and G. P. Salam. Dispelling the N^3 myth for the k_t jet-finder. *Phys. Lett.*, B641(1):57–61, 2006. arXiv:hep-ph/0512210.

[126] M. Cacciari, G. P. Salam, and G. Soyez. FastJet User Manual. *Eur. Phys. J.*, C72:1896, 2012. arXiv:1111.6097 [hep-ph].

[127] M. Cacciari, G. P. Salam, and G. Soyez. The Catchment Area of Jets. *JHEP*, 0804:005, 2008. arXiv:0802.1188 [hep-ph].

[128] The CMS Collaboration. Determination of Jet Energy Calibration and Transverse Momentum Resolution in CMS. *JINST*, 6:11002, 2011. arXiv:1107.4277.

[129] M. Cacciari and G. P. Salam. Pileup subtraction using jet areas. *Phys. Lett.*, B659:119–126, 2008. arXiv:0707.1378 [hep-ph].

[130] The CMS Collaboration. b-Jet Identification in the CMS Experiment. *CMS PAS BTV-11-004*, 2012. `http://cdsweb.cern.ch/record/1427247`.

[131] The CMS Collaboration. Measurement of the b-tagging efficiency using $t\bar{t}$ events. *CMS PAS BTV-11-003*, 2012. `http://cdsweb.cern.ch/record/1421611`.

[132] The CMS Collaboration. Missing transverse energy performance of the CMS detector. *JINST*, 6:09001, 2011. arXiv:1106.5048 [physics.ins-det].

[133] The CMS Collaboration. Jet Energy Resolution Measurement. 2012. `http://twiki.cern.ch/twiki/bin/viewauth/CMS/JetResolution`.

[134] The CMS Collaboration. Recommendation for b/c-tagging and mistagging Data/MC Scale Factors. 2012. `http://twiki.cern.ch/twiki/bin/viewauth/CMS/BtagPOG`.

[135] The CMS Collaboration. Measurement of the inelastic pp cross section at $\sqrt{s} = 7\,\text{TeV}$. *CMS PAS QCD-11-002*, 2012. `http://cdsweb.cern.ch/record/1433413`.

[136] The CMS Collaboration. Measurement of the inelastic pp cross section at $\sqrt{s} = 7\,\text{TeV}$ with the CMS detector. *CMS PAS FWD-11-001*, 2011. `http://cdsweb.cern.ch/record/1373466`.

[137] The CMS Collaboration. Estimating Systematic Errors Due to Pileup Modeling. 2012. http://twiki.cern.ch/twiki/bin/view/CMS/PileupSystematicErrors.

[138] The CMS Collaboration. Measurement of associated charm production in W final states at $\sqrt{s} = 7\,\text{TeV}$. *CMS PAS EWK-11-013*, 2011. http://cdsweb.cern.ch/record/1369558.

[139] The CMS Collaboration. Search for high-mass resonances decaying to $t\bar{t}$ in the electron+jets channel. *CMS PAS EXO-11-092*, 2012. http://cdsweb.cern.ch/record/1423037.

[140] T. Chwalek. Measurement of W-Boson Helicity-Fractions in Top-Quark Decays with the CDF II Experiment and Prospects for an Early $t\bar{t}$ Cross-Section Measurement with the CMS Experiment. 2010. IEKP-KA/2010-5, CERN-THESIS-2010-255; http://cdsweb.cern.ch/record/1416031.

[141] S. Gadatsch. Template morphing in many dimensions, with several fit parameters, 2009. Presentation in the ATLAS Statistics Forum; http://indico.cern.ch/getFile.py/access?contribId=5&resId=0&materialId=slides&confId=74940.

[142] J. S. Conway. Nuisance Parameters in Likelihoods for Multisource Spectra. 2011. arXiv:1103.0354 [physics.data-an]. In: Proceedings of PHYSTAT 2011 Workshop on Statistical Issues Related to Discovery Claims in Search Experiments and Unfolding, CERN-2011-006, H.B. Prosper and L. Lyons eds.

[143] R. J. Barlow and C. Beeston. Fitting using finite Monte Carlo samples. *Comput. Phys. Commun.*, 77:219–228, 1993.

[144] J. Neyman. Outline of a Theory of Statistical Estimation Based on the Classical Theory of Probability. *Philosophical Transactions of the Royal Society of London. Series A, Mathematical and Physical Sciences*, 236(767):333–380, 1937.

[145] J. Neyman and E. S. Pearson. On the Problem of the Most Efficient Tests of Statistical Hypotheses. *Philosophical Transactions of the Royal Society of London. Series A, Containing Papers of a Mathematical or Physical Character*, 231:289–337, 1933.

[146] The ATLAS Collaboration, the CMS Collaboration, and the LHC Higgs Combination Group. Procedure for the LHC Higgs boson search combination in Summer 2011. (CMS-NOTE-2011-005), 2011.

[147] Yu. V. Linnik. On the elimination of nuisance parameters in statistical problems. *Proc. 5th Berkeley Sympos. math. Statist. Probab., Univ. Calif. 1965/1966*, pages 267–280, 1967.

[148] E. C. Fieller. Some Problems in Interval Estimation. *Journal of the Royal Statistical Society. Series B (Methodological)*, 16(2):175–185, 1954.

[149] A. L. Read. Presentation of search results: the CL_s technique. *Journal of Physics G: Nuclear and Particle Physics*, 28(10):2693, 2002.

[150] T. Junk. Confidence level computation for combining searches with small statistics. *Nucl. Instrum. Methods Phys. Res.*, A434(2-3):435–443, 1999. arXiv:hep-ex/9902006.

[151] R. E. Kass and L. Wasserman. The Selection of Prior Distributions by Formal Rules. *J. Amer. Statist. Assoc.*, 91, 1996.

[152] R. Brun and F. Rademakers. ROOT – An Object Oriented Data Analysis Framework. *Nucl. Instrum. Methods Phys. Res.*, A389:81–86, 1996. `http://root.cern.ch/`.

[153] F. James and M. Roos. Minuit: A System for Function Minimization and Analysis of the Parameter Errors and Correlations. *Comput. Phys. Commun.*, 10:343–367, 1975. `http://dx.doi.org/10.1016/0010-4655(75)90039-9`.

[154] L. Moneta, K. Cranmer, G. Schott, and W. Verkerke. The RooStats Project. 2010. arXiv:1009.1003 [physics.data-an]. ACAT2010 Conference Proceedings.

[155] N. Metropolis, A. W. Rosenbluth, M. N. Rosenbluth, A. H. Teller, and E. Teller. Equation of State Calculations by Fast Computing Machines. *Journal of Chemical Physics*, 21(6):1087–1092, 1953. `http://dx.doi.org/10.1063/1.1699114`.

[156] W. K. Hastings. Monte Carlo sampling methods using Markov chains and their applications. *Biometrika*, 57(1):97–109, 1970. `http://dx.doi.org/10.1093/biomet/57.1.97`.

[157] A. Gelman, G. O. Roberts, and W. R. Gilks. Efficient Metropolis Jumping Rules. *Bayesian Statistics*, 5:599–607, 1996.

[158] J. M. Butterworth et al. Jet substructure as a new Higgs search channel at the LHC. *Phys. Rev. Lett.*, 100:242001, 2008. arXiv:0802.2470 [hep-ph].

[159] D. E. Kaplan et al. Top Tagging: A Method for Identifying Boosted Hadronically Decaying Top Quarks. *Phys. Rev. Lett.*, 101:142001, 2008. arXiv:0806.0848 [hep-ph].

[160] J. Babb, D. Boumediene, et al. Studies of Top Tagging Algorithms. *CMS AN-2010/080*, 2010.

[161] J. Babb, D. Boumediene, et al. Optimization and Commissioning of Jet Substructure Algorithms. *CMS AN-2010/330*, 2010.

[162] A. Abdesselam, E. Bergeaas Kuutmann, U. Bitenc, G. Brooijmans, J. Butterworth, et al. Boosted objects: A Probe of beyond the Standard Model physics. *Eur. Phys. J.*, C71:1661, 2011. arXiv:1012.5412 [hep-ph].

List of Figures

List of Tables

Acknowledgements

I want to thank my supervisor Prof. Müller for the opportunity of working in his group and the possibility to spend one year at CERN. I would also like to show my gratitude to Jeannine Wagner-Kuhr for her guidance and support. I am thankful Prof. Quast for his insights and for his role as co-supervisor for this thesis. I also want to thank my colleagues in the IEKP, who have been pleasant and helpful, especially Thorsten Chwalek and Frank Roscher, who provided many valuable comments on the thesis drafts.